北京大学

博士研究生学位论文

题目：日本 J-PARC 缪子反常磁矩与电二极矩测量实验中热缪子源的开发

姓　　名：张策

学　　号：1701110101

院　　系：物理学院

专　　业：粒子物理与原子核物理

研究方向：高能物理实验

导　　师：冒亚军 教授

二〇二二 年 六 月

版权声明

摘要

2012 年，希格斯玻色子（Higgs boson）在大型强子对撞机中被确认后，粒子物理标准模型所预测的所有基本粒子均已被发现。在此之后，寻找超出标准模型的新物理已经成为高能实验物理的研究重点。在高亮度前沿，针对缪子（muon，又称 μ 子）反常磁矩的测量（也称 muon $g-2$）是当下探索的焦点方向之一。

缪子反常磁矩的理论计算和实验测量贯穿了标准模型的发展史。它一直是能对标准模型进行最精确检验的“探针”之一。自二十世纪六十年代起，缪子反常磁矩的测量实验横跨欧美、历经数代。2021 年 4 月，美国费米加速器实验室公布了其首批缪子反常磁矩的实验测量值。经其更新后，缪子反常磁矩的综合实验测量值与标准模型的理论预言值之间存在 4.2 σ 的标准偏差。为了确认新物理的存在与否，实验测量精度亟待进一步提高。

在此背景下，日本高强度质子加速器研究所（Japan Proton Accelerator Research Complex, J-PARC）提出了全新的缪子反常磁矩与电二极矩（EDM）测量实验（Muon $g-2$/EDM 实验，也称 E34 实验）。与以往的实验相比，本实验将采用完全不同的方法和技术。实验预计在 2027 年开始取数，其最终的缪子反常磁矩测量目标精度和正在进行的费米实验的精度相同（0.1 ppm）。这一全新、独立的实验能够进一步提升缪子反常磁矩测量结果的精度和可信度，与费米实验室的结果相互检验，为寻找标准模型之外的新物理提供结论。

本论文的工作聚焦于日本实验中最具创新性与挑战性的步骤：热缪子源（thermal muon source）的开发。作为缪子冷却（muon cooling）技术的一种，本实验将源于质子加速打靶产生的表面 μ^+ 束流（surface muon beam）首先导入硅凝胶材料（silica aerogel）中冷却，μ^+ 和材料中的电子（e^-）结合，形成束缚态的热缪子素（muonium）。随后该原子将在真空中被激光电离，生成热缪子（thermal muon，也称 ultra-cold muon）。最后，热缪子束流将被重新加速、注入加有弱磁场的储存环中并测量其衰变的正电子数目随时间的演化，最终可由数据分析得到缪子的反常磁矩和电二极矩。

这一套热缪子源的制备方法为全世界首次提出，所产生的热缪子的平均动能仅为 0.02 eV 左右，比目前其他缪子测量实验中所用的低能缪子的平均动能还要低 1-2 个数量级。经过重新加速后，缪子束流的发散度是传统表面缪子束流的约千分之一。这一高品质的热缪子源不仅仅可用于本实验，更可能在今后广泛应用于其他的缪子物理实验，如缪子素能级结构的精细测量、缪子显微镜技术和未来的缪子对撞机设计等。

① 本研究得到中国国家留学基金资助。

目前，在热缪子源的开发中，存在两个关键问题：第一，世界范围内，整套方案尚未得到实验原型机层面上的完整实现；第二，根据目前的模拟预计，本实验的缪子反常磁矩的测量精度（统计误差）约为 0.45 ppm 左右。为了更进一步提高精度，达到最终目标（0.1 ppm），需要在现有实验方案基础上进一步提升热缪子的产生效率。

针对第一个问题，为了验证整套热缪子源制备方法的可行性，并对热缪子的产生效率、运动学性质等有更好的了解，我们提出了缪子素激光电离实验（muonium laser-ionization experiment）。我们的实验采用和 E34 实验相同的热缪子生成方法，也即通过硅凝胶产生缪子素，并由激光电离缪子素产生热缪子。与 E34 实验不同的是，本实验中，我们在下游设计了一套慢化缪子束线（slow muon beam-line），结合微通道板探测器（micro channel plate, MCP），对激光电离生成的热缪子进行初级加速和快速测量。利用本实验中 244 纳米波长的紫外激光，更能进一步测量缪子素从基态（1S 态）到激发态（2S 态）的跃迁能量，进而精确测量缪子质量。

本工作首先从模拟出发，利用 Geant4、Opera 等模拟软件估计了实验各个阶段的效率（包括表面缪子的传输、硅凝胶中缪子素的生成、激光电离和热缪子的传输等阶段），进而估计了热缪子在探测器上的强度。接着，我们开展了一系列的硬件准备工作：包括慢化缪子加速束线各部件的组装和校准、真空测试、高压测试、远程控制系统的开发、探测器的组装和测试等关键工作，确认了整套装置能够完整运行。最终我们将激光和束线结合，开展实验、获取数据。

我们的实验成功探测到了热缪子信号，确认了热缪子的生成。实验测得的信号特征和模拟结果符合。由此结果，我们确认了整套热缪子生成方法的可行性，估计了热缪子的生成效率，测量了热缪子的束斑性质，获得了最佳束流参数，并讨论了模拟预测和实验计数结果之间差异的原因。本实验初步测得的激光共振频率及其宽度与过去的实验结果一致，信号的平均计数率比以往的最佳结果高出 43 倍左右。

针对第二个问题，本论文在现有设计的基础上，创新性地提出了多层硅凝胶靶的设计。在此方案中，表面缪子束流打入多层靶中，进而提高缪子素的产率。同时，缪子素将被束缚在多层靶之间的真空中，进而提升激光电离产生热缪子的效率。本研究首先从概念设计出发，在单层靶模拟工作的基础上拓展了缪子素在硅凝胶材料中的扩散模型，并将激光电离的模拟与模型相结合，完整描述了热缪子的产生过程。利用蒙特卡洛模拟，我们优化了多层靶的几何参数，估计了热缪子的产生效率。在不同的激光能量下，相比于单层靶方案，热缪子产生效率可以提升 3 至 4 倍。

以上各项工作充分研究了热缪子源的生成及其各种重要性质。利用单层靶的基础方案，在即将开始建设的 E34 实验中，储存环中的 μ^+ 束流强度可以估计为 2×10^5 Hz 左右，符合 E34 实验第一阶段的统计量要求，确认了缪子反常磁矩的统计误差可以达

到 0.45 ppm，这将是 E34 实验的一个里程碑。再结合多层靶设计方案，E34 实验的缪子束流强度可以提升 3 至 4 倍左右，进一步使实验的统计误差降低一半左右，为达到缪子反常磁矩测量的最终精度目标 0.1 ppm 提供了希望。

关键词：缪子反常磁矩，热缪子源，缪子冷却，缪子素，激光电离

Development of thermal muon source for muon $g-2$/EDM experiment at J-PARC

Ce ZHANG (Particle Physics and Nuclear Physics)
Directed by Prof. Yajun Mao

ABSTRACT

The Higgs boson discovery at the Large Hadron Collider (LHC) in 2012 was an essential milestone in Standard Model (SM). In the post-Higgs era, high-energy physicists have focused on searching for new physics beyond SM. In the high-intensity frontier, the anomalous magnetic moment of muon (also known as muon $g-2$) has attracted great interest.

For decades, muon $g-2$ has been one of the most precisely measured quantities and the best probe to the new physics beyond SM. Since the 1960s, a series of experiments on storage-ring muon $g-2$ have been performed from CERN to the US. In April 2021, Fermi National Accelerator Laboratory (FNAL) published their analysis result of Run-1 data on the muon $g-2$. The statistically combined result with the previous one at Brookhaven National Laboratory (BNL) gives a 4.2 σ tension between experimental results and theoretical predictions. More precise measurements are necessary to study further such discrepancy and the possibility of the new physics behind it.

Meanwhile, an independent experiment was proposed aiming for muon $g-2$ and electric dipole moment (EDM) at Japan Proton Accelerator Research Complex (J-PARC), known as Muon $g-2$/EDM experiment (E34). The E34 experiment takes a different approach from its FNAL and BNL counterparts. The experiment is expected to finish the installation and start the first data from 2027, with a target precision of 0.1 ppm (parts per million), similar to the FNAL experiment. This new experiment will improve the experimental accuracy and provide independent cross-checks toward the conclusion of the muon anomaly.

This thesis focuses on the most innovative and challenging stage in the E34 experiment: the development of the thermal muon source. As one of the muon cooling technologies, the surface muons are firstly transported and stopped in the silica aerogel target. Muons are cooled down inside the target and form the thermal muonium atoms (the bound state of μ^+ and e^-). Thermal muonium diffuses into the vacuum and is ionized by a laser, creating the thermal

muon. After re-acceleration, muons are injected into the storage ring with a magnetic field, where decay positrons will be detected. The muon's anomalous magnetic moment is extracted by analyzing the evolution of the number of detected positrons above an energy threshold.

Such a thermal muon production method is the first of its kind globally. After cooling, the average kinetic energy of the thermal muon source is only 0.02 eV, typically one order smaller than that of the low energy muon source currently being used in other experiments. Moreover, the source has an extensive range of applications, not only in the Muon $g-2$/EDM experiment but also in other muon-related precision experiments, such as muonium hyperfine splitting and muonium 1S-2S spectroscopy, muon microscopy, and the muon collider projects in the future.

Currently, there are two main issues in the development of thermal muon source: (1) the entire scheme has not yet been validated through a prototype setup, confirming the efficiency and intensity of thermal muon predicted by simulation, which is a crucial step before constructing the E34 experiment; (2) To exceed the current statistic limit, novel ideas are necessary towards the final statistical goal of 0.1 ppm on a_μ measurement.

In light of the first issue, the muonium (Mu) ionization experiment was proposed to study the thermal muon generation and the dynamics of the thermal muon beam. The experiment utilized the same scheme as the E34 experiment on Mu generation and laser ionization. A slow muon beam-line (SMBL) was prepared after the thermal muon generation, which accelerated and transported the thermal muon to the multi-channel plate (MCP) detector and the muon beam profile monitor (MBPM). The hit rate and the beam profile of the muon were measured. Using this beam-line, the 1S-2S energy interval of the muonium is also measurable towards the precise determination of muon mass.

This work started with the development of end-to-end simulation. Softwares such as Geant4 and Opera were used to simulate the behavior and estimate the muon and muonium generation efficiency in each stage (surface muon transport in the beam-line, muonium diffusion inside the aerogel target, muonium emission in the vacuum, and the re-acceleration of thermal muon). The hit rate of the thermal muon at the detector was estimated. Moreover, a series of hardware preparations were done on the SMBL, including the assembly of accelerator components, alignment of the beam-line, operation test on the vacuum and high voltage system, upgrade on the control system, and design of the data acquisition systems, etc. Finally, the laser system was combined with the beam-line to take the data.

The signal of thermal muon at the MCP detector was successfully observed, confirming

the thermal muon production. The beam properties were carefully measured with the optimized optics. The efficiency of the Mu generation was calculated and consistent with the simulation prediction. The laser detuning curve and the resonance frequency with the width obtained in our study were consistent with the past experiment (at RAL, 1999). Our ionized muon rate was higher than that of the past experiment by a factor of 43.

Regarding the second issue, we proposed a multi-target silica aerogel design based on the current single-layer design. This design generates Mu inside the multi-layer silica aerogel targets facing the injecting surface muon beam to increase Mu emission efficiency. Mu is confined in a vacuum between the aerogel pieces by reflecting on the target surfaces. Our study started by modeling Mu diffusion inside the aerogel and the extension to the Mu confinement in multi-layer geometry. Combined with the laser ionization simulation, the entire Mu motion was described. By Monte-Carlo simulation, the thermal muon generation efficiency was studied. The geometry was optimized to increase the intensity of Mu by more than three times that of the current (single-layer) design. The development toward the realization of this design is ongoing.

All the works above fully confirmed the thermal muon generation and studied its properties. Considering the upstream muon intensity, the thermal muon after laser ionization and initial acceleration is estimated in the E34 experiment, giving the final muon intensity in the storage detector about 2×10^5 Hz. It is the milestone of the E34 experiment. Such intensity satisfies the a_μ precision of 0.45 ppm in the first stage of the experiment. Given the help of the multi-target design, the muon intensity in the final stage is expected to be enhanced by a factor of three to four, improving the precision by approximately two times and offering an opportunity toward the E34 final target of 0.1 ppm.

KEY WORDS: Muon $g-2$, thermal muon, muonium, laser ionization

Contents

Acronyms

BM	bending magnet
BNL	Brookhaven National Laboratory
DAQ	data acquisition
E34	Muon $g-2$/EDM experiment
ED	electric deflector
EDM	Electric Dipole Moment
EPICS	Experimental Physics and Industrial Control System
EQ	electric quadrupole
FNAL	Fermi National Accelerator Laboratory
Geant	Geometry and Tracking
HV	high voltage
J-PARC	Japan Proton Accelerator Research Complex
LHC	Large Hadron Collider
LINAC	linear accelerator
MCP	micro-channel plate
MLF	Materials and Life Science Experimental Facility
Mu	muonium
MUSE	The muon science facility
NMR	Nuclear Magnetic Resonance
QED	quantum electrodynamics
QCD	quantum chromodynamics
PMT	Photomultiplier Tube
ppb	parts per billion
ppm	parts per million
RFQ	The Radio Frequency Quadrupole
RIKEN-RAL	RIKEN-Rutherford Appleton Laboratory
RMS	root mean square
SM	Standard Model
SMBL	slow muon beam-line

1 Introduction

1.1 Magnetic moment and electric dipole moment of muon

1.1.1 Magnetic moment and muon anomaly

For an elementary particle that does not possess any internal structure, its magnetic moment[1] $\vec{\mu}$ is given by

$$\vec{\mu} = g_s \frac{e}{2m} \vec{S} \tag{1.1}$$

where m is the mass, e the charge and $\vec{S}$ the spin angular momentum, which is quantized with magnitude $\hbar/2$. The gyro-magnetic ratio g_s (also known as g-factor) describes particle's magnetic moment resulting from its spin $\vec{S}/\hbar$ in the unit of Bohr magneton ($\mu_B = \frac{e\hbar}{2m_e}$).

Classically, if the charged particle is rotating without spin, the spin momentum is replaced with the orbital angular momentum $\vec{L}$, which leads to orbital g-factor $g_L = 1$. But the intrinsic spin angular momentum $\vec{S}$ gives the spin g-factor approximately $g_s \approx 2$, twice as it in the classical mechanics[2]. It was firstly explained by Dirac[3] who found that $g = 2$ came out naturally by solving the Dirac equation for the relativistic spin-$\frac{1}{2}$ elementary particles (in the natural units):

$$(i\partial\!\!\!/ - m)\psi = 0 \tag{1.2}$$

It implies that the Dirac particle produces a magnetic moment twice as effective as its classical charged body. But such a statement was again challenged when experiment[4] found that the measured magnetic moment of the electron differed from 2 by a small fraction of a percent. It was later understood as the quantum fluctuations of the electromagnetic field around the particle at higher orders. As quantum field theory progressed, the contributions from those radiative corrections were calculated. $g = 2$ is the tree-level prediction of the QED diagram where a virtual photon directly interacts with the lepton. In 1948, Schwinger gave the calculation[5] on the first-order correction to g by exactly α/π, where α is the fine-structure constant.

The difference is now referred to as "anomalous magnetic moment". For charged leptons ($l = e, \mu, \tau$), the magnetic anomaly a_l is defined as

$$a_l = (g_l - 2)/2 \tag{1.3}$$

By studying such anomaly, the discrepancy between the theoretical value a_l^{SM} and the experimental measurement a_l^{EXP} may be contributed by the new physics (NP) beyond the Standard Model (SM) through the unknown particles:

$$a_l = a_l^{\mathrm{SM}} + a_l^{\mathrm{NP}} \tag{1.4}$$

For electron, the study of its anomaly, a_e, gives the most precisely measured quantities in particle physics and the most accurate calculation in the SM theory. The recent experimental values of a_e were reported from different groups[6–8]. One of the latest experiment results is $a_e^{\mathrm{EXP}} = 1.159\,652\,180\,73(28) \times 10^{-3}$ with the precision of 0.28 ppt[8].

For muon, which behaves like a heavy electron, its anomaly a_μ has a special role. Given the existence of the new physics particle with mass $\mathrm{M_{NP}}$, its effects could be enhanced via the muon mass[9]:

$$\delta a_\mu \propto \frac{m_l^2}{M_{NP}^2} \tag{1.5}$$

Compared with an electron, muon is more sensitive to the possible new physics by a factor of $(m_\mu/m_e)^2 \approx 4.3 \times 10^4$. On the other hand, compared with τ, the last generation of the leptons[10], muon has a relatively reasonable lifetime to be stored. In the lepton family, muon is the best probe for the new physics.

1.1.2 Electric dipole moment

An external magnetic field will exert a torque on the magnetic moment, yielding potential energy and the electric dipole moment (EDM)[11] in the electric field. The Non-relativistic Hamiltonian for the spin-$\frac{1}{2}$ particle in the external electromagnetic field is

$$H = -\vec{\mu} \cdot \vec{B} - \vec{d} \cdot \vec{E} \tag{1.6}$$

where the electric dipole moment (EDM) $\vec{d} = \eta(\frac{e}{2mc})\vec{S}$.

EDM is not usually considered in the elementary particles since it violates both time-reversal symmetry (T) and parity inversion (P), as shown in Table 1.1. Nevertheless, a non-zero EDM of the fundamental particle will directly indicate CP-violation (the combined symmetry of charge and parity).

In the SM, the only source of CP violation is the Kobayashi-Maskawa (KM) phase[12], which only appears in the coupling between the quark and the W boson. Studies in[13, 14]

表 1.1 电场、磁场与电二极矩（$\vec{\mu}$ 或 $\vec{d}$）的 CPT 对称性。在 $\vec{d}\cdot\vec{E}$ 一项中，P 与 T 对称性被破坏。

Table 1.1 CPT symmetries in the magnetic dipole moments and electric dipole moments. P and T are violated in the $\vec{d}\cdot\vec{E}$ term.

	$\vec{E}$	$\vec{B}$	$\vec{\mu}$ or $\vec{d}$
P	−	+	+
C	−	−	−
T	+	−	−

suggested that for the electron to receive a non-zero EDM contribution, at least four-loop diagrams are needed, which also apply to the muon EDM with obvious modifications of $m_e \to m_\mu$. In Ref.[13], the size of the four-loop contribution to the electron EDM d_e(SM) is estimated as

$$d_e(\mathrm{SM}) \sim 8 \times 10^{-41}\ e \cdot \mathrm{cm} \tag{1.7}$$

which further gives the SM prediction for the muon EDM d_μ(SM) to be

$$d_\mu(\mathrm{SM}) \sim \frac{m_\mu}{m_e} d_e(\mathrm{SM}) \sim 2 \times 10^{-38}\ e \cdot \mathrm{cm} \tag{1.8}$$

The latest measurement[15] was done using BNL muon g-2 experiment data, which gave the uplimit of the muon EDM d_μ(exp.)

$$d_\mu(\mathrm{exp.}) \leq 1.9 \times 10^{-19}\ e \cdot \mathrm{cm} \tag{1.9}$$

The discovery of non-zero d_μ above the d_μ(SM) will be direct evidence of new physics beyond the SM.

1.1.3 Theoretical prediction on muon $g-2$

In the SM, muon interacts with all kinds of the particles in three main sectors[16]: the QED contribution, the electric-weak contribution and the hadronic contribution:

$$a_\mu^{\mathrm{SM}} = a_\mu^{\mathrm{QED}} + a_\mu^{\mathrm{EW}} + a_\mu^{\mathrm{Hadronic}} \tag{1.10}$$

Examples of the processes are shown in Figure 1.1. The QED contribution has been analytically determined up to 5 loops among all the contributions. Now, the most problematic

terms lie in the hadronic interactions: the hadronic vacuum polarization (HVP) and the hadronic light-by-light scattering (HLBL), as shown in Figure 1.2.

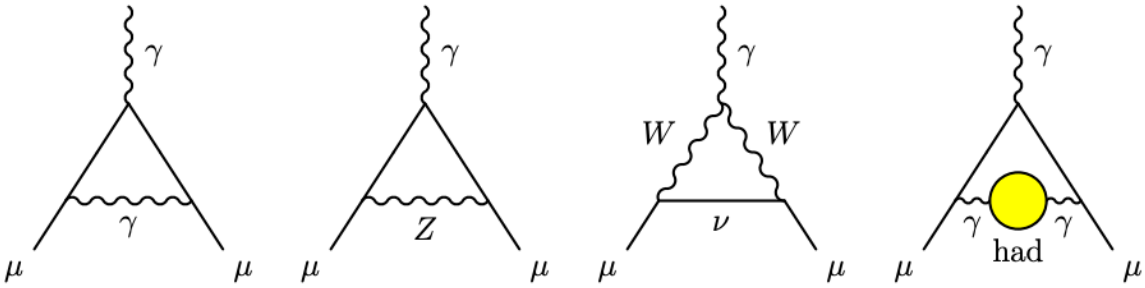

图 1.1　缪子反常磁矩相关的费曼图。从左到右分别是量子电动力学（QED）、电弱相互作用和强子的贡献。图片来自[1]。

Figure 1.1　Feynman diagrams of SM contributions to a_μ. The diagrams shown (from left to right) are first order QED (Schwinger $\alpha/2\pi$ term), the one-loop EW process involving Z-boson and W-boson exchange and the hadronic contributions. From Reference[1].

To calculate the hadronic processes, the usual method of the perturbative QCD is not applicable at low energy. Either lattice QCD (LQCD) or the experimental data input is needed. Regrading low mass meaons with π, η, and η', the measurement from the e^+e^- collision gives the prediction through the optical theorem. The contribution is proportional to the cross-section $\sigma(e^+e^- \to \text{hadrons})$.

A dedicated collaboration, "The muon $g-2$ theory initiative"[17], was established for the theoretical calculations in the light of combining the experimental data as the input into the theory. Meanwhile, the Lattice QCD method has also progressed recently[18], whose result is now under investigation on its consistency with SM.

The latest SM prediction[16] is given as

$$a_\mu^{\text{SM}} = 1.165\,918\,10(43) \times 10^8 \times 10^{-11} \tag{1.11}$$

1.1.4　New physics in light of muon $g-2$

The discrepancy of a_μ can be contributed by the new physics (NP) beyond the Standard Model (SBM), indicating new particles and new interactions. NP scale M_{NP} is determined by the size of the NP couplings to muon g_{NP}[19]. Given the 4.2σ discrepancy, the NP mass scale is estimated to be

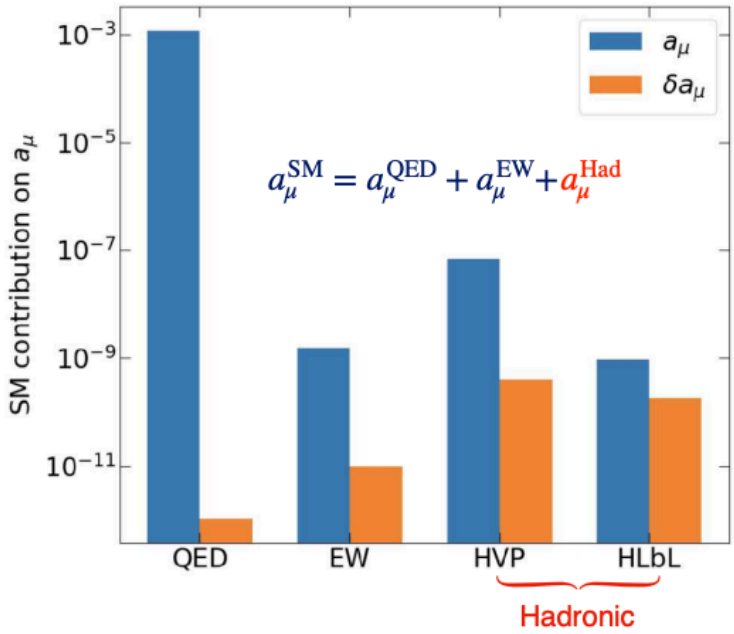

图 1.2　对缪子反常磁矩有贡献的各个过程的理论误差。横轴从左到右分别是量子电动力学（QED）、电弱相互作用、强子真空极化和强子光子-光子散射过程。其中后两者在理论误差中占主要贡献。图片来自[1]。

Figure 1.2　Uncertainties in the various contributions to a_μ, among which the HVP and HLbL terms are dominant. From Reference[1].

$$\Delta a_\mu = a_\mu^{\text{BNL+FNAL}} - a_\mu^{\text{SM}} = (25.1 \pm 5.9) \times 10^{-10} = \frac{m_\mu^2}{16\pi^2}\frac{g_{\text{NP}}^2}{M_{\text{NP}}^2} \tag{1.12}$$

Such naive estimation gives the $M_{\text{NP}} \sim g_{\text{NP}} \times 150$ GeV, around the EW scale. If g_{NP} is large by certain mechanisms such as chiral enhancement[20], TeV scale NP models are needed to explain the anomaly. If g_{NP} is small ($g \sim 10^{-3}$), MeV scale NP models are favorite. For example, the popular supersymmetry (SUSY) model[21] gives several types of one-loop diagrams responsible for explaining muon anomaly and proportional to SM parameter tanβ[19]. It results in an effectively large g_{NP} in the TeV scale. Other models and their NP particle mass scale involving Axion-like particle (ALP) and dark-photon models are discussed in References[22, 23].

1.1.5 Experiments on muon $g-2$: FNAL and J-PARC

There has been a long history since the 1960s of the experimental measurement of a_μ. The storage ring method was applied at CERN[24] for the first time, and the measurement was inherited by Brookhaven National Laboratory (BNL-E821)[25] and Fermi National Accelerator Laboratory (FNAL-E989) experiments[26].

The principle of those experiments involves the spin precession of polarized muon relative to its orbital momentum at the magnetic field[27]. The muon spin rotates with the angular frequency (Larmor precession together with the Thomas precession in the relativistic treatment) ω_s while the orital frequency is ω_c:

$$\omega_S = \frac{e}{m\gamma}[\frac{1}{\beta}(\vec{N} \times \frac{\vec{E}}{c}) - \vec{B}] \tag{1.13}$$

$$\begin{aligned}\omega_C = -\frac{e}{m}[(\frac{g-2}{2} + \frac{1}{\gamma})\vec{B} - (\frac{g-2}{2}\frac{\gamma}{\gamma+1})(\vec{\beta}\cdot\vec{B})\vec{\beta} - (\frac{g-2}{2} + \frac{1}{\gamma+1})(\vec{\beta}\times\frac{\vec{E}}{c}) \\ + \frac{\eta}{2}(\frac{\vec{E}}{c} - \frac{\gamma}{\gamma+1}(\vec{\beta}\cdot\frac{\vec{E}}{c})\vec{\beta} + \vec{\beta}\times\vec{B})]\end{aligned} \tag{1.14}$$

where the γ stands for the relativity factor of the muon in the lab frame. The spin ω_s precesses slightly bigger than ω_c by the difference defined as ω_a

$$\omega_a = \omega_s - \omega_c \tag{1.15}$$

The analytic expressions is further simplified by considering condition of $\vec{B}\cdot\vec{\beta} = 0$ and

$\vec{E} \cdot \vec{\beta} = 0$, meaning the particle is orbiting precisely perpendicular to the field:

$$\vec{\omega_a} = -\frac{e}{m}[a_\mu \vec{B} - (a_\mu - \frac{1}{\gamma^2 - 1})\frac{\vec{\beta} \times \vec{E}}{c} + \frac{\eta}{2}(\vec{\beta} \times \vec{B} + \frac{\vec{E}}{c})] \tag{1.16}$$

where the a_μ term stands for the magnetic moment while the η term stands for the EDM.

Starting from Equation 1.16, there are two approaches toward the experimental measurement of a_μ. One of the approaches utilized by FNAL and BNL is introduced in Section 1.1.5.1. In contrast, the other approach for the J-PARC E34 experiment is introduced in Section 1.1.5.2.

1.1.5.1 FNAL approach and its Run-1 result

In the FNAL experiment as well as the previous BNL experiment, the 'magic γ' was used to eliminate the terms including a_μ in Equation 1.16. Given the γ of 30 (muon momentum of P = 3 GeV/c), it makes $a_\mu = \frac{1}{\gamma^2 - 1}$. The frequency ω_a is simplified as

$$\vec{\omega_a} = -\frac{e}{m}[a_\mu \vec{B} + \frac{\eta}{2}(\vec{\beta} \times \vec{B} + \frac{\vec{E}}{c})] \tag{1.17}$$

Considering the uniform magnetic field perpendicular to the storage ring plane, the frequency ω_a becomes:

$$\vec{\omega_a} = -\frac{e}{m}[a_\mu \vec{B} + \eta \frac{\vec{E}}{2c}] \tag{1.18}$$

a_μ is determined given the magnetic field B and the precession frequency ω_a perpendicular to the storage ring measured.

To measure the precession frequency, the muon events are stored in the storage ring with a magnetic field until it decays. The highly-polarized muon decays into positron and neutrino. The positron emission angle follows the Michel spectrum[28]:

$$\frac{d\Gamma}{d\cos\theta} \sim 1 + \frac{1}{3} P_\mu \cos\theta \tag{1.19}$$

where θ is the angle of the positron momentum relative to the muon spin vector and P_μ is the muon momentum. Following this distribution, the positron with the highest energy tends to emit towards the spin direction, as shown in Figure 1.3.

Following this principle, the experiment at BNL and FNAL utilized the storage ring with a diameter of 14 m and a magnetic field of 1.45 T[30]. Calorimeters around the storage ring detect the decay positrons from muon. Since the spin of muon keeps precession at the fixed position, the number of positrons above a certain threshold evolves by frequency ω_a:

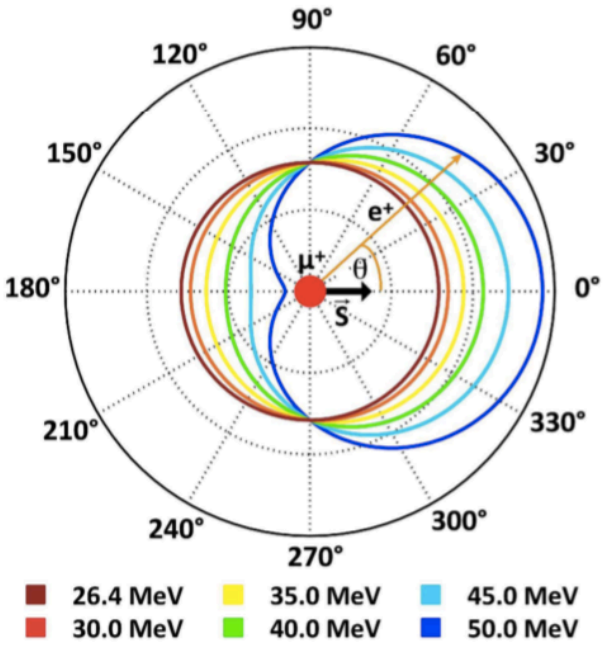

图 1.3　从缪子衰变的正电子将服从米歇尔谱分布。在此分布中，能量最高的正电子将倾向于从缪子自旋方向出射。图片来自[29]。

Figure 1.3　Positrons from the muon decay follows the Michel spectrum. Positrons with the highest energy tends to emit in the direction of the muon spin. From Reference[29].

$$N(t) = N_0 e^{-t/\tau}[1 + A_\mu \cos(\omega_a t + \phi)] \tag{1.20}$$

The schematic is shown in Figure 1.4. By fitting the wiggle plot, the precession frequency ω_a is obtained, as shown in Figure 1.5.

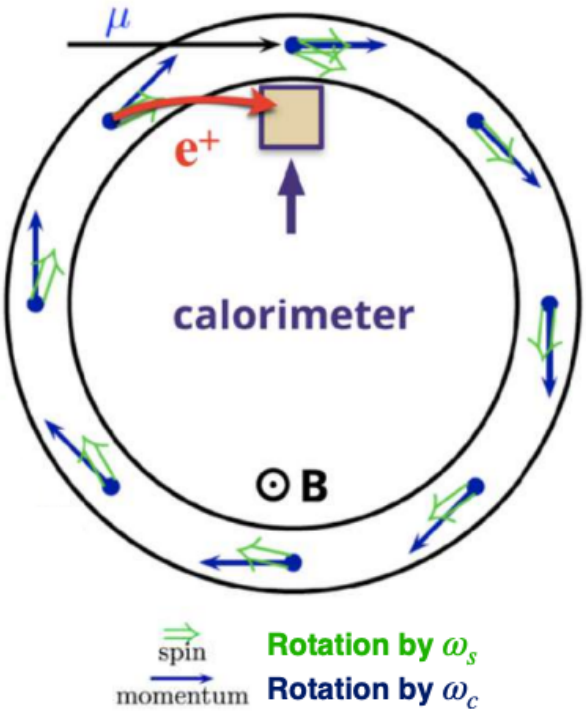

图 1.4 缪子被注入储存环中，并在垂直于储存环的磁场下绕环运动。其自旋方向与动量方向间的夹角呈周期变化。衰变的正电子将被量能器探测。图片来自[2]。

Figure 1.4 Muons are injected into the storage ring, where the B field is applied. The angle between the muon spin direction and the momentum direction varies periodically. The number of positrons is counted by the calorimeter. From Reference[2].

Such experiment was conducted at BNL from 1997 to 2001, then a new experiment at FNAL started from 2016 and published Run-1 result on April, 2021. Their measurements yields:

$$a_\mu^{\mathrm{BNL}} = 1.165\,920\,92(63) \times 10^8 \times 10^{-11} \tag{1.21}$$

$$a_\mu^{\mathrm{FNAL(RUN-1)}} = 1.165\,920\,40(54) \times 10^8 \times 10^{-11} \tag{1.22}$$

The BNL measurement reached the precision of 0.54 ppm while FNAL RUN-1 reached

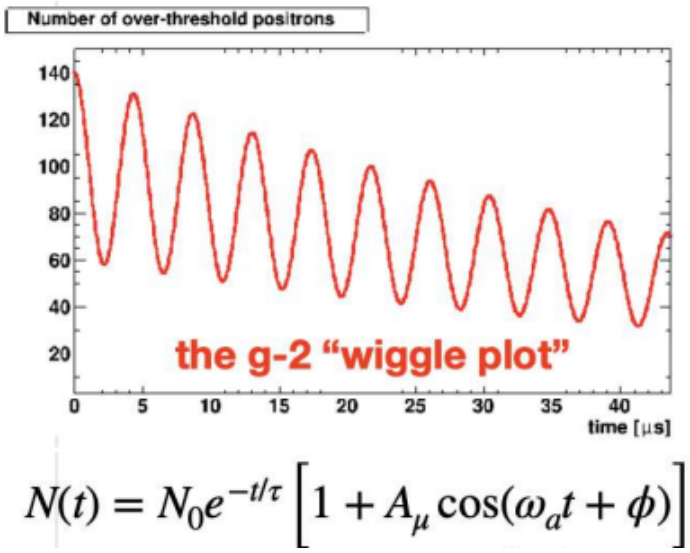

图 1.5　量能器测得的正电子数目随着时间的变化关系（正电子选取特定的能量阈值之上）。从拟合中可以得到频率 ω_a 的测量结果。图片来自[2]。

Figure 1.5　The typical wiggle plot, showing the evolution of the number of positrons above the selected threshold. ω_a is obtained from the parameters fitting. From Reference[2].

0.46 ppm. Their combined result gives the most precise experimental measurement on a_μ so far:

$$a_\mu^{\mathrm{EXP}} = 1.165\,920\,61(41) \times 10^8 \times 10^{-11} \tag{1.23}$$

with the precision of 0.35 ppm.

The current status of the measurement result is summarized in Figure 1.6 and Table 1.2.

表 1.2　缪子反常磁矩的实验测量与理论总结

Table 1.2　Summary on the current status of the a_μ measurement and theoretical prediction.

a_μ	result [$\times 10^{-11}$]	precision [ppm]
a_μ^{BNL}	$1.165\,918\,10(43) \times 10^8$	0.54
$a_\mu^{\mathrm{FNAL(RUN-1)}}$	$1.165\,920\,40(54) \times 10^8$	0.46
a_μ^{EXP}	$1.165\,920\,61(41) \times 10^8$	0.35
a_μ^{SM}	$1.165\,918\,10(43) \times 10^8$	0.37

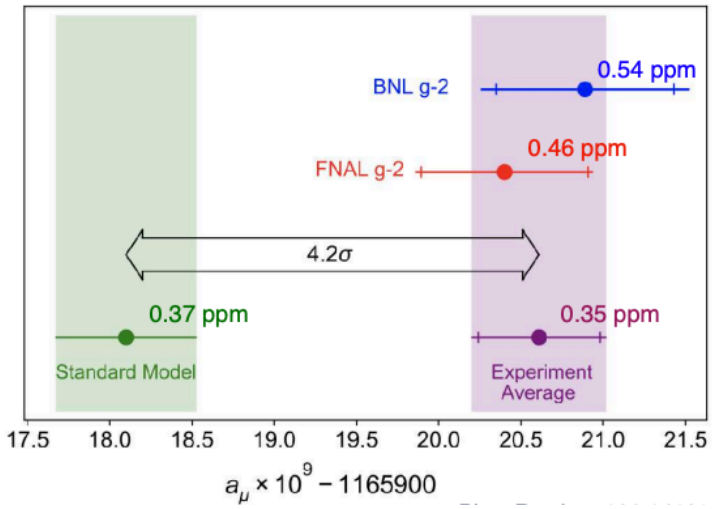

图 1.6　费米实验 RUN-1 的缪子反常磁矩测量值与理论现状。结果来自[30]。

Figure 1.6　Comparison on the a_μ measurements as of April 2021 with SM prediction. From Reference[30].

1.1.5.2　J-PARC E34 approach

On the other hand, the Muon $g-2$/EDM experiment (E34) proposed at J-PARC[31] uses a different approach from FNAL, aiming to measure a_μ with a statistical precision of 0.1 ppm, and muon EDM with the uplimit of $1.5 \times 10^{-21}\ e \cdot \mathrm{cm}$.

For the J-PARC experiment, the E-field is directly removed in Equation 1.16, which becomes:

$$\vec{\omega}_a = -\frac{e}{m}[a_\mu \vec{B} + \frac{\eta}{2}(\vec{\beta} \times \vec{B})] \tag{1.24}$$

The experiment can be conducted at any γ with zero E-field. However, it is very challenging to contain the muon beam with reasonably small emittance without the existence of the electric field, since muons originated from isotropically pion decay. The widely-used surface muon beam (positive) is made by collecting muons with the energy of approximately 4 MeV from stopped pion decay and has a typical energy spread of several hundred keV. The beam is soon lost during transport without a focusing field.

Regarding this issue, the J-PARC E34 experiment plans to utilize the thermal muon beam, a source of room-temperature muons. In this scheme, the 100% polarized surface muons from one of the J-PARC muon beam-line, H-line[32] are converted into a thermal muon (or known as ultra-cold muon) with 50% polarization by laser ionization of muonium (μ^+e^- atom, or Mu).

Such thermal muon has low kinetic energy at room temperature and can be re-accelerated to high energy with small emittance contained.

Following the thermal muon generation, the SOA lens[33] is used to accelerate the thermal muon to 5.6 keV initially. The muon LINAC, consisting of several accelerator components, accelerates muon until 212 MeV. The re-accelerated muon beam is 3D-spirally injected into the solenoid storage ring with a locally uniformed magnetic field with an uncertainty of less than 1 ppm. The silicon strip detectors detect muon orbits with a diameter of 66 cm and the decay positrons assembled in the center. The experiment overview is shown in Figure 1.7.

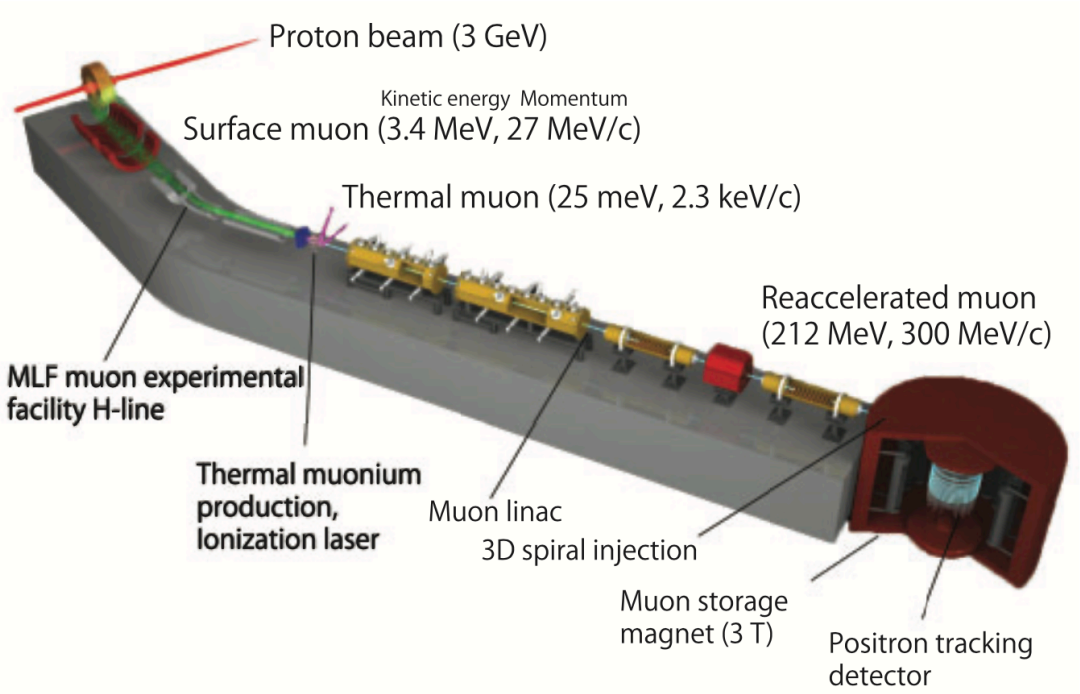

图 1.7　J-PARC 缪子反常磁矩与电二极矩实验总览[31]。

Figure 1.7　The overview of the muon $g-2$/EDM experiment at J-PARC MLF[31].

By re-accelerating, the thermal muon source, the emittance of the muon is reduced to approximately 1000 times smaller than that of the conventional muon beam. The production of the thermal muon source is a crucial step, and its development is the main content of this thesis.

The comparison of the BNL-E821, FNAL-E989 experiments, and J-PARC E34 experiment is in Table 1.3.

表 1.3 缪子反常磁矩测量相关实验比较

Table 1.3 Comparison on the muon $g-2$ experiments

Experiment	BNL-E821 and FNAL-E989	J-PARC-E34
Muon momentum	3.09 GeV/c	300 MeV/c
Muon polarization	100%	50%
Storage (B) field	1.45 T	3.0 T
Focusing field in the storage ring	Electric quadrupole	Very weak magnetic
Cyclotron period	149 ns	7.4 ns

1.2 Thermal muon production via laser ionization of muonium

Muonium (Mu)[34] is a purely leptonic system consisting of a positive muon and an electron. Since its discovery[35], it has been widely used in precision measurements to determine fundamental constants such as muon mass and fine structure constant[36]. Using laser ionization, Mu can be converted into sub-eV thermal muons in vacuum[37, 38]. Acceleration of thermal muons provides a promising way of generating a low energy μ^+ beam with better quality than the traditional surface muon beam.

An alternative method to improve the muon beam quality is to use a cryogenic degrader to produce keV muons, known as the Low Energy Muon (LEM) beam accomplished at Paul Scherrer Institute (PSI)[39]. A novel scheme of utilizing the space compression method for the development of a low-energy bright muon beam with an efficiency of 10^{-3} per surface muon is also under progress[40].

Recently, there have been developments in silica aerogel material for Mu generation in vacuum at TRIUMF[41–43]. The Mu was produced from aerogels in a clean vacuum and room temperature environment with a typical kinetic energy of only 0.02 eV (thermal energy), an order of magnitude lower than that of hot tungsten (2300 K).

Such thermal muon via Mu laser ionization is the most innovative technique proposed in the J-PARC E34 experiment. The scheme of the entire re-accelerated thermal muon beam is summarized in Figure 1.8. Surface muon with the momentum of 28 MeV/c is firstly generated by proton beam (3 GeV) at J-PARC Materials and Life Science Facility (MLF). Starting from the muon target, surface muons are collected by the H-line solenoid and transported into the silica aerogel position, where they capture an electron and form Mu atoms. Some Mu atoms diffuse into the vacuum, where they are ionized by laser and converted into a thermal muon for further acceleration by muon LINAC.

The entire scheme is divided into several stages: Mu generation inside silica aerogel,

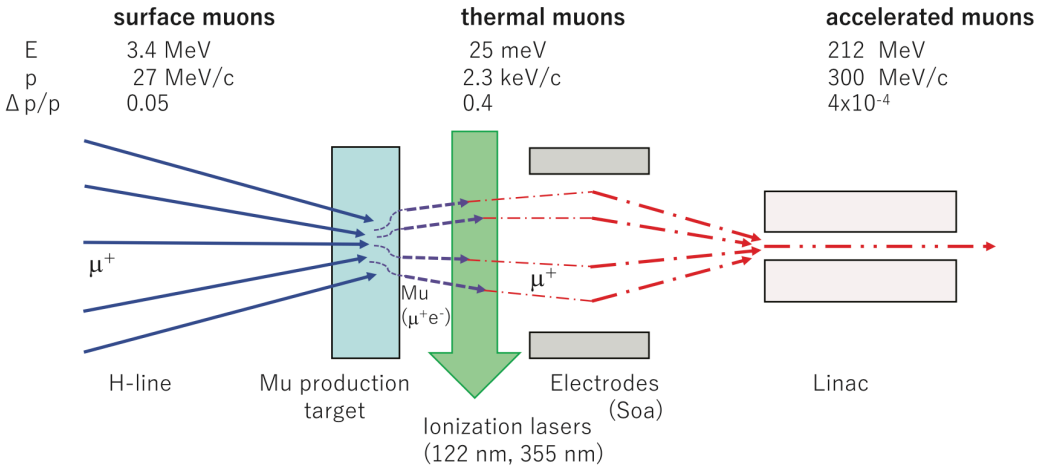

图 1.8　缪子素激光电离制备热缪子方法概览[31]

Figure 1.8　Overview on the Mu ionization scheme for thermal muon generation[31]

laser ionization of the Mu in a vacuum, and thermal muon re-acceleration. These stages are explained in step by step in Sections 1.2.1, 1.2.2 and 1.2.3.

1.2.1　Mu generation inside silica aerogel

Thermal Mu is typically generated in a vacuum by implanting positive muon beams into materials such as hot tungsten[44], silica powder[45], or mesoporous SiO_2[46].

The scheme of the muonium 1S-2S laser ionization originated back in 1986 by S. Chu and K. Nagamine in[47] when silica powder was used for the first time. Hot tungsten was another choice. Among those choice, silica powder has a relatively higher Mu production efficiency of approximately 19% at 300K, while hot tungsten foil of approximately 4%. However, silica powder, consisting of micrometer particles, is unstable in the accelerator vacuum, and hot tungsten has difficulty being used at room temperature. A new choice of silica aerogel satisfies the requirement of a stable and self-supporting material for room-temperature Mu production in a vacuum for the J-PARC E34 experiment.

In a series of tests of aerogel materials at TRIUMF, Mu emission from silica aerogel was observed at room temperature[41] and further studies[42, 43] indicated that the laser ablation on the aerogel surface helped to enhance emission by order of magnitude. The laser-ablated aerogel sample with the best yield was identified as a pattern of laser-ablated holes with a pitch of 300 μm and a diameter of 270 μm.

The experimental setup is shown in Figure 1.9. Using the DC muon beams at TRIUMF,

Mu atoms emerged from the downstream surface of the aerogel sample. Mu signals were observed by detecting the positrons from Mu decay in the surrounding positron tracker. The detectors recorded both position and time of muon decay. Positions were measured by extrapolating the drift chamber track positions to the target region. The number of Mu emissions in the various areas of the vacuum (10-mm-wide regions from 10 to 40 mm from the target surface) was determined, as shown in Figure 1.10.

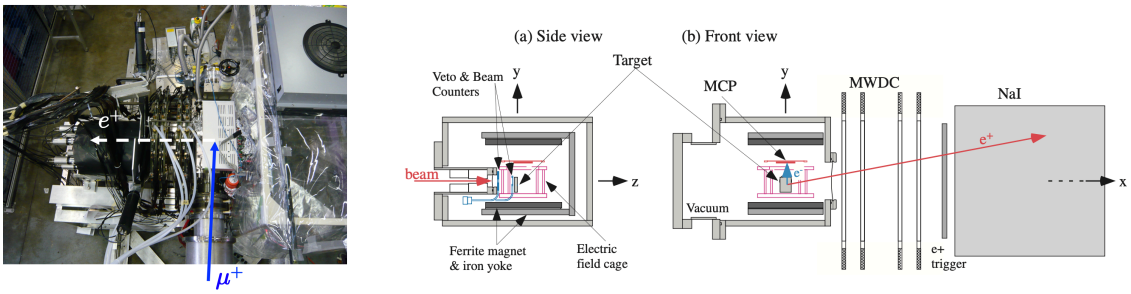

图 1.9 缪子素在硅凝胶材料中的生成实验设置（TRIUMF）[41]

Figure 1.9 Setups in the TRIUMF experiment for Mu emission from silica aerogel[41]

Figure 1.11 shows one of the laser-ablated aerogel samples tested in[42, 43]. A non-uniform surface on aerogel slabs with the micrometer hole structure was created by laser ablation to increase the total surface area of the aerogel. It helped to enhance emissions by order of magnitude. Maximum Mu vacuum yields of 0.3% and 3% were observed respectively on flat silica aerogel and silica aerogel with laser-ablated holes on the surface, as shown in Figure 1.10.

1.2.2 Laser ionization

Mu emitted from the downstream surface of the aerogel is ionized by laser. From the Mu spectroscopy shown in Figure 1.12, the ionization schemes are possible in two ways: from 1S-2S excitation to ionization or from 1S-2P excitation to ionization. The latter was preferred in the E34 original design. Nevertheless, two laser systems are currently under development: the 122 nm Lyman-α laser to excite the Mu from the ground (1S) to the 2P state and the 244 nm laser for 1S-2S excitation. In addition, a 355 nm laser is also on the way to ionize the excited Mu.

E34 experiment assumes the following parameters for 122 nm laser: power per pulse 100 μJ, pulse length two ns, spot size 2 cm^2. The expected laser ionization efficiency is about 73% per Mu in the laser-irradiated region. However, such an intense 122 nm Lyman-α laser design is challenging to reach high power and high ionization efficiency.

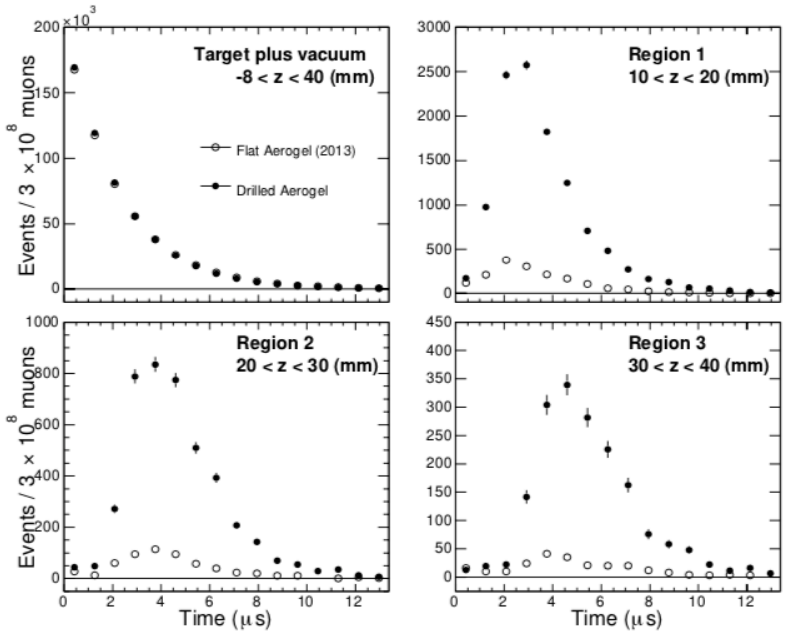

图 1.10　TRIUMF 实验中缪子素在真空中的数量的时间分布。真空区域按照距离硅凝胶靶材料的距离分为三个区域（从 10 厘米到 40 厘米）。图中白色数据点代表缪子素从非激光蚀刻的硅凝胶表面溢出的数量，黑色数据点代表其从激光蚀刻的硅凝胶表面溢出的数量。本图来源于文献[42]。

Figure 1.10　Time distributions of positrons in the entire target region and in each of three vacuum regions in the TRIUMF experiment, Mu emission was significantly enhance from the flat aerogel (open circles) to laser-ablated aerogel(closed circles). This Figure is from Ref.[42].

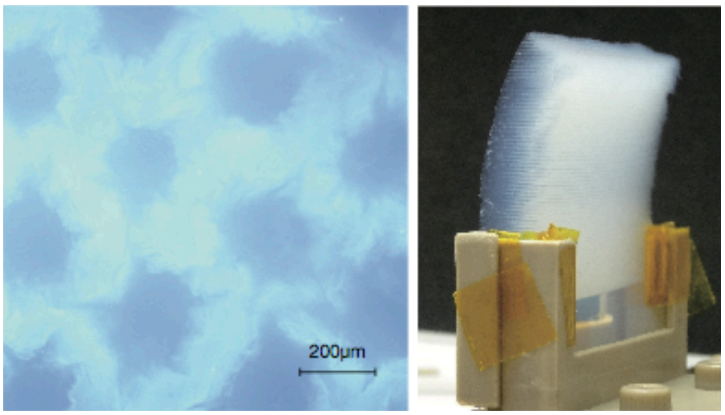

图 1.11　TRIUMF 实验中所用硅凝胶样品（表面经过激光蚀刻）[42]

Figure 1.11　Example of aerogel sample with laser-ablation on its surface used in the TRIUMF experiment[42]

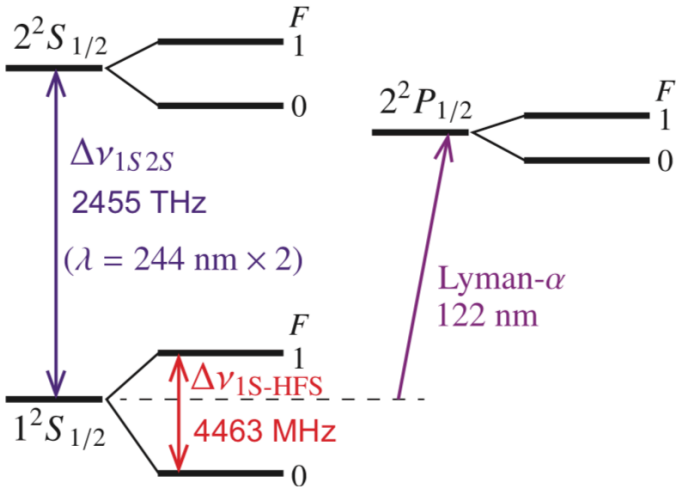

图 1.12　缪子素能谱。122 纳米波长激光能将缪子素从 1S 激发至 2P 态。244 纳米波长激光能将缪子素从 1S 态激发至 2S 态。

Figure 1.12　Mu spectroscopy. 122 nm laser excites Mu from 1S to 2P state while 244 nm laser excite Mu from 1S to 2S state.

The laser system is generated by a non-linear conversion in Kr gas from two pump laser beams, followed by four stages of amplifiers and three stages of frequency converters with nonlinear optical crystals[31], as shown in the Figure 1.13. The laser system is currently under development at J-PARC U-line[48]. The energy of only about 3 μJ and a laser width of about 3 mm are achieved, which is still lower than the targeted design.

Regarding 1S-2S excitation via 244 nm laser, the two-photon excitation process is generally considered low efficiency compared with one-photon excitation. But it is produced in a simpler scheme and applicable for a quick demonstration of the Mu ionization scheme before constructing the E34 experiment. Table 1.4 summarizes the features of both 122 nm laser and 244 nm laser. More features of the 244 nm laser will be discussed in Chapter 2 and 4.

1.2.3 Re-accelerated thermal muon

Thermal muon generated from Mu laser ionization needs to be re-accelerated. At the initial vacuum region where the laser is shot, there are two parallel meshes plates at the downstream surface of the aerogel and 10 mm away from the surface, respectively. High voltages (HVs) are applied to the meshes, providing the uniform E field to extract the thermal muon. After meshes, the SOA lens is set, consisting of several cylindrical structures with different thicknesses and diameters. They are applied with different voltages. The intervals between the lens provide the electric fields to accelerate the thermal muon. The muon beam is

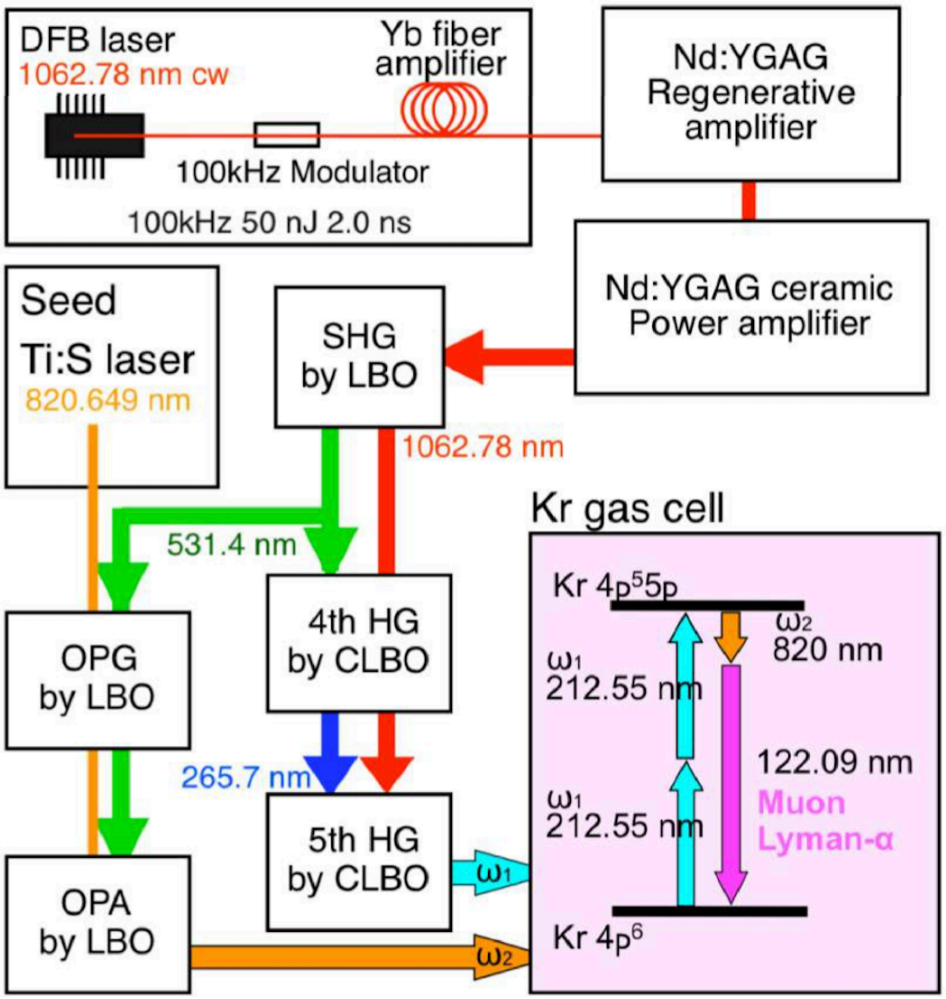

图 1.13　122 纳米波长激光制备概览[31]

Figure 1.13　Desgin of the 122 nm Lynman-α laser system for E34 experiment[31]

表 1.4　缪子激光电离中所用不同波长激光的比较

Table 1.4　Comparison on the laser systems applicable for Mu ionzation experiment

Laser type	122 nm	244 nm
Ionization scheme	One photon excitation	Two-photon excitation
Typical energy	3 uJ	3 mJ
Line width	3 mm	a few mm
Target energy	100 uJ	Under investigation
Target irradiation area	5×40 mm^2	Under investigation
Target ionization probability①	68%	-

① Assuming same 355 nm laser for ionization

focused along the way. The scheme is shown in Figure 1.14.

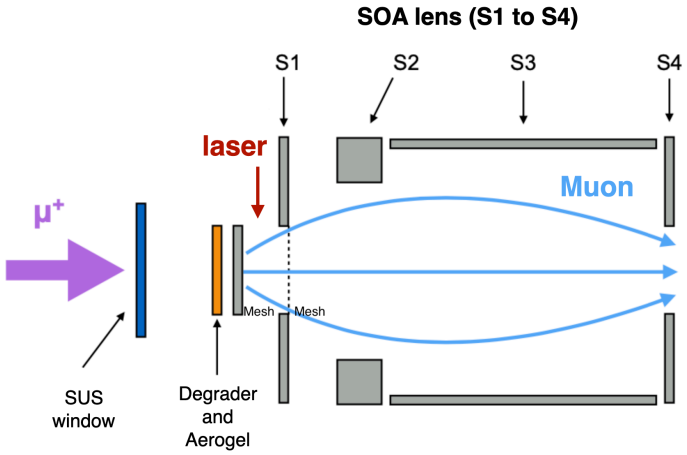

图 1.14 SOA 对热缪子进行初级加速

Figure 1.14 SOA lens for initial acceleration of thermal muon

1.3 Current issues on thermal muon source development

The scheme of the thermal muon generation via laser ionization of Mu from silica aerogel is the first of its kind globally. There are two main issues in this context:

- **The scheme has not yet been validated** through a prototype setup. Mu emission from silica aerogel was confirmed in TRIUMF experiments, but its ionization was yet missing. The properties of the thermal muon (its beam profile, emittance, energy and time spread, etc.) and, most importantly, its generation efficiency need careful study before the scheduled E34 data taking (2027 and beyond).
- **Pursuit of sensitivity of 0.1 ppm on a_μ requires higher muon intensity**. Thermal muon production efficiency estimated by simulation is approximately 0.034 per injecting surface muon, the lowest in the breakdown of E34 efficiencies[31]. An order of magnitude improvement from the current intensity is considered a milestone toward 0.1 ppm.

Regarding the first issue, we proposed the prototype of the Mu ionization experiment with a 244 nm pulsed laser. A slow muon beam-line (SMBL) was prepared to extract thermal muon to the MCP detector to detect thermal muon and study its properties. The project is not only a quick demonstration of the E34 scheme but is also regarded as the Phase-0 for Mu 1S-2S spectroscopy, aiming to measure the muonium 1S-2S energy interval and therefore the muon

mass to an unprecedented precision[49].

Regarding the second issue, a novel and original idea for multi-layer silica aerogel targets design were proposed in this thesis for the higher thermal muon intensity. Mu generated in the multi-layer aerogel targets emits into the sandwiched vacuum regions. It is confined in a vacuum between aerogel slots separated by a few mm. The Mu motion and laser ionization model was constructed and simulated via the customized Monte Carlo program. This idea offers hope of reaching the statistical sensitivity of 0.1 ppm for a_μ.

Table 1.5 summarizes the issues, the projects proposed to revolve the issues, and the corresponding chapters in this thesis. The thesis introduces the experimental setup of the Mu ionization experiment in Chapter 2, the simulation study in Chapter 3) and the hardware preparation on the slow muon beam-line in Chapter 4. Experimental data taking and analysis are described in Chapter 5. A novel Mu target design idea is introduced in Chapter 6.

表 1.5　热缪子源开发中的两个关键问题总结与本论文的组织结构

Table 1.5　Summary of current issues on the thermal muon source development and the structure of the thesis

Current issues	Projects to resolve the issues	Corresponding chapters
(1) Prototype validation of thermal muon generation scheme: • Generation efficiency • Propeties of thermal muon	Mu laser ionization project (Phase-0 of Mu 1S-2S spectroscopy)	• Simulation (Chapter 3) • Hardware preparations (Chapter 4) • Experiment results (Chapter 5)
(2) Towards higher thermal muon intensity for long-term goal	Novel design of multi-layer targets project	• Chapter 6

2 Experimental Setups for Mu Ionization Experiment

This chapter describes the experimental setups for the Mu ionization experiment, including the overview of the setups, the upstream surface muon beam from J-PARC facilities, the silica aerogel samples, the 244 nm laser development, and the slow muon beam-line (SMBL).

2.1 Setup overview

Figure 2.1 shows the schematic drawing on the overview of the Mu ionization experiment.

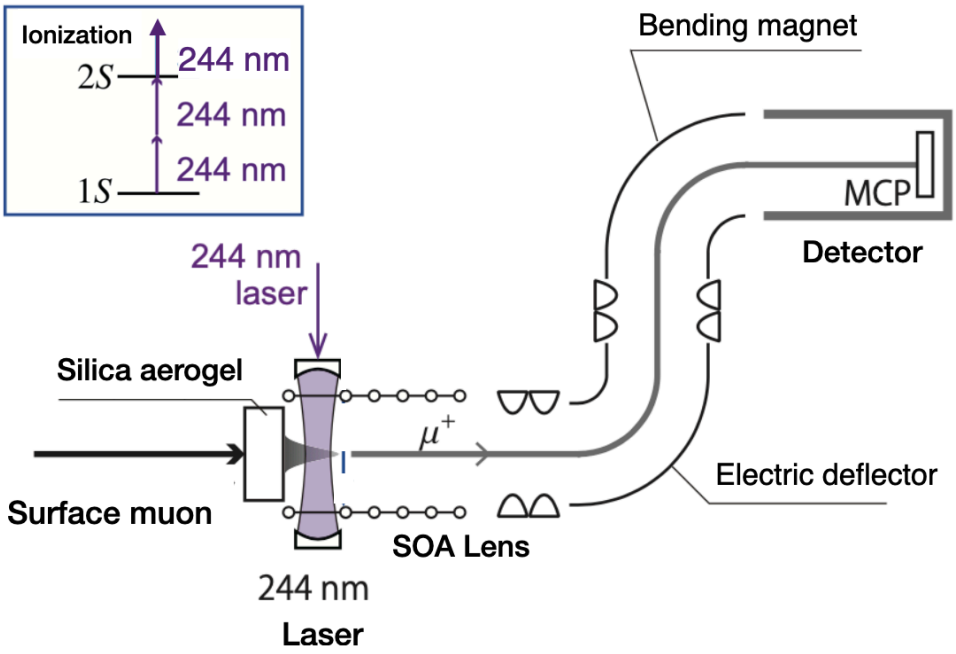

图 2.1　缪子素激光电离实验配置概览

Figure 2.1　Overview on the Mu ionization experimental setups

The incident surface muon beam from J-PARC MLF with the momentum of 28 MeV/c is transported to the experimental area. Muon beams first pass through the SUS foil window, separating the muon beam-line vacuum and the downstream vacuum (slow muon beam-line). A large portion of the surface muons stopped inside the silica aerogel target, where the surface muon captures an electron and forms thermal Mu. Mu has the diffusion process in the target. Only part of Mu emits into the vacuum after the downstream aerogel surface. The 244 nm

laser is timed to excite the Mu from 1S to 2S state via two-photon excitation; the third 244 nm photon helps strip out an electron and ionize Mu. The thermal muons are generated.

After thermal muon generation, the meshes between the downstream surface of aerogel and the first lens of the SOA provide the extraction E-field. SOA lens accelerates muon from thermal energy (0.02 eV) to 20 keV. Muons are transported in the slow muon beam-line (SMBL), where there are quadrupoles for the beam focusing, electric bending and magnetic bending for eliminating the backgrounds. Finally, muon reaches the multi-channel plate (MCP) detector, where hit rate (by single-anode MCP) and profile (by beam-profile monitor, MBPM) are measured.

2.2 Muon beam at J-PARC MLF

Figure 2.2 shows the overview of the J-PARC facilities. The protons accelerated by the J-PARC linear accelerator (LINAC) are transported into the 3-GeV rapid cycling synchrotron (RCS). Part of the 3 GeV proton beam is transported to the Materials and Life Science Experimental Facility (MLF) by the 3 GeV nucleon beam transport beam-line (3NBT) at 25 Hz.

There are muon targets and neutron targets inside the MLF. The muon target is made of graphite facing upstream to the proton beam. When the proton hits the muon target, about 5% of the total energy is consumed on the muon target. Charged pion, π^+, and π^- are produced by

$$p + N \rightarrow \pi^{\pm} + N \tag{2.1}$$

Pions soon decay into muons through:

$$\pi^+ \rightarrow \mu^+ + \nu_\mu \tag{2.2}$$

$$\pi^- \rightarrow \mu^- + \bar{\nu}_\mu \tag{2.3}$$

Those muons produced via the pion decay in flight in the lab frame are called “decay muons”. Other muons come from the pion that decays on the surface of the target and is known as “surface muon”. Surface muons have a momentum of 28 MeV/c. Since the negative muons stopped in the target are trapped in atoms, the yield of the negative muons is much less than the positive ones. We refer to the surface muon to be positive in this thesis. The proton beam power at MLF is approximately 780 kW as of March 2022. J-PARC has a plan to upgrade the power up to 1 MW.

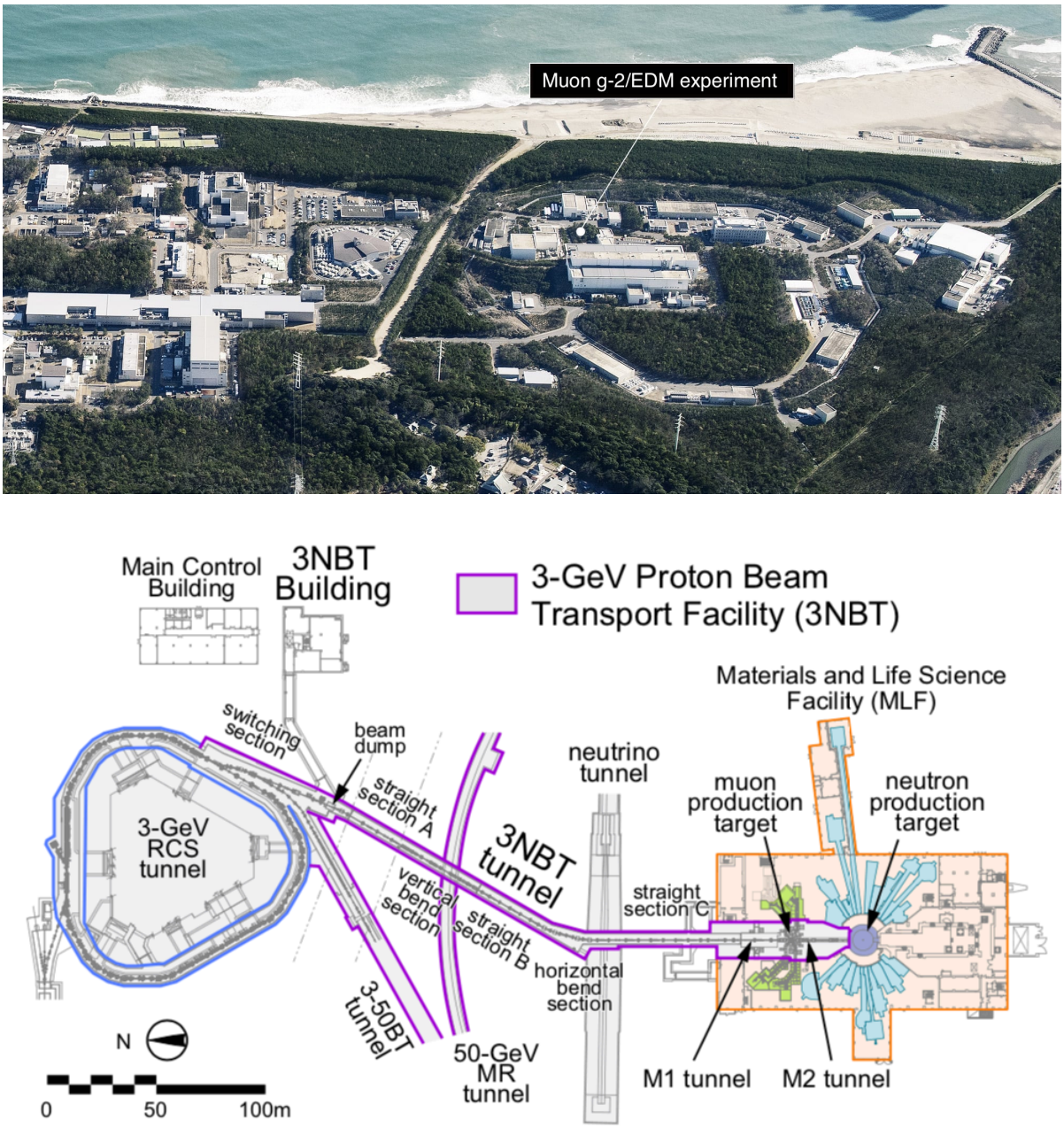

图 2.2　上：J-PARC 鸟瞰图；下：J-PARC 质子加速器设备概览，包括 RCS 环形加速器和物质、生命科学研究设施（MLF）。E34 实验和本文中的缪子素激光电离实验在 MLF 建设。

Figure 2.2　Top: J-PARC birdview. Bottom: overview on J-PARC facilities (RCS on the left and MLF on the right). E34 experiment and Mu ionization experiment in this thesis are proposed at MLF.

Figure 2.3 shows the schematic drawing of the muon beam-lines at MLF. There are in total four muon beam-lines extended from the muon target: S-line ('slow muon'), H-line ('high-intensity muon'), U-line ('ultra-slow muon'), and D-line ('decay muon').

Along each beam-line, there are sub-experimental areas divided at the end. Details on S-line and H-line are shown in Figure 2.4. The E34 experiment is expected to be installed in the H2 area. In contrast, the Mu ionization experiment and the future phases of the Mu 1S-2S spectroscopy experiment utilizes the S2 area, where the SMBL was installed. The S-line consists of three bending magnets and several quadruples to provide muon beam bending and focusing. The S1 and S2 areas share the S-line common parts before the third bending magnet (known as "SB3"). The slits (SSL1) were set between the second magnet (SB2) and the triplets (SQ10-12). After SB3, there sets a kicker to separate the muon beam between S1 and S2. The muon beam from MLF is a two-bunched structure. The Mu ionization experiment at S2 receives first one of two bunches at 25 Hz.

An automatic beam tuning program named " ForTune"[50], developed at MUSE, was used to obtain a well-focused muon beam. The surface muon intensity at S1 was currently measured with the slit and the collimator. The surface muon intensity at S1 was measured to be about $1.9 \times 10^5/s$ for 500 kW proton power and the single pulse.

2.3 Silica aerogel and target holder

The techniques of the laser-ablated aerogel has been introduced in Chapter 1. In addition, further progress on the aerogel material has been made for the Mu ionization experiment: by applying laser ablation on both surfaces, the wrapping of the aerogel target, which appeared in the previous models, has been fixed. The photos of new samples are shown in Figure 2.5, whose shape has been significantly improved compared with the previous ones in Figure 1.11.

The aerogel samples were initially fabricated at Chiba University. Then the samples were transported to the University of British Columbia (UBS) in Canada for the laser-ablation on their surfaces.

2.4 244 nm laser system

The group has developed the 244 nm laser system at Research Institute for Interdisciplinary Science (RIIS) from Okayama University, Japan.

The scheme for the pulse 244 nm laser production for phase-0 is shown in Figure 2.6. The high stabilized 976 nm CW seed laser will be used and be amplified in several stages,

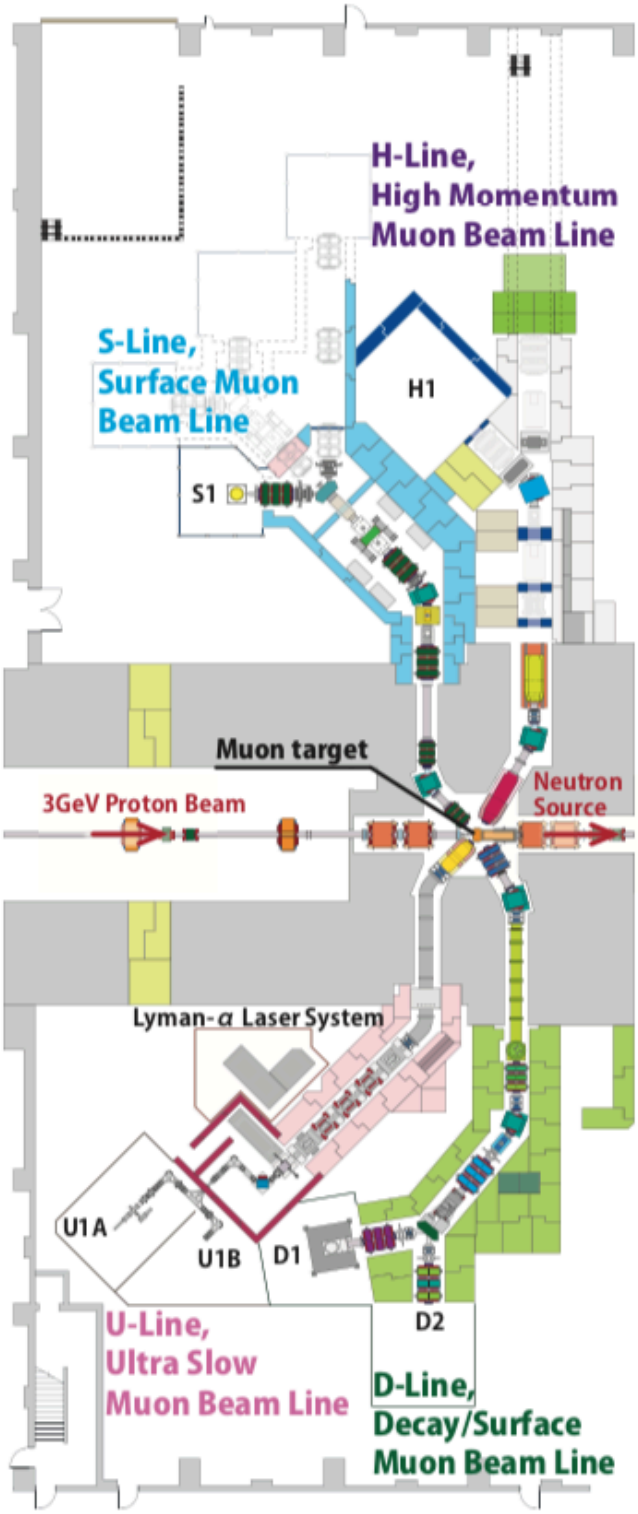

图 2.3　MLF 缪子束线概览，包括 S-line, H-line, U-line 和 D-line 四条束线。

Figure 2.3　Overview on MLF muon beam-line (including S-line, H-line, U-line and D-line)

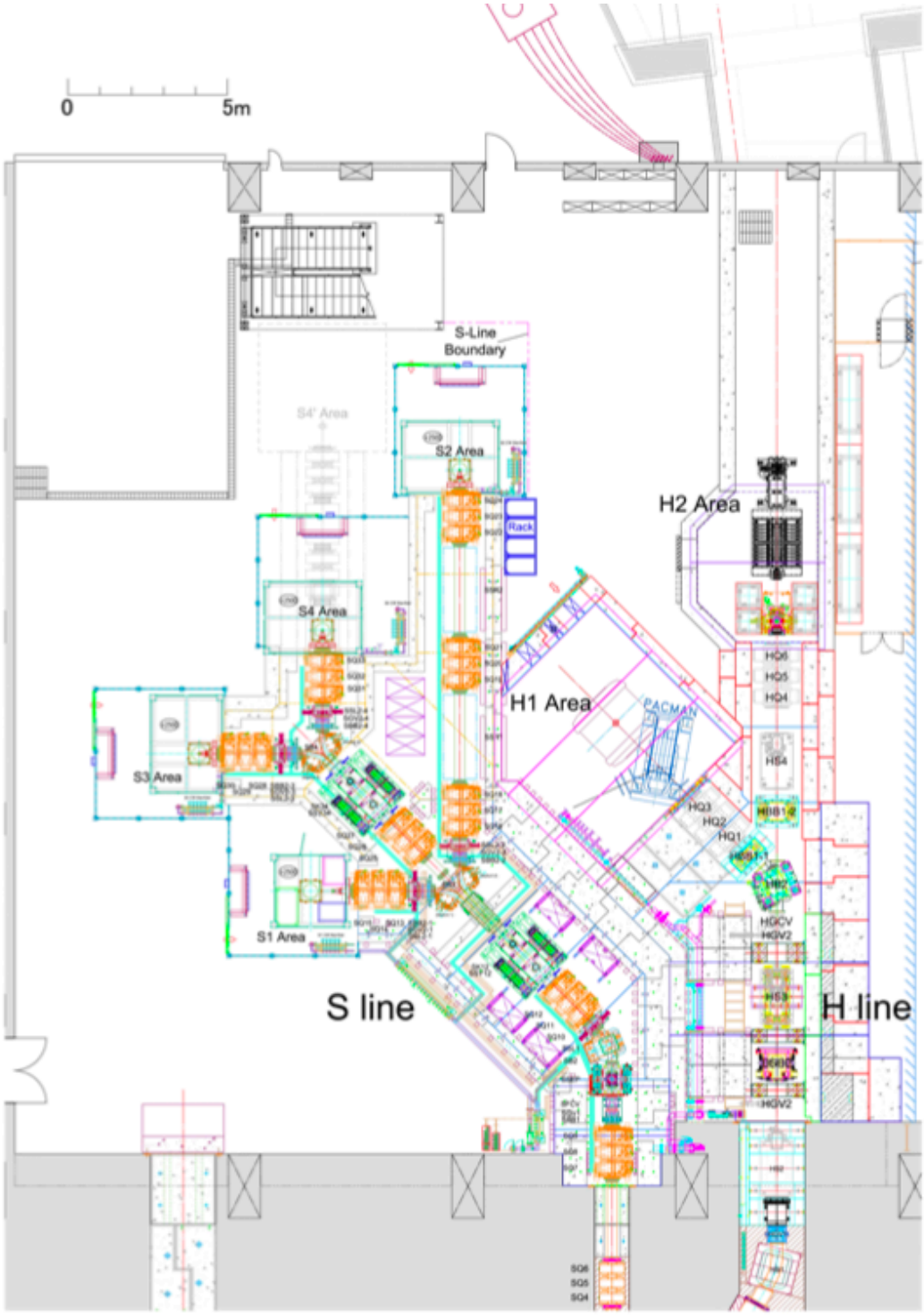

图 2.4　S-line 束线图。缪子激光电离实验安装在 S2 区域。缪子反常磁矩（E34）实验未来将在 H2 区域建造。

Figure 2.4　S-line overview: the Mu laser ionization experiment was installed at S2 area while the E34 experiment will be at H2 area.

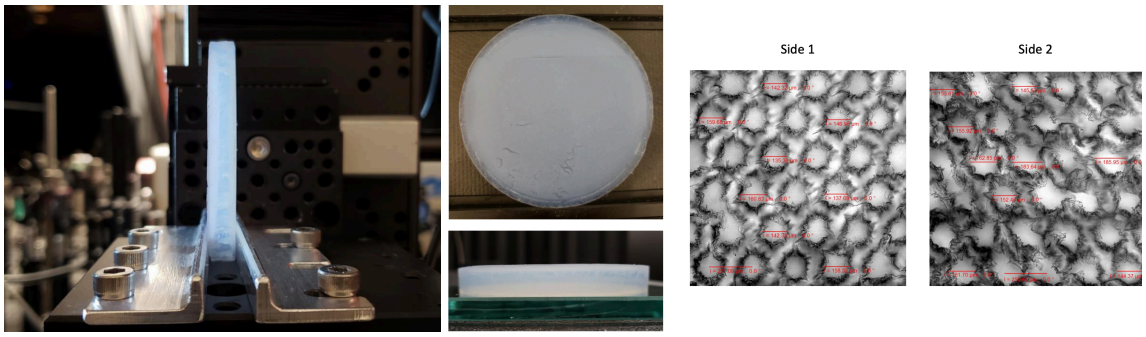

图 2.5 左图：双表面激光蚀刻的硅凝胶样品，和旧样品（图 1.11）相比，本样品不再变形，更加稳定。右图：硅凝胶表面被蚀刻后的空洞结构的细节。

Figure 2.5 Left: Silica aerogel samples with double layers laser-ablated. No wrapping could be seen compared from old one in Figure 1.11. Right: Detailed photos of the laser-ablated holes on the surface of aerogel.

including the Ti:S cavity and Ti:S amplifier. After the Second Harmonic Generation (SHG) with lithium triborate (LBO) crystal and Fourth Harmonic Generation (FHG) with β-barium borate (BBO) crystal, the 244 nm laser is produced. The expected power of the 244 nm laser for the Mu ionization experiment ranges from about 1 mJ to 5 mJ.

In the future phases for the Mu 1S-2S spectroscopy experiment, CW 244 nm laser is considered, and the more complex schematic drawing is shown at the bottom of Figure 2.6. The CW laser narrows the linewidth[51], and the low intensity is compensated with an enhanced optical cavity.

2.5 Slow muon beam-line (SMBL)

2.5.1 Accelerator components

The slow muon beam-line (SMBL) consists of several accelerator components[52]. At the most upstream is the SOA lens, which provides the static electric field for the initial extraction nad acceleration of thermal muon. SOA consists of four lenses labeled S1, S2, S3, and S4. The S1 is mesh, which provides the initial electric field with the target mesh. The specifications of the SOA are summarized in Table 2.1. The size of the SOA is shown in Figure 2.8.

After SOA, The electric quadruples labeled EQ1 and EQ2 were installed to focus the muon beam, as well as EQ3 and EQ4 towards the detector. The electric deflector (ED) and bending magnet (BM) select the muon's kinetic energy and momentum. The background of decay positrons from the incident muons and the electron produced by the field emission are eliminated[53]. The specifications of ED, EQs and BM are summarized in Table 2.1, 2.2, 2.3, 2.4

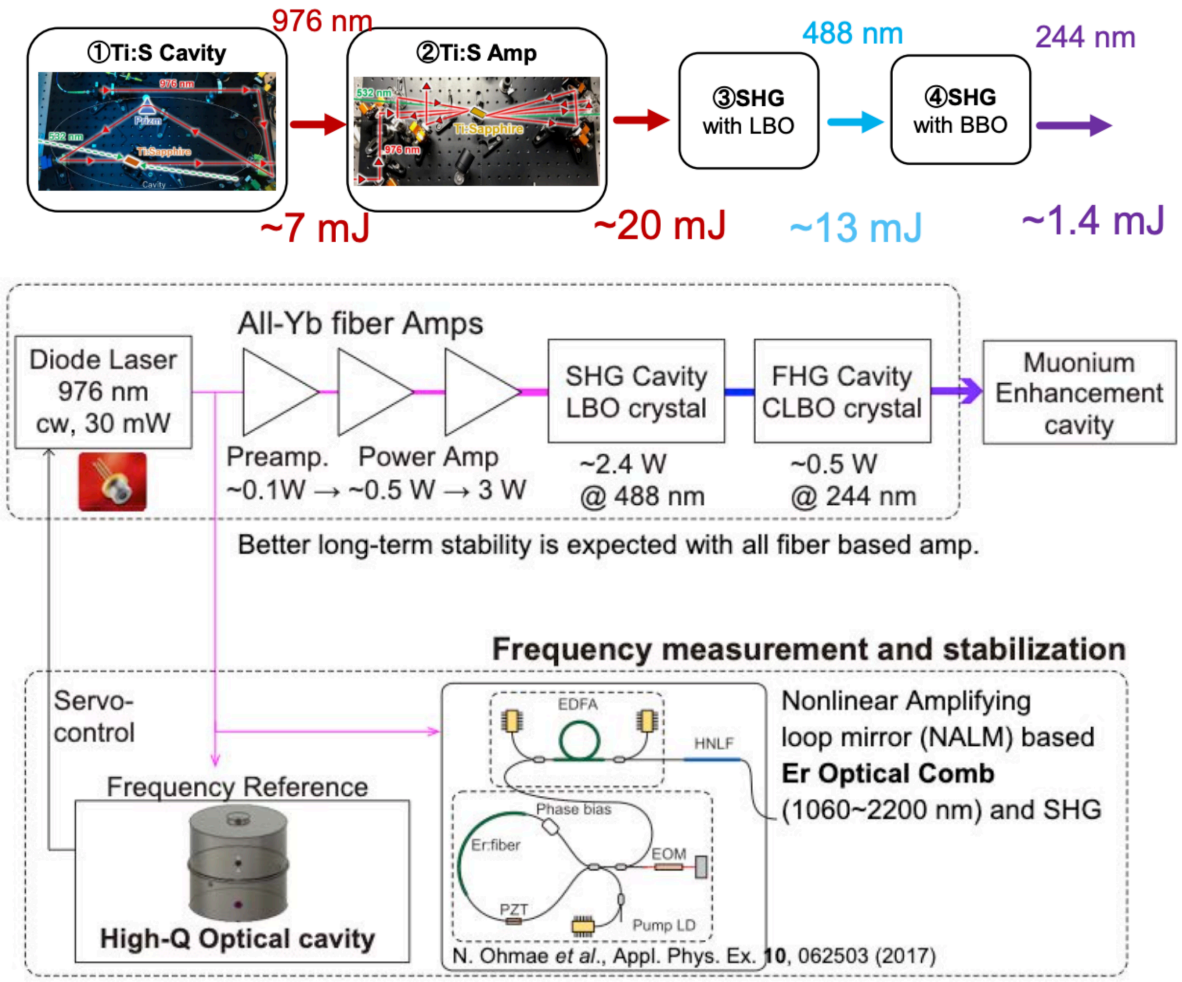

图 2.6　244 纳米波长的激光的开发示意图。上图为缪子素激光电离实验初级阶段采用的脉冲激光。能量较低（约 1-2 mJ 左右）。下图为长期实验计划采用的激光方案。由 976 纳米的种光经过光纤放大后再经过二次变频得到 244 纳米波长的激光。

Figure 2.6　244 nm laser development. Top: the pulsed 244 nm laser utilized in the Phase-0 of Mu ionization experiment. Bottom: the developement of CW 244 nm laser for future phases.

and 2.5.

The re-configuration of the SMBL was conducted during the spring of 2020. After re-configuration, the bending direction of the beam-line was changed, with better beam-line alignment achieved. Current SMBL at the S2 area is shown in Figure 2.7. The details of the SMBL re-configuration work are described in Chapter 4.

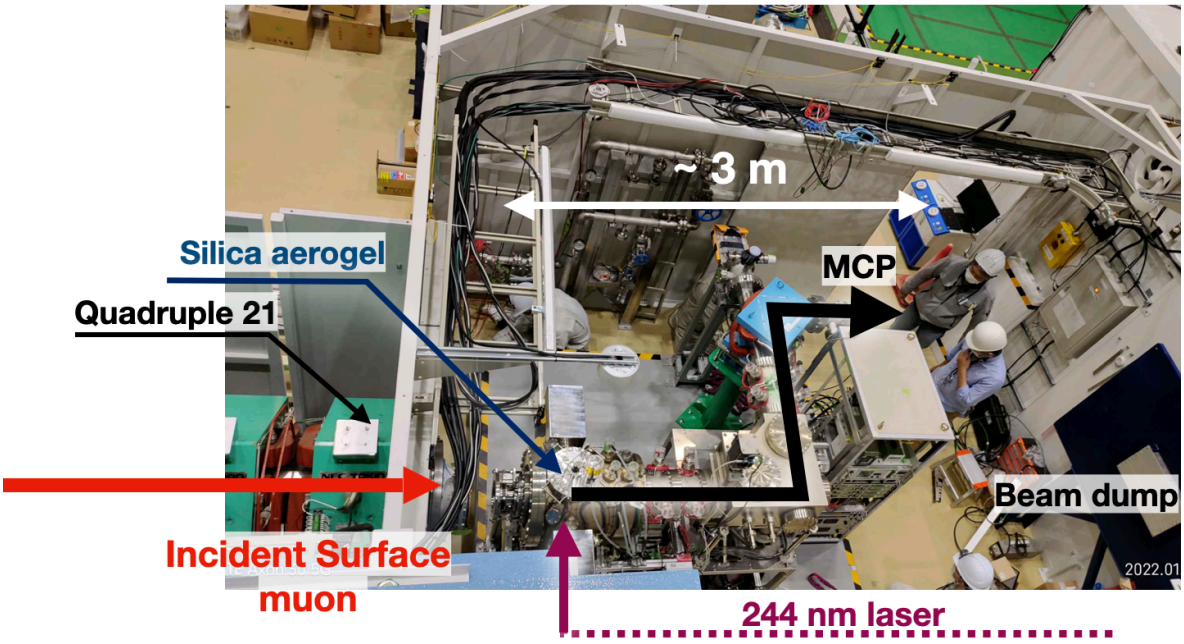

图 2.7 经过重新组装后的 SMBL 概览（已被安装在 S2 区域）。左侧为加速器上流方向。

Figure 2.7 The overview of the SMBL after re-configuration (at S2 area). The upstream of the beam-line (SOA chamebr) is on the left.

表 2.1 SOA 规格表

Table 2.1 Specifications of SOA

SOA Electrode	SOA-S1	SOA-S2	SOA-S3	SOA-S4
Typical applied voltage [kV]	+18.94	+18.04	+16.00	0.00
Length of the electrode [mm]	2	38	196	2
Inner aperture [mm]	80	76	140	76
Outer aperture [mm]	174	174	148	174

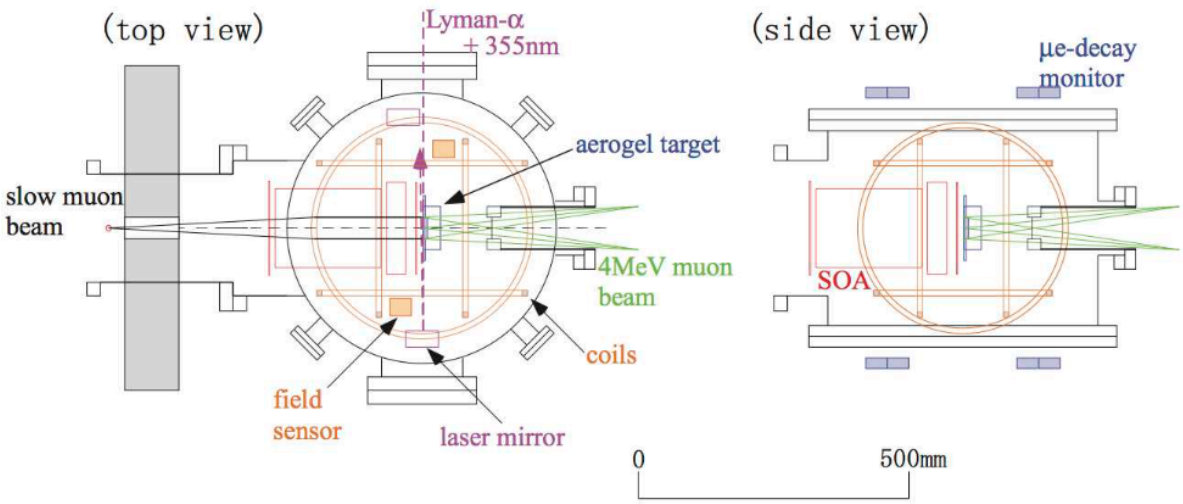

图 2.8　电极板加速装置（SOA）配置图

Figure 2.8　SOA design drawing

表 2.2　靶金属网格和 S1 金属网格规格表

Table 2.2　Specifications of the target mesh and S1 mesh.

Meshes	target mesh	S1 mesh
Typical applied voltage [kV]	+20.00	+18.94
Thickness [mm]	0.1	0.1
Aperture [mm]	78	80
Meterial	W	Mo
Openning fraction [%]	77.8%	84.9%

表 2.3　电偏转极板（ED）规格表

Table 2.3　Specifications of electric deflector (ED)

ED	
Deflection angle [degree]	90
Curvature radius [mm]	400
Maximum withstand Voltage [kV]	2.5
Electrode aperture [mm]	100

表 2.4 偏转磁铁（BM）规格表

Table 2.4 Specifications of bending magnet (BM)

BM	
Maximum Current [A]	20
Typical Voltage [V]	5
Magnetic field [Gauss]	300
Weight [kg]	370

表 2.5 电四极铁（EQ）规格表

Table 2.5 Specifications of electrid quadruples (EQ)

EQ	
Typical voltage [kV]	1.0
Length of the electrode [mm]	80
Electrode aperture [mm]	80

2.5.2 Vacuum system

Figure 2.9 shows the vacuum system on the SMBL. Two scroll pumps (SPs) and two turbomolecular pumps (TMPs) are connected at the MC and ED bottom to provide the vacuum environment. There are two vacuum pumping lines at the MC (TMP1-SP1) and ED (TMP2-SP2). A gate valve (EQ2-GV) is set in between two pumping positions. There are also gate valves at the main chamber (V1 and V2) and the ED (ED-GV).

The vacuum level is monitored with several vacuum gauges at the MC and detector chamber. The requirement from the MCP detector is to maintain the vacuum level with less than 1.3×10^{-4}Pa.

2.5.3 High voltage system

The High Voltage modules for SOA, EQ, ED, and BM's current module are remotely controlled with the EPICS (Experimental Physics and Industrial Control System)[55] through the PLC (Programmable Logic Controller) modules. EPICS is an open software framework to create a remote control system for the power supplies and monitor the voltage or current from the beam-line apparatus. Physical IOC (I/O controller) is its central task. In SMBL, PLC is integrated via TCP/IP to EPICS. Figure 2.10 shows the block diagram of the remote control system. Figure 2.11 exhibits the various HV modules on the rack nearby SMBL at MLF S2.

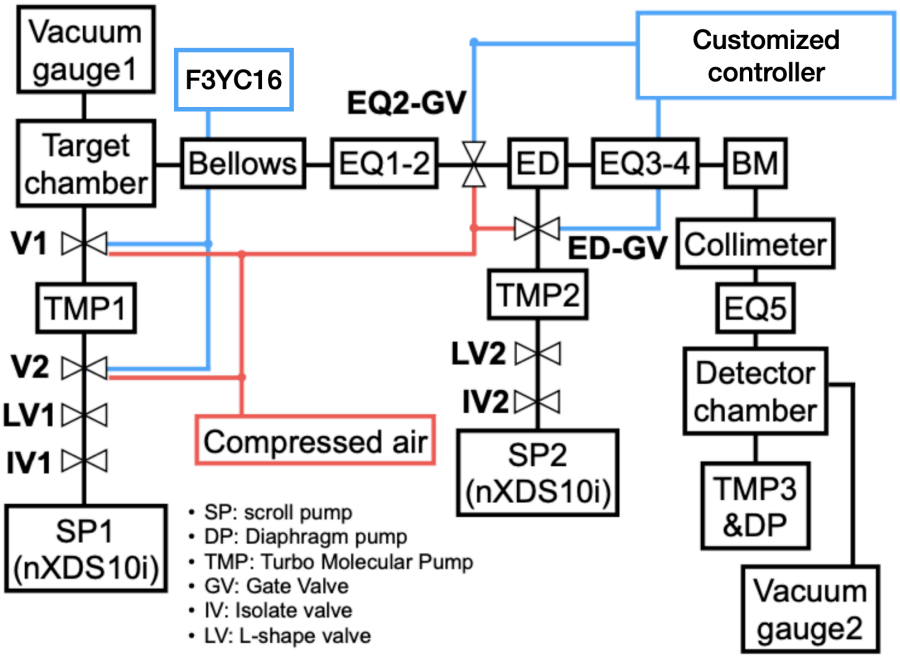

图 2.9　SMBL 真空系统图

Figure 2.9　Block diagram of SMBL vacuum system, updated from[54].

Figure 2.12 displays the different PLC modules on the shelf labeled with their functions.

2.5.4　Multi-channel plate (MCP) detector

The multi-channel plate (MCP) detects the thermal muon rate. It has excellent sensitivity to detections with low energy particles. Figure 2.13 shows the photo of the MCP. The MCP in our SMBL is a single-anode type fabricated by Hamamatsu with a fast response.

When the muon hits one of the channels of the MCP, secondary electrons are generated and accelerated by the applied voltage. Electrons hit the opposite side of the wall, and their showers will be multiplied. This amplification process in the MCP produces the observable electric signal.

The detection efficiency of the MCP depends on the open aperture ratio of the channel on the surface of the MCP. The open aperture ratio of our MCP is 95%.

2.5.5　The Muon Beam Profile Monitor (MPBM)

The muon beam profile monitor (MBPM) for the low-energy muon was developed based on the MCP, a phosphor screen, and a CCD camera. When the incident particles hit the MCP

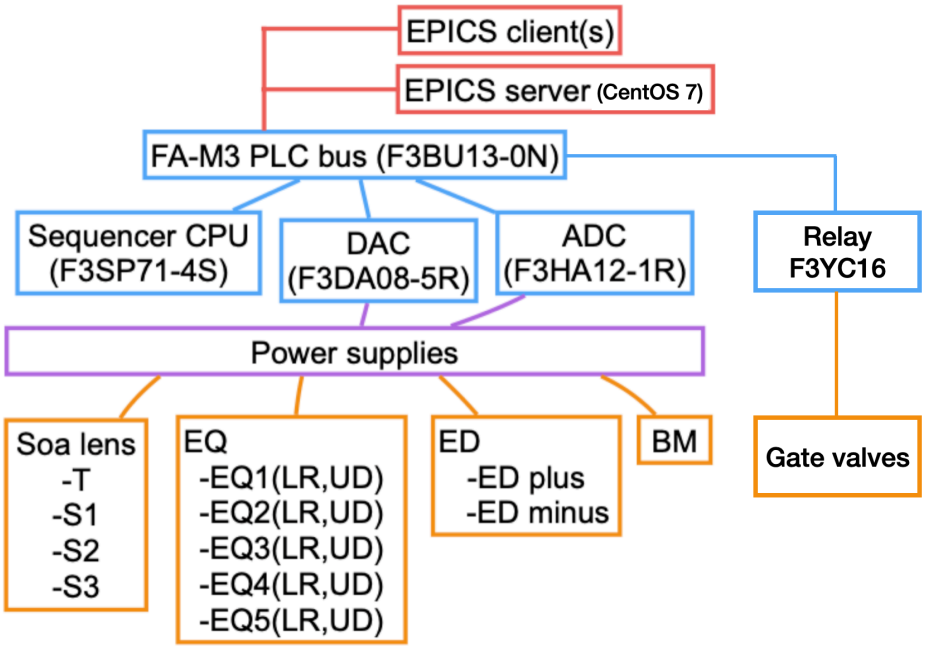

图 2.10 EPICS 远程控制高压系统框图

Figure 2.10 Block diagram of EPICS system for high voltages, updated from[54].

and produce secondary electrons, those electrons will be extracted by the potential gradient between the MCP and the phosphor screen, where electrons strike. The phosphor screen converts the output secondary electrons into photons. The photon distribution is transported to the CCD camera through the optical lens. The photo image of the beam profile is projected to the CCD sensor and detected[56]. Figure 2.14 shows the schematic of the BPM with the CCD camera.

2.5.6 Optical fiber and Al target

During the hardware preparations of the SMBL, the H^+ particle was used at KEK before muon beams were available at J-PARC. Figure 2.15 shows the setup for H^+ generation. It consists of an optical fiber that induces the light emitted from the Xe lamp into the Al plate. The photon from the lamp hits the Al target and H^+ is generated. SMBL transported the H^+ to the MCP detector with proper HV applications. Such source is free of laser ionization. It was used for testing the SMBL after the re-configuration and for alignment of the signal.

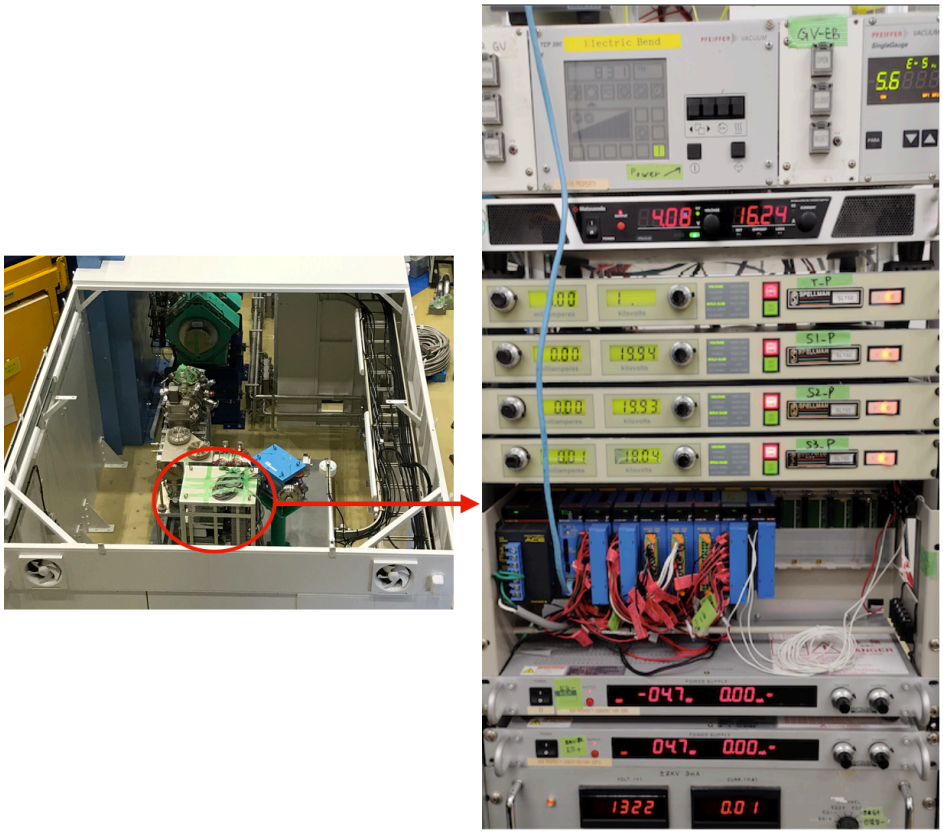

图 2.11　S2 区域的各高压组件实物图

Figure 2.11　Photo of the HV modules on the rack at MLF S2

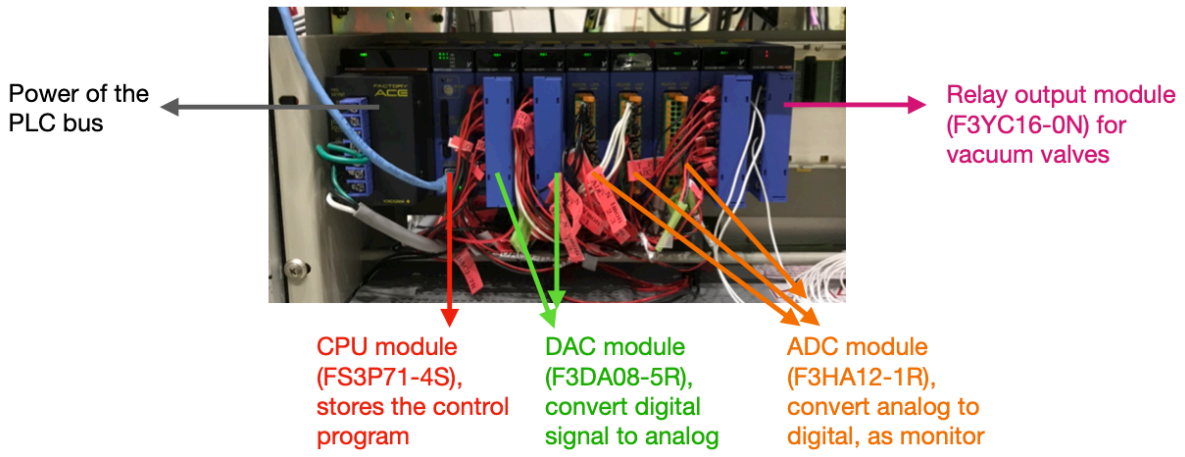

图 2.12　可编程逻辑控制组件（PLC）实物图。不同型号的组件可实现不同的电压、电流和真空阀门控制功能。

Figure 2.12　Photo of the PLC modules on the rack at MLF S2. There are various types for different functions on HV and vacuum systems.

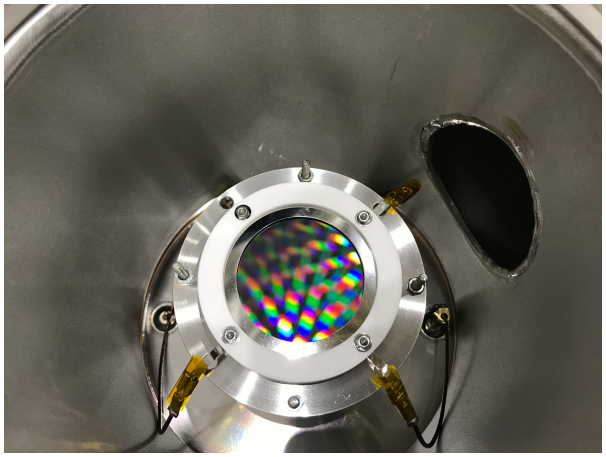

图 2.13　微通道板探测器（MCP）实物图。探测区域的直径约为 40 毫米。

Figure 2.13　MCP detector with a diameter of 40 mm.

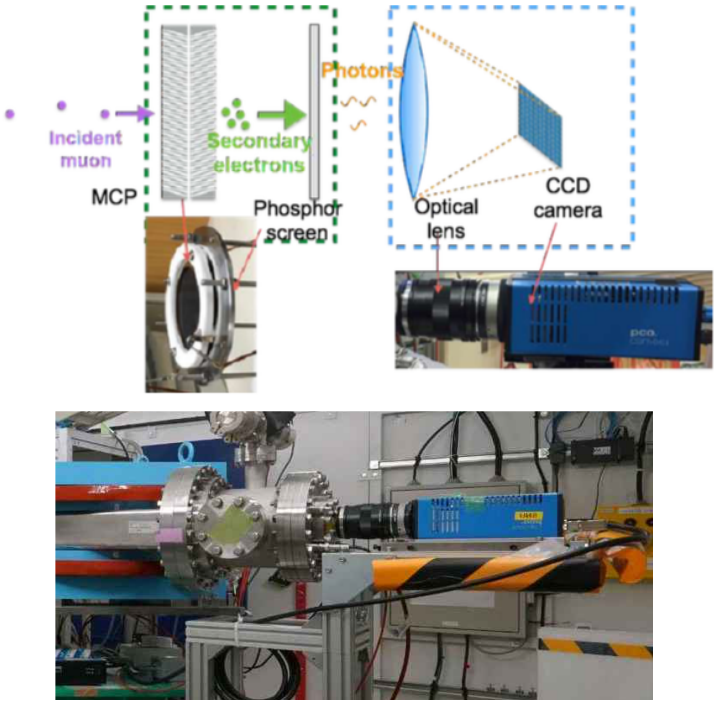

图 2.14　上：缪子束流轮廓探测器示意图；下：CCD 照相机设置实物图[54]

Figure 2.14　Schematic drawing of the MBMP (top) and the installation of the CCD camera (bottom). From Reference[54].

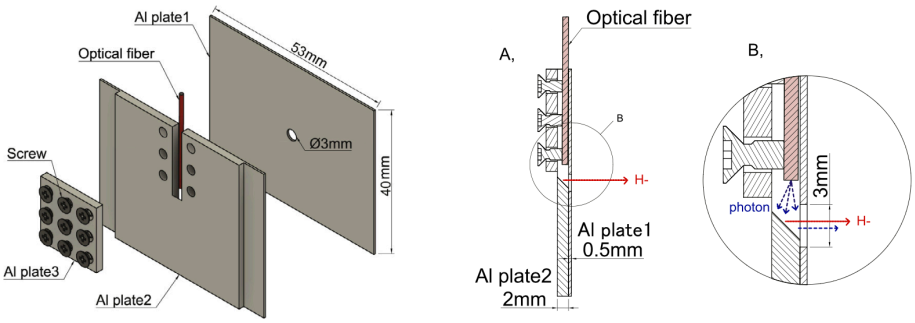

图 2.15　光纤与铝板产生 H 源示意图[56].

Figure 2.15　Fiber with Al target to generate H source. From Reference[56].

3 Simulation Study for Mu Ionization Experiment

This chapter describes the end-to-end simulation to estimate the thermal muon intensity for the Mu ionization experiment. From upstream to downstream, it includes the surface muon transport through S-line to the S2 area, the Mu formation and diffusion inside the aerogel, Mu yield into the vacuum, and the extraction of the thermal muon by slow muon beam-line (SMBL). Finally, the thermal muon generation efficiency and signal rate at detector are estimated.

3.1 Surface muon Transport

The simulation goal in this section is to estimate the surface muon intensity at S2 entrance and obtain a focusing beam profile with optimized beam-line optics.

The simulation was performed using the Geant-4-based software, the G4beamline[57]. Since the S2 area is the newly constructed experimental area for our project, the strategy is to start from the surface muon intensity measured at the S1 area and then simulate similar conditions in the S2 area with the unnecessary slits and collimator removed. The efficiency from the simulation result was used to estimate the transport efficiency and calibrate the surface muon rate intensity at the S2 area. The strategy flow is shown in Figure 3.1.

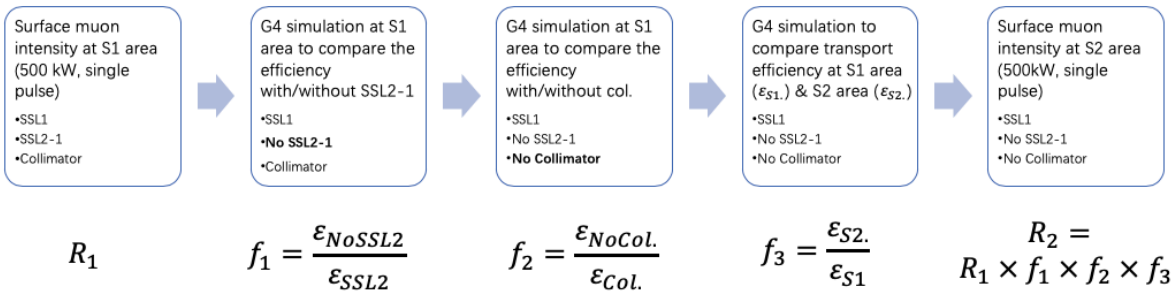

图 3.1 估计在 S2 区域表面缪子束流亮度（R_2）的策略。从 S1 测量的计数率出发，狭缝（SSL2-1）和准直器（collimator）被一步步移除，并得出相应的变化率。

Figure 3.1 Strategy to estimate the surface muon intensity R_2 at S2. Slit SSL2-1 and the collimator were removed at S1 simulation step by step to check the change of the efficiency

In the G4Beamline (G4BL), the accelerator components to the S2 area were created. As

shown in Figure 3.2, the beam-line consists of bending magnets (SB1, SB2, SB3), magnetic quadruples (SQ1 to SQ21), a DC separator (SSEP), etc. After Septum (SB3), S-line divides into the different experimental areas. Quadrupole triplets SQ16-18 and SQ19-21 are set towards to S2 area. Three quadruples make a triplet set for the beam focusing.

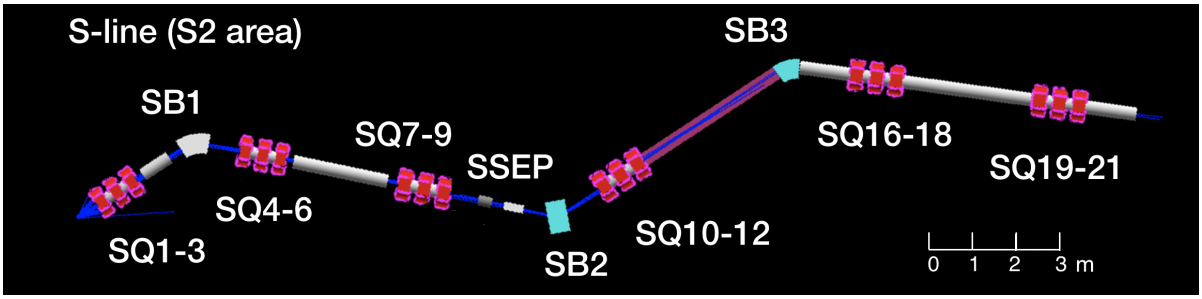

图 3.2 S 束线模拟的光束线光学设计，从左到右为上流到下游方向。其中蓝色数据点显示表面缪子光束从左到右的典型传输。

Figure 3.2 The beam-line optics design for the S-line simulation, where blue lines shows the typical transport of the surface muon beam from left to right.

The initial surface muon beam profile before the S-line transport was assumed to be a Gaussian distribution. Parameters are summarized in Table 3.1.

表 3.1 表面缪子束流的初始分布模拟参数

Table 3.1 Initial surface muon distributions

Parameter	Value
Mean momentum P	28.5 MeV/c
σ_P	0.5 MeV/c
σ_x	17 mm
σ_y	24 mm
$\sigma_{X'}$	0.208 mm
$\sigma_{Y'}$	0.208 mm

Surface muon intensity was measured to be 1.9×10^5 at S1 at 500 kW proton power under the single bunch with slits SSL1 and SSL2-1 set. Conditions were changed step by step to investigte the final efficiency and the intensity accordingly, as shown in Table 3.2.

From Table 3.2, The effects of the conditions change in S1 are summarized:

- The effect of removing SSL2-1 is:

$$f_1 = \frac{\epsilon_{NoSSL2-1}}{\epsilon_{SSL2-1}} = 4948/575 = 9.1$$

表 3.2 S1 束线在各种狭缝与准直器条件下的模拟总结

Table 3.2 Summary of the S-line simulation under various conditions

SSL1 [mm × mm]	SSL2-1 [mm × mm]	Collimator	$N_{initial}$	N_{final}	Efficiency	Scaled intensity (500 kW, single pulse) [/s]
100×40	40×40	ON	1E+06	574	0.00057	1.9×10^5
100×40	40×40	OFF	1E+06	586	0.00059	1.9×10^6
100×40	240×240	OFF	1E+06	7236	0.0072	2.4×10^6
240×240	240×240	OFF	1E+06	10646	0.011	3.5×10^6
100×40	240×240	ON	1E+06	4948	0.0050	1.6×10^6
240×240	240×240	ON	1E+06	6931	0.0069	2.3×10^6

- The effect of removing collimator is:

$$f_2 = \frac{\epsilon_{NoCol.}}{\epsilon_{Col.}} = 7236/4948 = 1.5$$

In the S2 simulation, the currents of last triplet (SQ19, SQ20, and SQ21) were tuned to have optimized beam size and the profile at the muon stopping target at S2, while the other triplets' settings before SQ16 are the same in the S1 area. The focusing position of the beam is changed when triplet currents are changed. SQ19 and SQ21 are for beam focusing in vertical (Y) direction, while SQ20 is for the horizontal (X) direction. The beam size is shifted by scaling all the three current setups. It was difficult to focus both horizontal and vertical directions simultaneously. As a balance, the profile at the end of the beam-line was explicitly tuned to be shrunk vertically but extended horizontally, considering horizontal laser-shooting conditions. More events are expected to penetrate the laser ionization area after surface muons' stopping and Mu emission. The best results are summarized in Table 3.3.

表 3.3 S2 区域内四极铁组合（SQB19-21）调试参数总结

Table 3.3 Summary of the S2 SQB19-21 tuning

SQB	Normalized current [A]
19	0.29
20	-0.43
21	0.19

The simulation result on S2 slits is shown in Table 3.4. As S1 and S2 share the same slit SSL1, the setup for the Mu 1S-2S experiment at S2 is determined such that SSL1 is set to be 100×40 mm^2 while SSL2-2 240×240 mm^2, without the collimator in the end.

表 3.4　S2 束线在狭缝与准直器条件下的模拟总结

Table 3.4　Summary of the S-line (S2) simulation

SSL1 [mm × mm]	SSL2-2 [mm × mm]	Collimator	$N_{initial}$	N_{final}	Efficiency
100×40	240×240	OFF	2.1E+09	$1.505\,707\,3 \times 10^7$	0.00717
240×240	240×240	OFF	1E+08	$1.085\,249 \times 10^6$	0.0109

The optimized beam at the target position has a Gaussian shape with a size of approximately 77 mm (FWHM) horizontally and 29 mm vertically. Based on the simulation and the comparison with the measurement at S1, the surface muon intensity at the S2 area is estimated to be 2.4×10^5/s per pulse at 500 kW without the slit and the collimator at S2.

From Table 3.2 and Table 3.4, under the same specifications (SSL1 100*40 mm^2, SSL2 240*240 mm^2, collimator OFF), the efficiency of beam line transport for S2 and S1 was compared. The transport efficiency for S-line to S1 area is 0.00724 while S2 is 0.00717. The final scale factor is calculated as:

$$f_3 = \frac{\epsilon_{S2}}{\epsilon_{S1}} = 0.00717/0.00724 = 0.99$$

It implies that the transport efficiency for S1 and S2 are almost the same. The intensity of the surface muon beam at the S2 area is therefore estimated to be

$$R1 \times f_1 \times f_2 \times f_3 = 1.9 \times 10^5/\mathrm{s} \times 9.1 \times 1.5 \times 0.99 = 2.4 \times 10^6/\mathrm{s}$$

under 500 kW proton power and single bunch.

The profile at the end of S2 is shown in Figure 3.3, including the distributions in the X and Y directions, X-X', Y-Y' distributions, and the momentum distributions. The asymmetry exhibited in X and Y directions was from the upstream setups of quadruples to maximize the downstream Mu number for horizontal laser shooting. The beam envelope along the S-line to S2 is shown in Figure 3.4, corresponding to the critical accelerating components from Figure 3.2. Simulation results are summarized in Table 3.5. The profiles is used as input for the further simulations of surface muon stopping inside the aerogel target and the Mu yield for the laser ionization.

We are particularly interested in the region near the aerogel target. Figure 3.5 shows the beam size near the target region. Beam size focuses in both horizontal and vertical directions

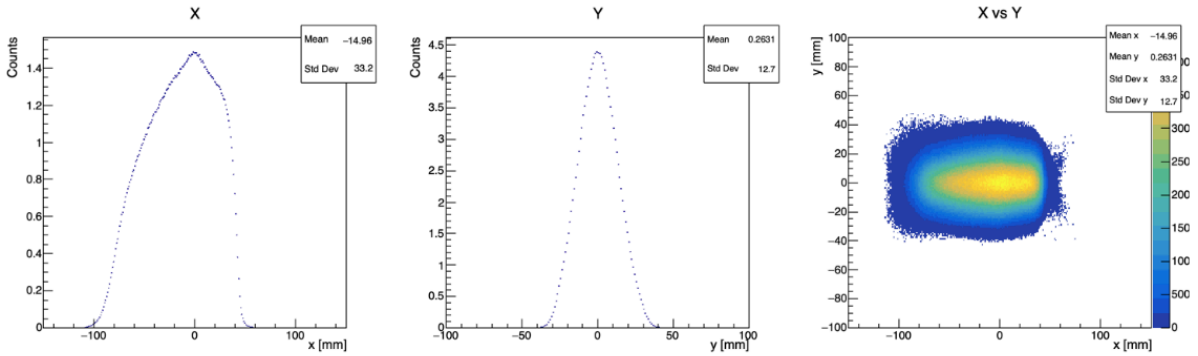

图 3.3 S2 区域传输后的最终表面缪子分布，从左到右分别为 X，Y 和二维空间分布。虚拟探测器位于硅凝胶靶位置上游 163 mm 处。

Figure 3.3 Surface muon distributions after transport at S2 area, including X,Y,spatial distributions. The virtual detector is 163 mm upstream from silica aerogel target position.

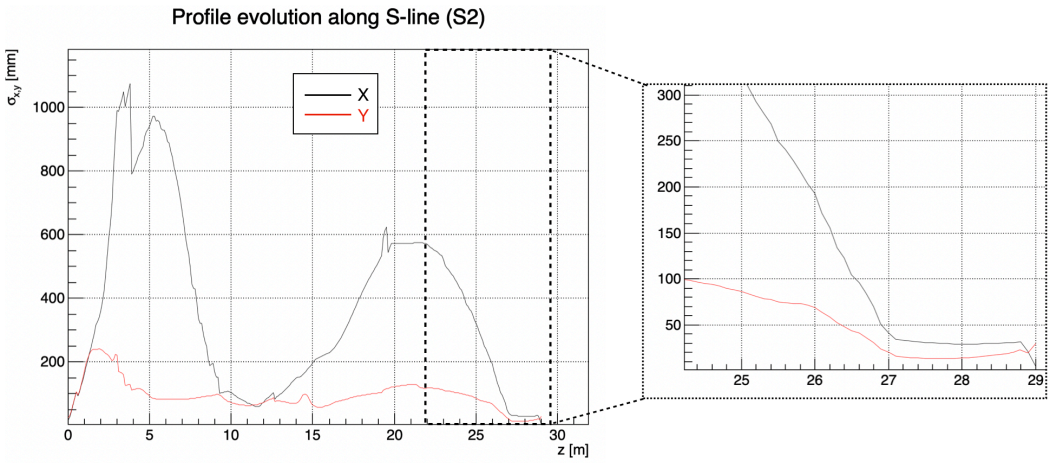

图 3.4 沿 S 线传输（至 S2 区域）的光束包络。质子靶在初始位置（0 米），S2 区域的硅凝胶靶在 27.34 米处。

Figure 3.4 Beam envelope along the S-line. The proton target is at origin, while the aerogel target at S2 area is at 27.34 m.

near the 600 mm from the end of last quadruple, SQ21. The silica aerogel target position is therefore determined to be at this position.

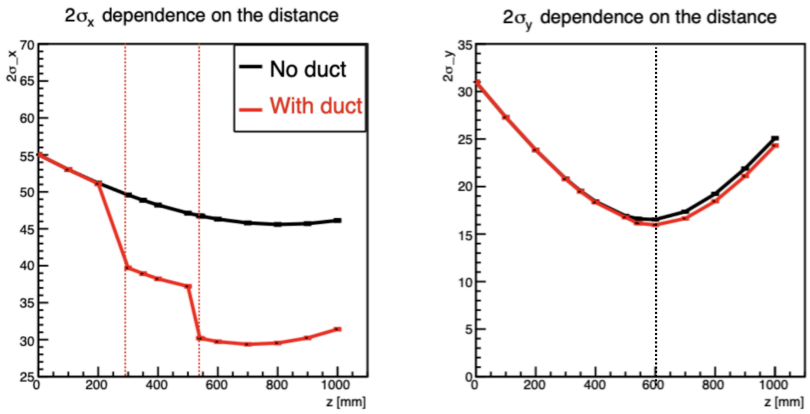

图 3.5 S2 区域附近的光束包络。根据束流的聚焦信息，可以确定最终靶的位置在距离四级铁 SQ21 的末端 600 毫米处。

Figure 3.5 Beam envelope near the target region. The red color indicates the current design of the transport duct while the black color is the result without duct (for furture improvement). The optimized focusing position (target) is determined to be 600 mm from the end of SQ21.

表 3.5 S2 表面缪子传输结果总结

Table 3.5 Summary of the S-line (S2) simulation at the S2 target position

Item	Result
Transport efficiency along S-line to S2	0.00717
Surface muon intensity at S2 (500 kW, single pulse)	2.4×10^6/s
σ_x	33.2 mm
σ_y	12.7 mm
Mean Momentum P	28.58 MeV/c
σ_P	0.46 MeV/c

3.2 Mu production

The Mu production simulation was developed to estimate the number of Mu formed in the silica aerogel target. The surface muon beam profile, the beam gradient, and the momentum distributions at the S2 area entrance obtained from Section 3.1 were used as inputs.

The GEANT4 simulation[58] was performed to obtain the fraction of the surface muon beam stopping in the target. The incident surface muons firstly penetrate a Kapton foil window

with a thickness of 100 μm and then aerogel target with Al degrader on the center of the chamber. The thickness of the Al degrader remains free for optimization. The size of the aerogel target is 78 mm × 78 mm × 6 mm in the transverse directions and the longitudinal direction, respectively. The schematic view is shown in Figure 3.6.

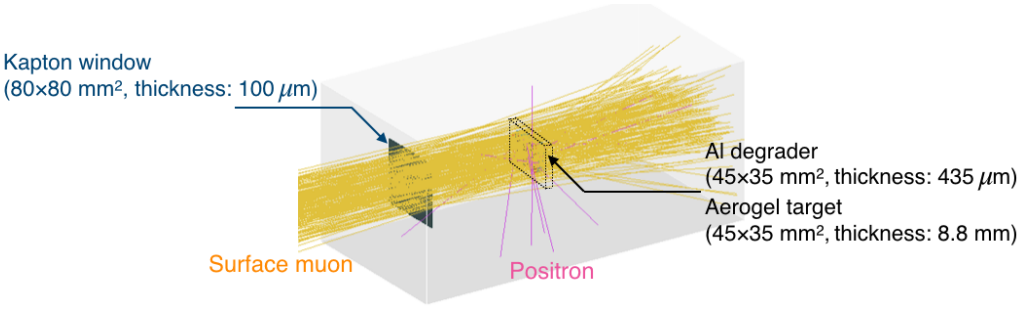

图 3.6 表面缪子停止模拟的 GEANT4 模拟方案。表面缪子束流通过用于分隔 S 束线和腔室之间的真空的聚酰亚胺薄膜（Kapton）和降能铝薄膜后到达硅凝胶靶材料。

Figure 3.6 Overview of the surface muon stopping simulation inside the silica aerogel. Surface muon was injected and passed Kapton window, Al degrader before reaching aerogel. Yellow tracks are surface muons.

The thickness of the Al degrader is optimized for the number of stopping muons, especially the number within the 2 mm from the downstream surface. Figure 3.7 shows the distribution of the stopping surface muons inside the aerogel when the thickness of Al degrader is optimized to be 360 μm. The stopping efficiency is 44.3% per incident surface muon. The mean stopping time for the muon is about 350 ns, starting from the generation of the surface muon at the proton target.

From measurement, it is known that 52% of the stopped muon form Mu inside the aerogel[41]. But for the convenience of statistics, 100% of Mu formation was assumed in the simulation. The factor of 52% is counted in the final efficiency.

Figure 3.8 shows the scan of the degrader thickness. The number of the total stopping muon is maximum when the thickness is 420 μm. However, from the diffusion simulation (see Section 3.3), it is more important to optimize the stopping number within a few millimeters of the downstream surface. The stopping numbers are maximum when the thickness is 360 μm when 2, 1, and 0.5 millimeters of the downstream surface. The FWHM width of the scan is approximately 94 μm within 2 millimeters.

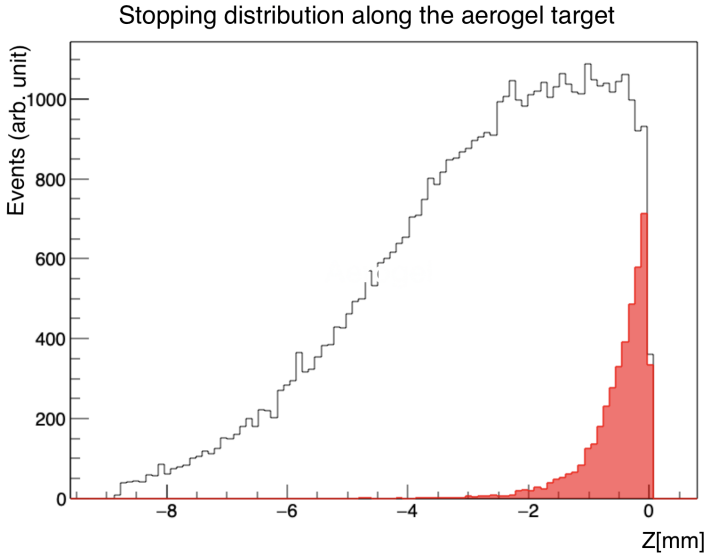

图 3.7　硅气凝胶靶内表面缪子的停止分布。束流在 z 方向射入硅凝胶。黑色柱状图显示所有停止在材料内的表面缪子的分布，而红色柱状图显示在扩散模型后从硅凝胶靶中溢出到真空中的缪子分布。

Figure 3.7　The stopping distribution of surface muon inside the aerogel target. The beam is shot into aerogel in z-direction. The black histogram shows the total stopping distribution of surface muon while the red histogram shows the Mu events who yield out of the aerogel target after diffusion model (see Section 3.3).

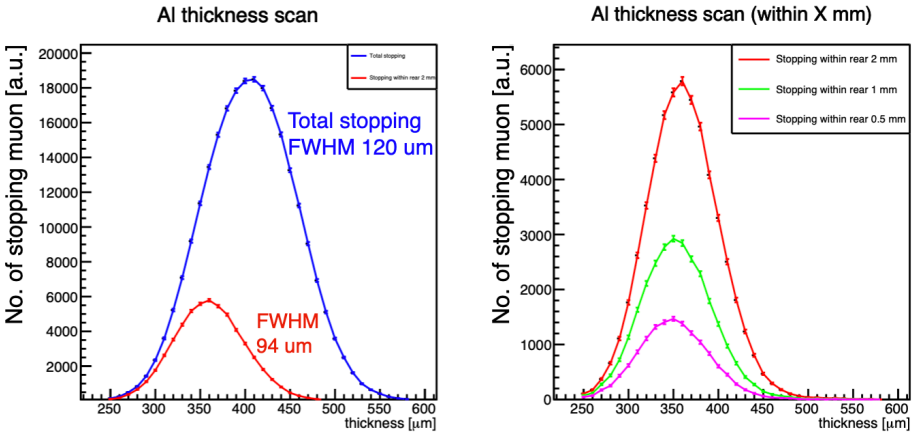

图 3.8　降能铝箔材料厚度扫描：左为在靶内停止的缪子数随着不同厚度的变化（蓝色）和在硅凝胶靶下游表面 2 毫米范围内停止的缪子数（红色）。右图为在硅凝胶靶下游表面 2 毫米、1 毫米、0.5 毫米范围内停止的缪子数随着不同厚度的变化。

Figure 3.8　The stopping number of surface muon inside the aerogel target as the funtion of degrader thickness. Left is the total stopping number (blue) and the stopping number within 2 mm of the downstream aerogel surface (red). Right is the stopping number within 2 mm (red), 1 mm (green) and 0.5 mm (purple) of the downstream surface.

3.3 Diffusion model

After the Mu stopping and formation, the simulation for the Mu diffusion process was developed. It describes the elastic scattering of the Mu atom inside the aerogel. After the diffusion process, Mu events yield into the vacuum and has a chance of being ionized by the laser at certain time.

3.3.1 Model construction and validation

Figure 3.9 shows the schematic overview of the Mu diffusion process. The Mu motion is modeled as a three-dimensional random walk to describe its scattering in the nano-porous structures of silica aerogel.

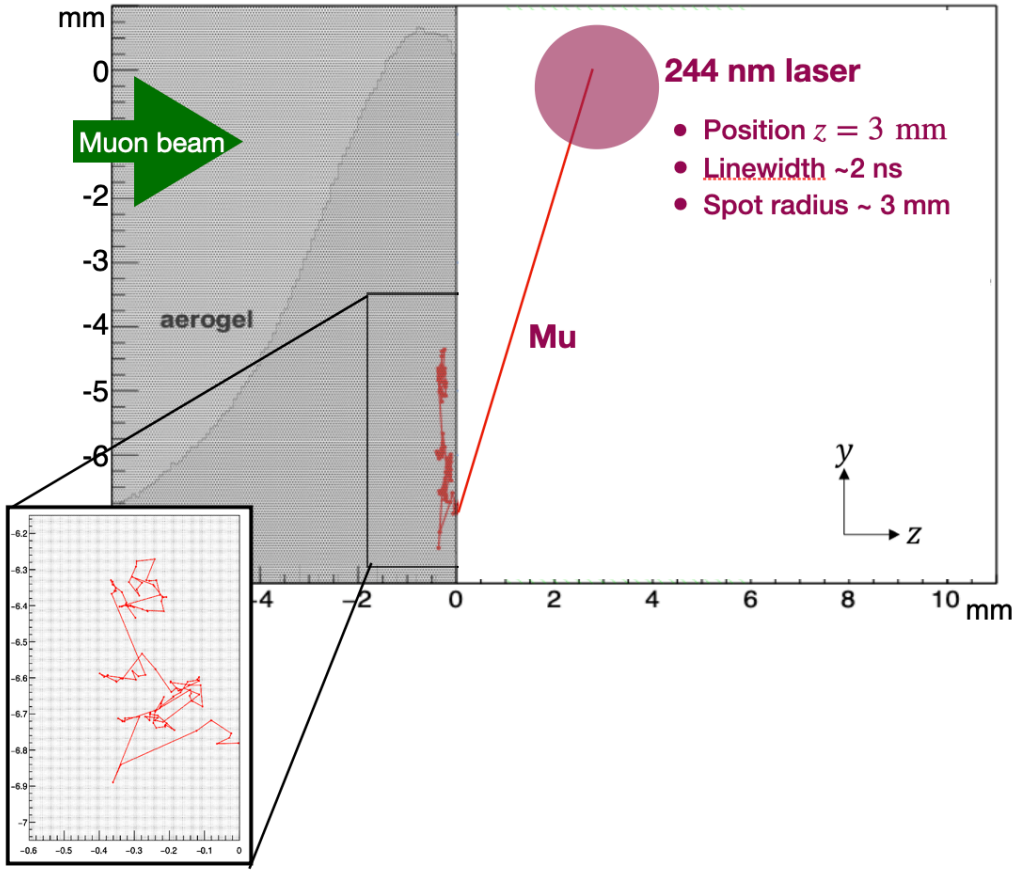

图 3.9 缪子素在硅凝胶材料内的扩散模型示意图。灰色阴影部分为硅凝胶材料。红色曲线展示了缪子素在材料内外的运动轨迹。

Figure 3.9 Overview of the diffusion model process of Mu from silica aerogel to the vacuum. The grey color indicates the aerogel material and the red tracks indicates the motion of Mu.

In this model, for each elastic scattering step, the velocity v of Mu is determined from the mean velocity $\overline{v}$ of the Maxwell-Boltzmann distribution[59] under the temperature T

$$\overline{v} = \sqrt{\frac{8kT}{\pi m_{\mathrm{Mu}}}} \tag{3.1}$$

where k is the Boltzmann's constant and m_{Mu} is the mass of Mu. The probability density function $P(l)$ of the scattering length l of Mu inside the aerogel follows the exponential distribution of displacement

$$P(l)dl = (1/l_{\mathrm{mfp}})e^{(-l/l_{\mathrm{mfp}})}dl \tag{3.2}$$

where l_{mfp} is the mean free path. The product of l_{mfp} and $\overline{v}$ is proportional to the diffusion coefficient D:

$$D = \frac{\pi l_{\mathrm{mfp}}\overline{v}}{12} \tag{3.3}$$

The above equation is described based on the definition of the three-dimensional diffusion coefficient $6D\overline{t} = \overline{l^2}$ as reported in[60], where $\overline{l^2} = 2l_{\mathrm{mfp}}^2$ and $\overline{t} = \frac{4l_{\mathrm{mfp}}}{\pi\overline{v}}$ is the mean time between collisions. If T and D are given, the velocity v can be derived from Equation 3.1 and the length l can be derived from Equations 3.2 and 3.3.

Mu diffuse until it reaches the surface of the aerogel, then continuing with the thermal speed in the vacuum.

The key parameters in the model, the diffusion coefficient D and temperature T, were determined by fitting the model to the measurement data with non-ablated aerogel samples[41] and laser-ablated aerogel samples[42]. In these measurements, decay positrons from emitted Mu were measured in the vacuum ranging from 10 to 40 mm to the surface of the aerogel, and the decay position of the Mu and its temporal evolution by the time were determined.

The effect of the laser-ablated structure on the aerogel surface is incorporated as an enlarged diffusion coefficient compared to the flat aerogel due to the voids and larger surface area that would increase the effective mean free path, which is consistent with the observation in the past TRIUMF tests.

A comparison between the data and the fitted model is shown in Figure 3.10. The Mu emission data in the vacuum region from 10 mm to 40 mm were used. There are three regions, each of which has 10 mm width. Time evolution is due to the combination of Mu diffusion into the vacuum, Mu flight in the vacuum with a thermal velocity distribution, and Mu decay.

The diffusion model, together with the exponential background from muons stopped in the aerogel, agrees with the Mu emission data. The uncertainties of the parameters were obtained by calculating χ^2 between the data and model simulation. In the case of laser-ablated aerogel, the optimal temperature T was determined to be 322 ± 2 K and the diffusion coefficient D was $870 \pm 30\,\mathrm{cm}^2/\mathrm{s}$ with a fit quality of $\chi^2/(\mathrm{d.o.f}) = 156/116$ (p = 0.7%). The diffusion coefficient was larger than the value fitted from the flat (non-ablated) aerogel ($D_{\mathrm{flat}} = 9.1 \pm 0.2\ \mathrm{cm}^2/\mathrm{s}$) by two orders of magnitude.

The model simulation shows that the initial position in the aerogel of Mu which can yield into the vacuum follows the exponential distribution starting from the downstream surface of the target. The direction of the Mu emission is distributed in an angle with an approximately $\cos\theta$ dependence concerning the perpendicular to the surface, fulfilling our naive expectations[49]. In the laser-ablated aerogel case, the characteristic depth for diffusion to the aerogel surface in the lifetime of muon τ_μ is $\sqrt{D\tau_\mu} = 0.43$ mm.

These results demonstrate that our diffusion model can successfully describe the Mu emission data from the silica aerogel. The extrapolation from our measurement region to positions closer to the aerogel surface is justified by the purely kinematic nature of the model.

3.3.2 Simulation result

Table 3.6 lists the critical parameters used in the simulation, which came from the best fitting on the laser-ablated aerogel samples in Section 3.3.1.

表 3.6　扩散模型中的初始模拟参数

Table 3.6　Simulation parameters in the diffusion model

Parameters	Value
Incident muon beam	one bunch pulses, FWHM: 100 ns
Pulses-x	Gauss(0, 31.96 mm)
Pulses-y	Gauss(0, 14.36 mm)
Aerogel Size	103 mm * 130 mm * 7.12 mm
Maxwell velocity T	322K
Diffusion coefficient	870 cm^2/s

In the Mu ionization experiment, the laser is centered at 3 mm from the downstream surface of the aerogel. The laser irradiation region is defined as a volume of $2 \times 40 \times 2$ mm^3 in the transverse direction and longitudinal direction.

Figure 3.11 shows the distributions of the total Mu yield on the surface and the evolution of Mu into the laser irradiation region as the function of yield time. The result indicated that

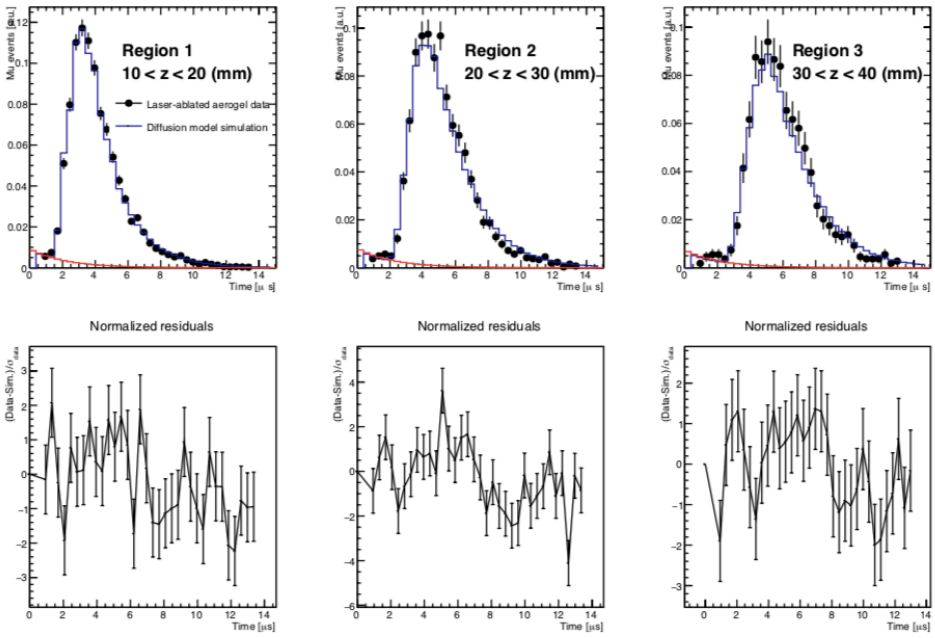

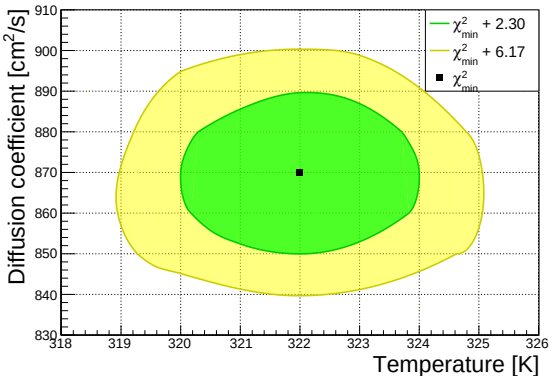

图 3.10　上图：起源于距硅凝胶下游表面 10 毫米至 40 毫米的真空区域的衰变正电子的时间分布（实心圆圈）、扩散模型的模拟结果（蓝色直方图）和指数本底（红色）。在本图中，扩散系数为 870 cm^2/s，温度为 322 K。下图：模型预测和测量数据之间的 χ^2 等值线图，以确定模型参数的不确定性。数据点来自[42]，可与图 1.10对比。

Figure 3.10　Top: Time distribution of the decay positrons originating in the vacuum region 10 mm to 40 mm from the aerogel surface (closed circles), the diffusion model prediction (blue histogram) and the exponential background (red). In this example, the diffusion coefficient is 870 cm^2/s, and the temperature is 322 K. Bottom: the contour plot of the χ^2 between the model prediction and measurement data for the 10mm to 40mm region to determine the model parameter uncertainties. Data points are from Ref.[42].

the optimum time for the pulse laser is near 0.8 μs after the average time of the arrival of the two surface muon beams pulses (0.6 μs apart between two centers).

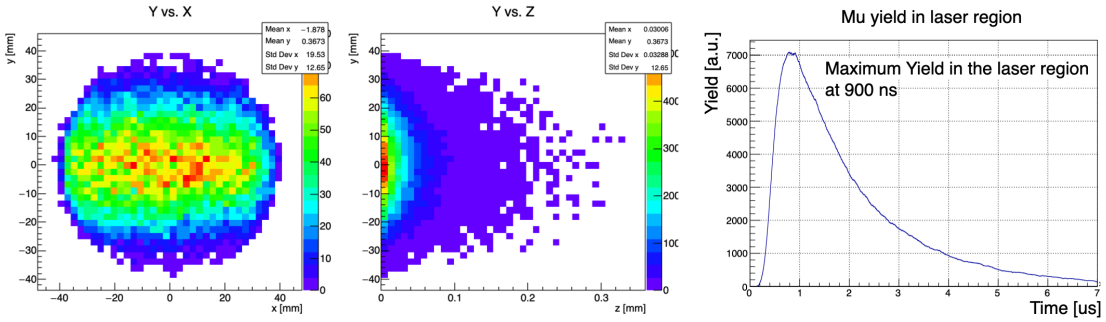

图 3.11　缪子素扩散模拟的结果。左二图为硅凝胶表面溢出的缪子素的累积分布。右图是作为时间函数的缪子素进入激光照射区域的数目演变。最大溢出数所对应的最佳激光照射时间约为 0.8 μs。

Figure 3.11　Results of the Mu diffusion. Left two are the accumulative distribution of the total Mu yield on the surface of the aerogel target. Right figure is the evolution of Mu into the laser irradiation region as the function of yield time. The maximum number is at 0.8 μs.

The 244 nm laser excitation simulation for the yield Mu was developed separately. The two-photon excitation and ionization probabilities of each Mu are calculated by numerically solving optical Bloch equations[61]. Simulation shows the probability for 1S state excited to 2S state is 8.8×10^{-7} and the probability for 2S state to ionization is approximately 44%. In total, the laser ionization efficiency is 3.9×10^{-7} per yield Mu in the vacuum region. These factors include the spatial and temporal overlap of the laser and the Mu events. The final efficiency of Mu vacuum yield is estimated to be 0.082.

Figure 3.12 shows the initial space distributions of the thermal muon at the laser ionization area as the input to the slow muon beam-line (SMBL) simulation.

3.4 Thermal muon extraction in SMBL

After thermal muons are generated by Mu laser ionization, the slow muon beam-line (SMBL) is employed to extract and transport the thermal muons.

The SMBL simulation is conducted by the "musrSim" program, which is a Geant4-based simulation program developed in PSI[62]. It was initially used to simulate the response of μSR instruments and later has become a general program for the beam-line experiment simulation with muon-specific classes (muon spin rotation, Mu formation, decay, etc.).

Figure 3.13 shows the construction of SMBL in musrSim. The electric fields of the SOA

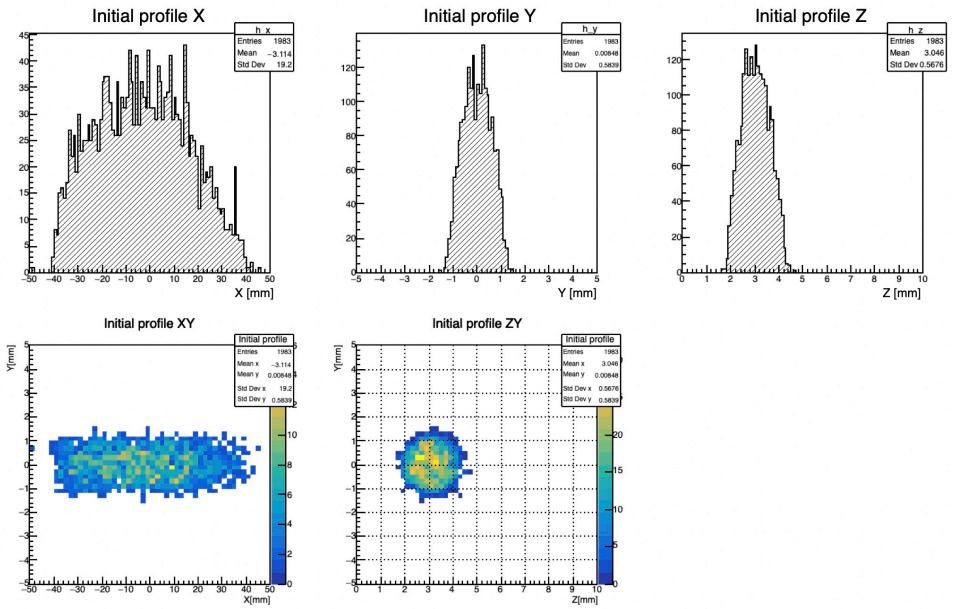

图 3.12　用于慢化缪子束线模拟的初始热缪子源分布。表面缪子束和热缪子的方向为 z 轴。左边是 XY 平面的分布，右边是 ZY 平面的分布。激光在 X 方向上射出，以 Z = 3 为中心，Y = X = 0，半径约为 1 毫米。

Figure 3.12　The initial thermal muon source profile for the SMBL simulation. Surface muon beam and the thermal muon extraction direction is towards z axis. Left is the distribution in the XY plane, right the ZY plane. The laser was assumed to be shot in the X-direction, centered at Z=3, Y=X=0, within the radius of about 1 mm.

lens, the ED, the EQs, and the magnetic field of the BM were generated by OPERA software[63] as a grid and implemented in the musrSim.

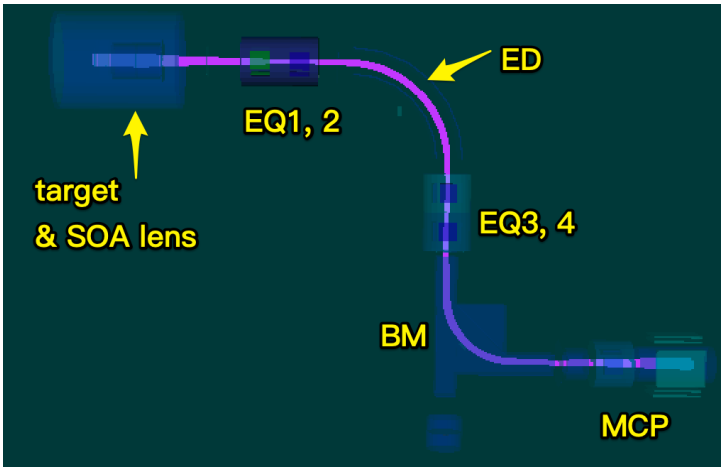

图 3.13 慢化缪子束线在 musrSim 模拟中的几何构建示意图。热缪子将被从左上方的靶与初级电极加速（SOA）传输到右下方的微通道板（MCP）探测器中。

Figure 3.13 The SMBL geometry construction in the musrSim simulation. From target and SOS (top left) to MCP detector, thermal muon is transported along beam-line.

The highest acceleration voltage of the SOA lens is set to be 20 kV. The decay positron from the incident muon or the electron produced by the field emission at the SOA lens is eliminated by the ED and the BM. The applied voltage for ED is 5 kV to bend the charged particle with the kinetic energy of 20 keV. Only the thermal muon can be transported to the MCP detector, where the rate of the thermal muon is measured.

The muon source is assumed to be generated at the center of the main chamber by two-photon laser ionization via 244 nm laser. For the rest of the individual components (SOA lens and various EQs), the strategy is to scan the different high voltage setups to investigate the change of the efficiency.

The goal of the SMBL optics design is to optimize the thermal muon transport efficiency, maximizing the thermal muon rate at the MCP detector. Table 3.7 listed the typical setups studied in the past Mu^- acceleration projects[56]. The study of turning processes on SOA, EQ12, are introduced from Section 3.4.1 to Section 3.4.3.

3.4.1 Tuning of SOA lens

The SOA lens consists of the mesh electrode (S1) and three metal plates (S2 to S4). The aperture of the S1 mesh and the inner aperture of the S2 lens are the same of 140 mm. Since

表 3.7　以往的缪子素相关研究中的光学设计总结。它们被用作本研究的调试起点。施加在 EQ 上的电压在水平 (H) 和垂直 (V) 电极上的极性相反。

Table 3.7　Results of optics design in the past Mu-related studies. They were used as the starting point of this study. The voltages applied on EQs are under opposite polarity on horizontal (H) and vertical (V) electrode.

Components	High voltages (kV)	High voltages (kV)	High voltages (kV)
Target mesh	+20.00	+20.00	+20.00
SOA-S1 mesh	+20.00	+18.94	+19.00
SOA-S2	+20.00	+18.04	+18.00
SOA-S3	+20.00	+16.00	+16.60
EQ1 H/V	±2	0.0	0.0
EQ2 H/V	±2	+0.35/−0.35	+2.0/−2.0
EQ3 H/V	±2	+0.68/−0.68	+0.94/−0.94
EQ4 H/V	±2	−0.66/+0.66	−0.94/+0.94
EQ5 H/V	±2	0.0	+1.8/−1.8

S4 lens is grounded, the high voltages (HVs) to be determined in the tuning were the voltages on S1, S2, and S3.

With a high voltage difference between the target mesh and S1, the quicker initial extraction and less decay loss are achieved; the voltage on S1 is therefore started to be 19 kV with the target mesh to be 20 kV.

To determine the voltage at S2, HVs were scanned on S1 and S2. The simulation showed that the muon beam would not be focused when exiting the S2 lens unless the voltage applied on S1 and S2 were the same. Figure 3.14 shows the event display of the beam under corresponding voltage setups, where muons are saved inside the S2 lens if the voltages are the same on S1 and S2.

At the exit of SOA, the transport efficiency is estimated to be 0.853. Compared with 0.787 from previous setups, about 6% of the total events are saved if HV on S1 is the same as on S2. Such a feature determines the HV on S1 and S2 to be 19.00 kV.

The remaining parameter is the HV on S3. Figure 3.15 quantitatively shows the number of muon at the exit S3 and SOA as the function of the voltages on S3. The shift of the focusing position inside the S3 is observed. When the voltage applied on S3 decreases, the focusing effect becomes significant, and the focusing position shifts upstream. The turning point is at around 16 kV when the events start losing at the S3 exit and the SOA exit.

It is foreseeable that the beam is expected to have maximum defocusing inside the EQ12

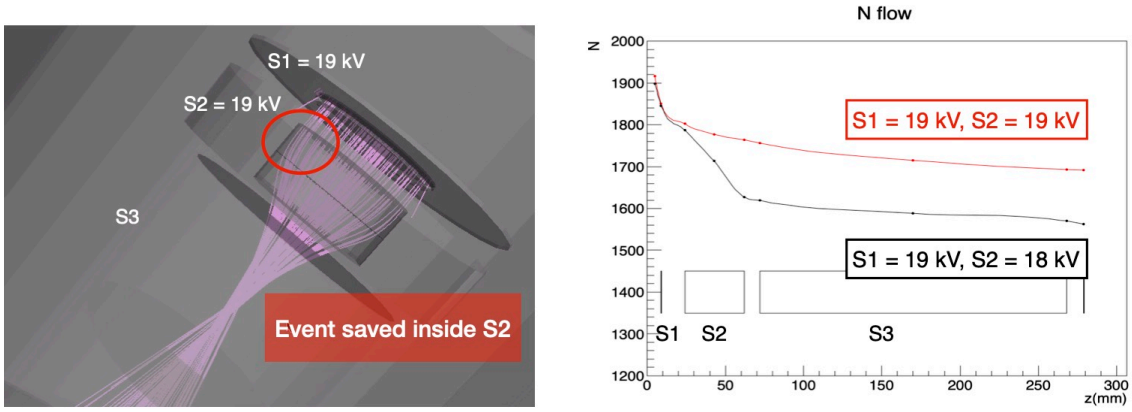

图 3.14　SOA 电极 S2 上的高压与 S1 相同时的缪子传输事件显示（左）。将此条件下的传输效率（红色）与 S1 高于 S2（黑色）的电压设置进行比较，可以看出传输效率明显提升。

Figure 3.14　Event display when HV on S2 is the same as S1 (left). The transport efficiency (red) under such condition is compared with the voltage setup where S1 is higher than S2 (black).

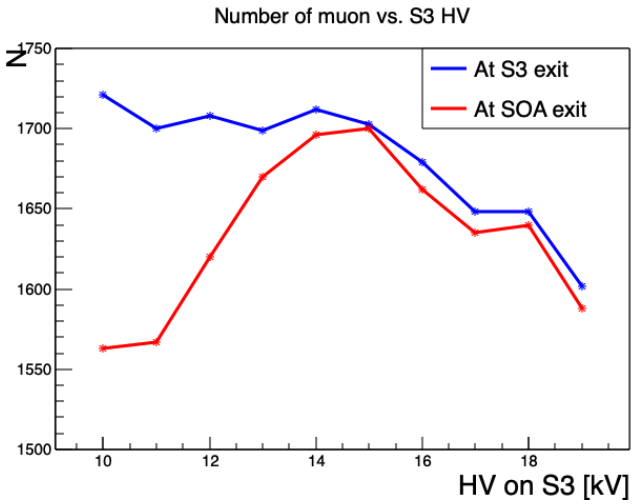

图 3.15　经过传输的慢化缪子数目与 S2 电压之间的关系。蓝色曲线表示在 S3 出口位置的数目；红色曲线表示在 SOA 末端位置的数目。转折点在 16 kV。

Figure 3.15　The number of muon at S3 exit and SOA exit as the function of voltages on S3. The highest rate corresponds to a voltage of 16 kV.

at the downstream position. A reasonable amount of events are needed. With all these considerations, the HV on S3 is set to be 15.00 kV.

Table 3.8 summarize the tuning result of voltages applied on each SOA lens.

表 3.8 SOA 高压数值优化总结

Table 3.8 Optimized HVs on SOA

Electrode	Optimized high voltage [kV]
SOA-target	+20.00
SOA-S1	+19.00
SOA-S2	+19.00
SOA-S3	+15.00

3.4.2 Tuning of quadrupoles

Electric quadruples focus the beam in either a horizontal or vertical direction. DC voltages with opposite signs are applied to two pairs of electrodes in the EQ. The required voltage for focusing the beam by EQ is calculated from the transport matrix of the particle:

$$\begin{pmatrix} x \\ x' \end{pmatrix} = \begin{pmatrix} \cosh(kl) & \frac{1}{k}\sinh(kl) \\ k\sinh(kl) & \cosh(kl) \end{pmatrix} \begin{pmatrix} x_0 \\ x'_0 \end{pmatrix} \tag{3.4}$$

$$\begin{pmatrix} y \\ y' \end{pmatrix} = \begin{pmatrix} \cos(kl) & \frac{1}{k}\sin(kl) \\ -k\sin(kl) & \cos(kl) \end{pmatrix} \begin{pmatrix} y_0 \\ y'_0 \end{pmatrix} \tag{3.5}$$

The strength of the focusing of EQ, k, is described as $k^2 = -\frac{2qV_0}{a^2mv^2} = -\frac{qV_0}{a^2T}$, where a is the distance between the center of the EQ and the head of the electrode, T the kinetic energy, V_0 the voltage, q the charge of the particle, l the length of the EQ. Using the strength factor k, the focal length f of the EQ can be described as

$$\frac{1}{f} = \pm kl \tag{3.6}$$

Figure 3.16 shows the simulation display under our quadruple, where the distance between the focusing position and the quadruple is about 210 mm. The muon beam becomes parallel after passing the EQ with voltage 0.96 kV applied.

Following the calculation, the voltage applied on the EQ1 is set to be 1.25 kV with the focal distance from the focusing position inside the SOA-S3 to the center of EQ1 (The polarity

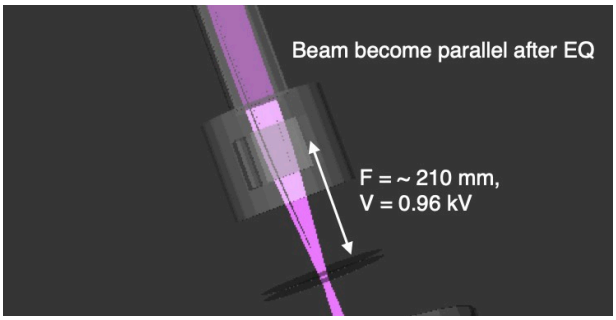

图 3.16　四极铁电压的调试事件展示：在计算得到的电压下，平行入射四极铁的束流在经过中心处 210 毫米后聚焦。

Figure 3.16　The muon beam focused 210 mm from the quadruple become parallel under the calculated voltage applied on EQ.

of the voltage on the horizontal and vertical electrodes are opposite). The focusing direction of EQ1 is set to be horizontal (X) direction, considering the relatively broad profile initially in the horizontal direction. Figure 3.17 shows the event display of the beam on SOA, EQ1, and EQ2. The beam in the horizontal direction reaches maximum inside the EQ1 and meets the requirement.

A similar strategy goes for the voltage design of EQ3 and EQ4. Since both ED and BM have a weak focusing ability on the beam due to the fringe fields, the tuning of EQ12 and EQ34 were done to optimize the beam profile entering the ED and BM separately. Table 3.9 listed the focusing direction of each EQ and the corresponding voltages.

表 3.9　电四极铁（EQ）高压数值优化总结

Table 3.9　Optimized HVs on EQs (voltages are for the horizontal (H) and vertical (V) electrodes)

Quadruple	Focusing direction	Optimized high voltage H/V [kV]
EQ1 H/V	X	+1.25/−1.25
EQ2 H/V	Y	−1.25/+1.25
EQ3 H/V	X	+1.125/−1.125
EQ4 H/V	Y	−1.125/+1.125

3.4.3　Tuning summary on the muon intensity

Table 3.10 summarizes the optics design on the muon rate measurement for the Mu ionization experiment. In the Table, we also discussed the possibility of installing the fifth

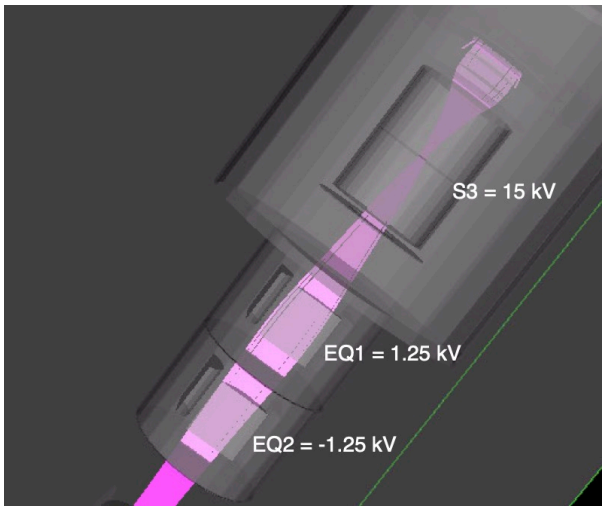

图 3.17　经过优化后，在 SOA、EQ1 和 EQ2 附近的缪子束事件示意图。

Figure 3.17　Muon beam event display on SOA, EQ1 and EQ2.

electric quadruple (EQ5) after the bending magnet and before the MCP detector. EQ5 is not installed for SMBL and this is proposed for future improvements. High voltages on each component are summarized under two conditions (with EQ5 or without EQ5). Figure 3.18 shows the beam event display by the optimized optics.

Figure 3.19 shows the comparison of the transport efficiency under two different conditions. With EQ5, the transport efficiency at MCP is 0.647, while it is 0.656 without EQ5. Similar transport efficiency is achieved under two conditions. At the MCP position, the radius of MCP of 21 mm was taken into account, and the events outside of the radius is not included.

3.4.4　Tuning for muon profile monitor

In addition to the beam profile monitored at the end of the SMBL, utilizing a beam-line as the profile monitor to the thermal muon at the laser ionization region is another potential study of the Mu ionization experiment.

The MBPM at the SMBL (straight end) to monitor the 2D beam profile of accelerated muon was introduced in Chapter 2. Using the initial profile from Figure 3.12, the tuning of the voltages on SOA lenses, the EQs were performed. The voltages on S1 and S2 are set to be 19.9 kV. Figure 3.20 shows the transport efficiency and the features of the beam profile σ_x and σ_y under different voltages on S3. In the evolution of σ_x, σ_y, if the voltage on S3 is relatively high, the voltage difference between the S2 and S3 is reduced, and the focusing position inside the S3 is shifted downstream. On the other hand, if the voltage on S3 is relatively low, the voltage

表 3.10 慢化缪子束线调试后的各高压与电流数值总结

Table 3.10 Summary of the optics design for SMBL, the voltages are listed for the horizontal (H) and vertical (V) respectively for EQs.

Component	High voltage [kV]	Current [A]
Target mesh	20.00	-
SOA-S1 mesh	19.00	-
SOA-S2	19.00	-
SOA-S3	15.00	-
SOA-S4	0.0	-
EQ1 H/V	+1.25/−1.25	-
EQ2 H/V	−1.25/+1.25	-
ED +/−	+4.7/−4.7	-
EQ3 H/V	−1.125/+1.125	-
EQ4 H/V	+1.125/−1.125	-
BM	-	16.26
EQ5 H/V	+1.5/−1.5	-

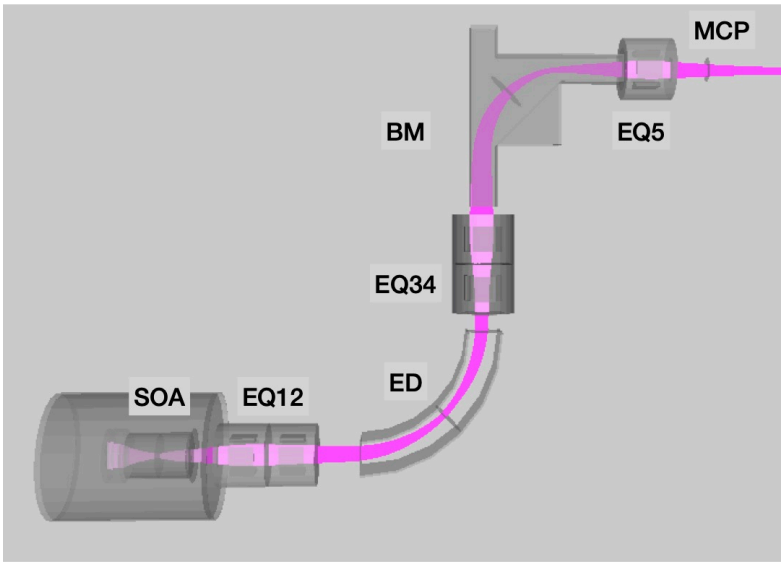

图 3.18 经过优化后的慢化缪子束线传输事例图

Figure 3.18 Event display of the SMBL optics with optimized optics.

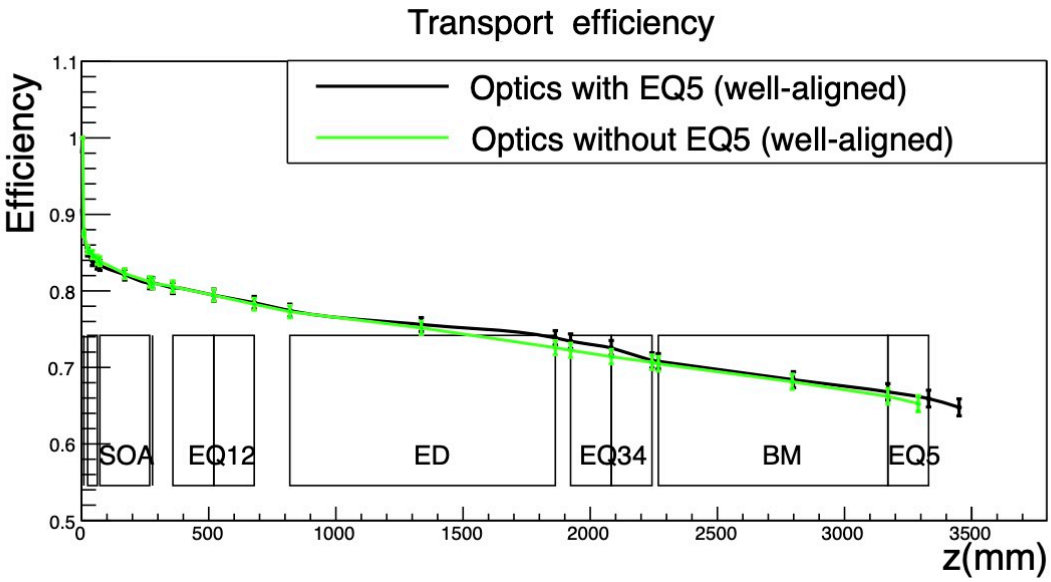

图 3.19　慢化缪子束线的传输效率示意图。在实验中我们设计了两种方案：安装额外的电四极铁（EQ5）的情况（黑色）与不安装电四极铁的情况（绿色）

Figure 3.19　Transport efficiency with EQ5 and without EQ5.

difference between the S2 and S3 is increased, and the focusing position shiftes upstream.

Such a feature determined the optimal HV value so that the beam reached the highest profile in the middle position of EQ1 and EQ2. The beam profiles were tuned to be σ_x and σ_y of about 15 mm so that the outermost part of the beam is covered by the aperture of the quadruple, which is 80 mm. Bottom left plot in Figure 3.20 shows the σ_x and σ_y dependence on S3 voltage at the center of EQ12. The S3 HV is 18.0 kV, yielding a beam profile of about 15 mm and a high transport efficiency.

Similarly, the tuning processes were performed with voltages of various EQs. Figure 3.21 shows the comparison between the initial profile before SMBL transport and the final beam profile at the MCP position after the optimization of the HVs obtained from the previous section. This figure also presents the correlation between the initial position of the beam with the final position of the beam, including the correlation between the initial X and the final X (horizontal), the initial Y, and the final Y (vertical).

It is found that within ±20 mm, there is an excellent linear correlation between the initial position and the final position for the transported events. Such a feature indicates the potential to track the profile at the MCP back to the profile at the laser ionization area, which is usually difficult to be monitored.

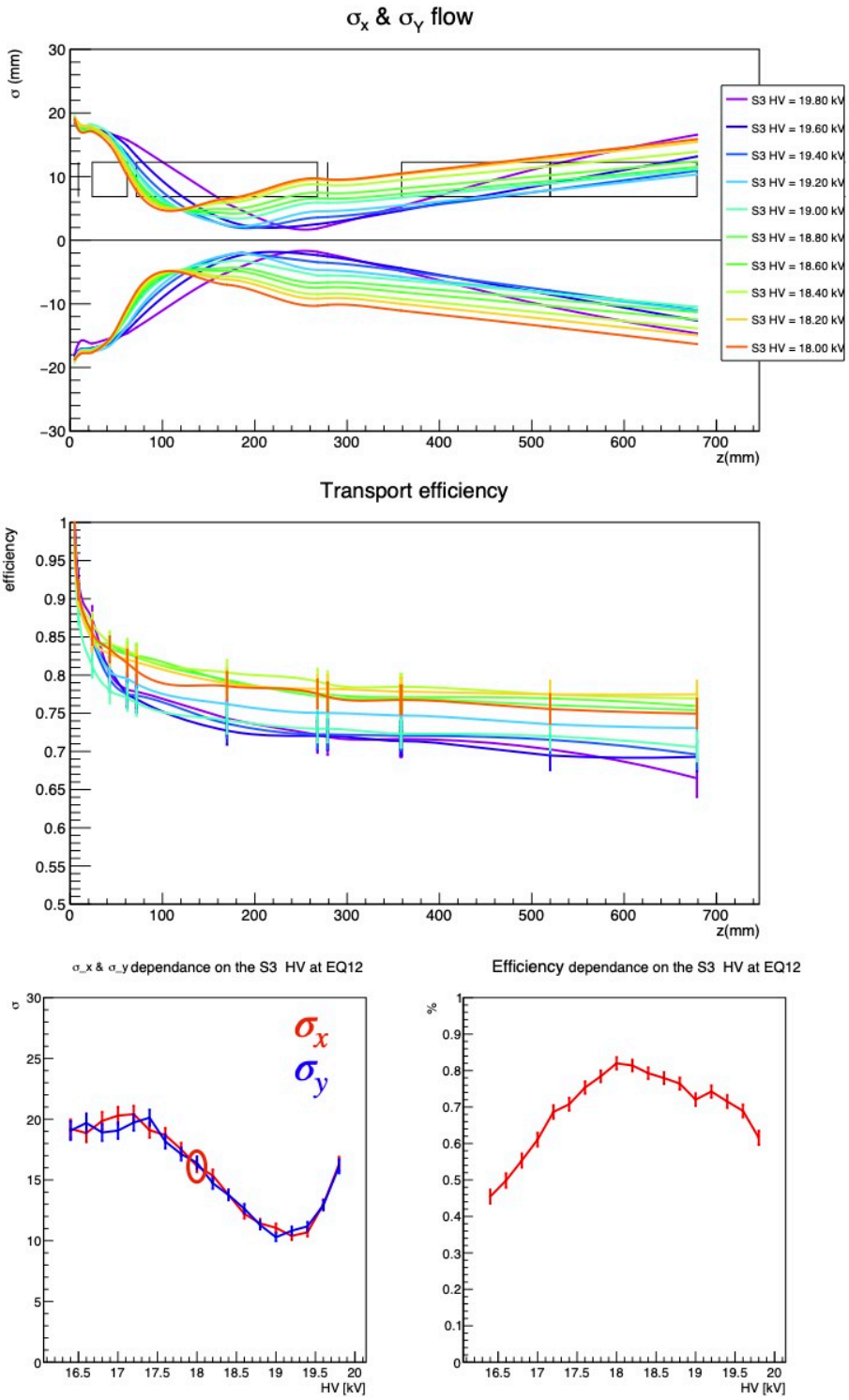

图 3.20 顶图与中图：缪子的空间轮廓、传输效率随着传输距离变化关系。底图：缪子空间轮廓与传输效率随着 S3 电极的电压变化的关系。

Figure 3.20 The result of the transport efficiency and the beam profile under S3 HV scan.

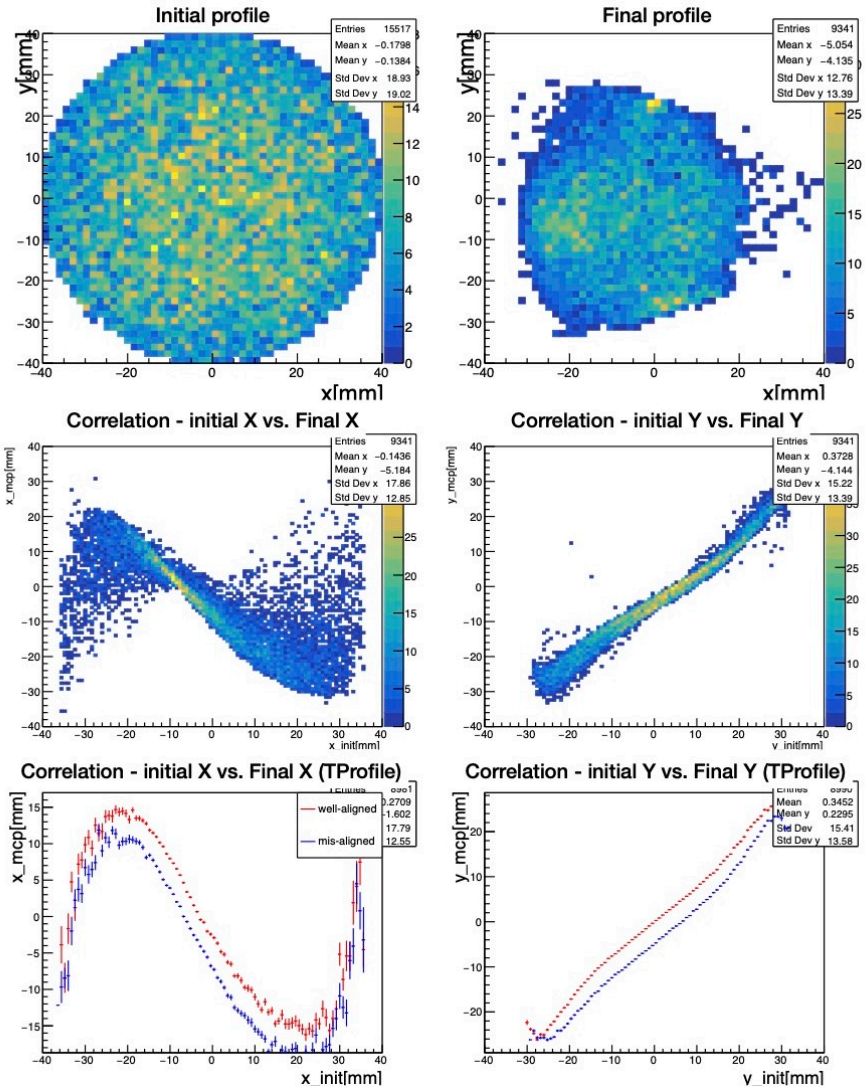

图 3.21　束流轮廓在初始位置（顶部图）和最终探测器位置（中部）的比较以及初始位置和最终位置之间的相关性（底图）。分水平 (X) 位置和垂直 (Y) 位置呈现。

Figure 3.21　Comparison of the initial and final beam profile (top) and the correlation between the initial position and the final position. Horizontal (X) position and vertical (Y) position are presented respectively.

3.5 Summary

Table 3.11 summarized the optimized optics in this simulation study, including the optics for the muon intensity (with or without EQ5), as obtained in Section 3.4.3, and the optics for the profile monitoring obtained in Section 3.4.4.

表 3.11 慢化束流高压与电流优化调试结果总结

Table 3.11 Summary of the optics design for SMBL

Components	Voltage (with EQ5) [kV]	Voltage (without EQ5) [kV]	Voltage as profile monitor [kV]	Optimized current [A]
Target mesh	20.00	20.00	20.00	-
SOA-S1 mesh	19.00	19.00	19.90	-
SOA-S2	19.00	19.00	19.90	-
SOA-S3	15.00	15.00	18.00	-
SOA-S4	0.0	0.0	0.00	-
EQ1 H/V	+1.25/−1.25	+1.25/−1.25	+1.31/−1.31	-
EQ2 H/V	−1.25/+1.25	−1.25/+1.25	−1.31/+1.31	-
ED +/−	+4.7/−4.7	+4.7/−4.7	+4.7/−4.7	-
EQ3 H/V	−1.125/+1.125	+1.25/−1.25	−1.12/+1.12	-
EQ4 H/V	+1.125/−1.125	−1.125/+1.125	+1.12/−1.12	-
BM	-	-	-	16.26
EQ5 H/V	+1.5/−1.5	-	−0.56/+0.56	-

The breakdown of the efficiency for the Mu ionization experiment via 1S-2S excitation is summarized in Table 3.12. The intensity of ionized thermal muon is estimated starting from the surface muon intensity of 2.4×10^6 per bunch at 500 kW proton power at S2. In total, Mu ionization generated 2.0×10^3 thermal muon events, and 1.5×10^3 events reached the MCP detector. The transport efficiency is estimated to be $(58.6 \pm 0.9)\%$, including 13% of decay-loss, 85% of the mesh transport efficiency, and the 90% of the MCP aperture ratio.

The final thermal muon counting rate was estimated to be about 0.28 Hz, which is enough to demonstrate the laser ionization method within reasonable data taking time.

表 3.12　缪子激光电离实验的模拟细分效率总结表

Table 3.12　Breakdown of the simulation efficiency and muon intensity for Mu ionization experiment

Step	Efficiency	Event rate (Hz)
Transport efficiency along S-line to S2	0.00717	2.4×10^{6}
Surface muon Stopping	0.467	1.1×10^{6}
Mu formation	0.52	5.8×10^{5}
Mu vacuum yield	0.082	4.8×10^{4}
Laser ionization	1.0×10^{-5}	0.48
Slow beam line Transport	0.651	0.31
MCP detection efficiency	0.90	0.28

4 Hardware Preparations on SMBL for Mu Ionization Experiment

This chapter describes the hardware preparation on the slow muon beam-line (SMBL) for Mu ionization experiment. After the proposal of the experiment, the re-configuration work was performed on the SMBL at High Energy Accelerator Research Organization (KEK). The bending direction of the beam-line was changed, and the beam-line alignment was improved. After the alignment measurement, an operation test was performed with the Hydrogen source.

4.1 Re-configuration of the SMBL

The beam-line re-configuration was performed in 2020 to change the bending direction so that SMBL matches the MLF S2 area. The activities included the design of the main chamber support, reassembling of the SMBL, beam-line transport from KEK to J-PARC, and the beam-line alignment.

Figure 4.1 shows the comparison of the drawings between the old beam-line and the new beam-line. Figure 4.2 shows the comparison of the SMBL photos before and after this work. The bending direction has been changed and the uncessary components have been removed.

The disassembly and reassembly of the SMBL and its transport to J-PARC were conducted safely.

4.1.1 Main chamber support design

Before disassembling the SMBL, a new support frame was designed for the main chamber (MC). Figure 4.3 shows the drawing and the schematic view of the new MC support by MISUMI software[64].

4.1.2 Alignment measurement

The alignment of various components along the bean-line was measured after the re-configuration. The vertical and horizontal alignment measurements were conducted with auto-level, theodolite, and microscope. The measurement results are shown in Figure 4.5. Alignment of 1 mm level on average has been achieved.

The optimized optics for the SMBL in Chapter 3 was assumed to be ideally aligned. The simulation results are updated with the alignment measurements. The effect of the alignment

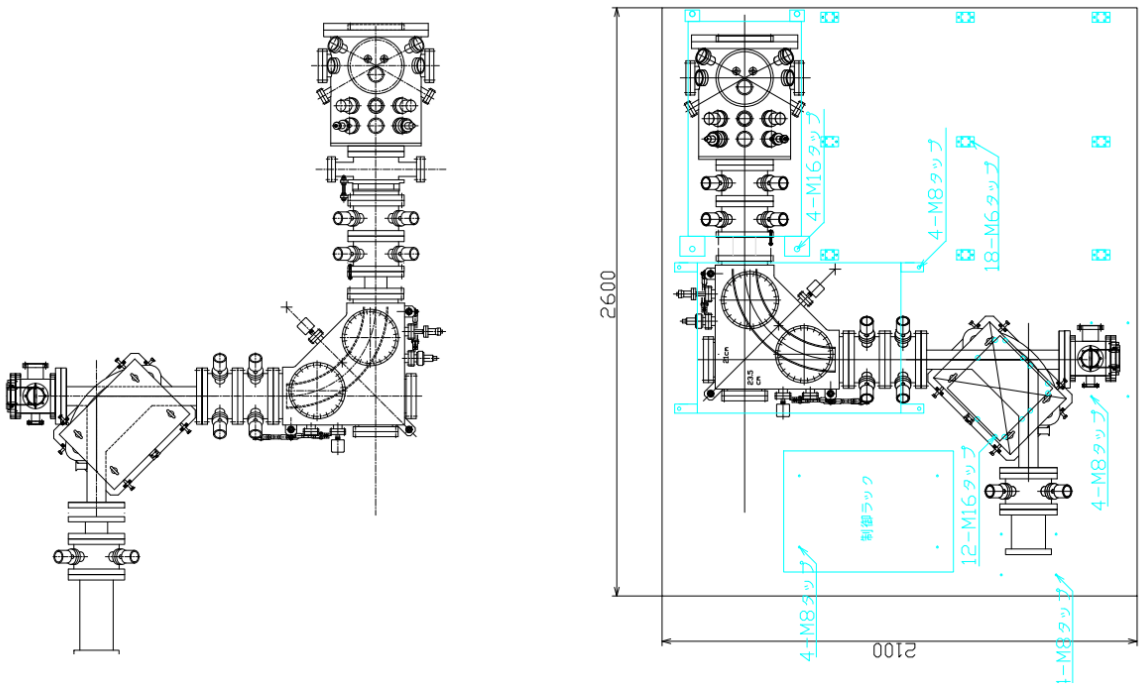

图 4.1　旧加速器束线（左）与新加速器束线（右）的设计图比较。新束线移除了多余的部分组件。

Figure 4.1　The comparison of the old beam-line (left) and new beam-line(right). The unnecessary components of the SMBL were removed in the new beam-line.

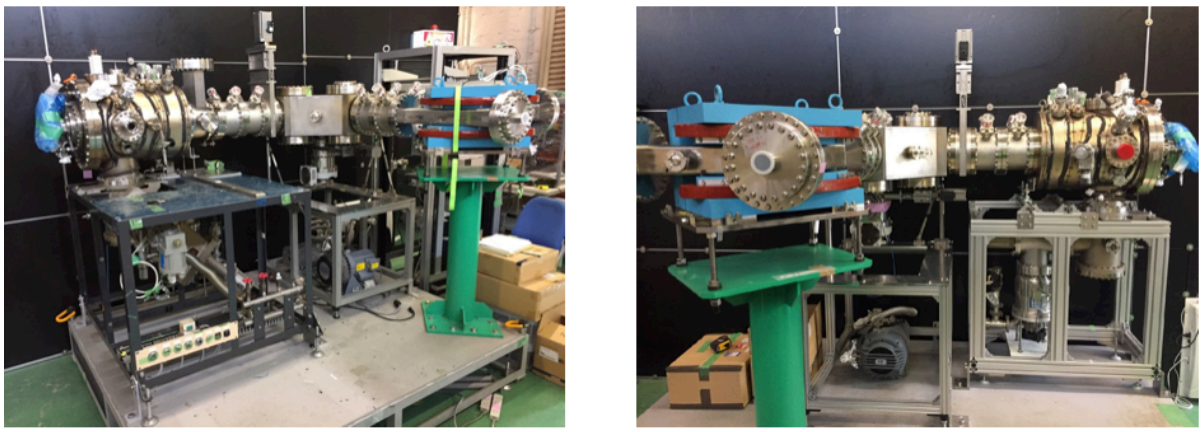

图 4.2　旧加速器束线（左）与新加速器束线（右）的实物图比较

Figure 4.2　The comparison of the old beam-line (left) and new beam-line(right)

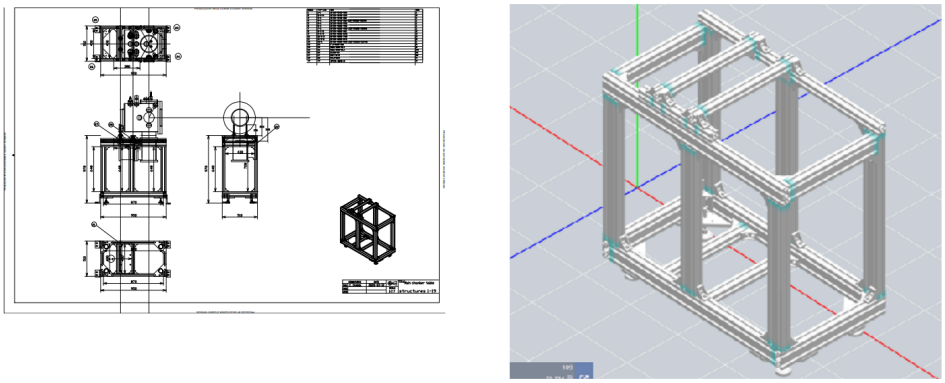

图 4.3　主室支架的设计图（软件：MISUMI FRAME）

Figure 4.3　The design of the new MC support by MISUMI FRAME

图 4.4　束线在 KEK 和 J-PARC 的校准活动示意。采用了自动水平仪和激光经纬仪等仪器对束线精确校准。

Figure 4.4　The activities of the alignment measurement at KEK and J-PARC MLF S2

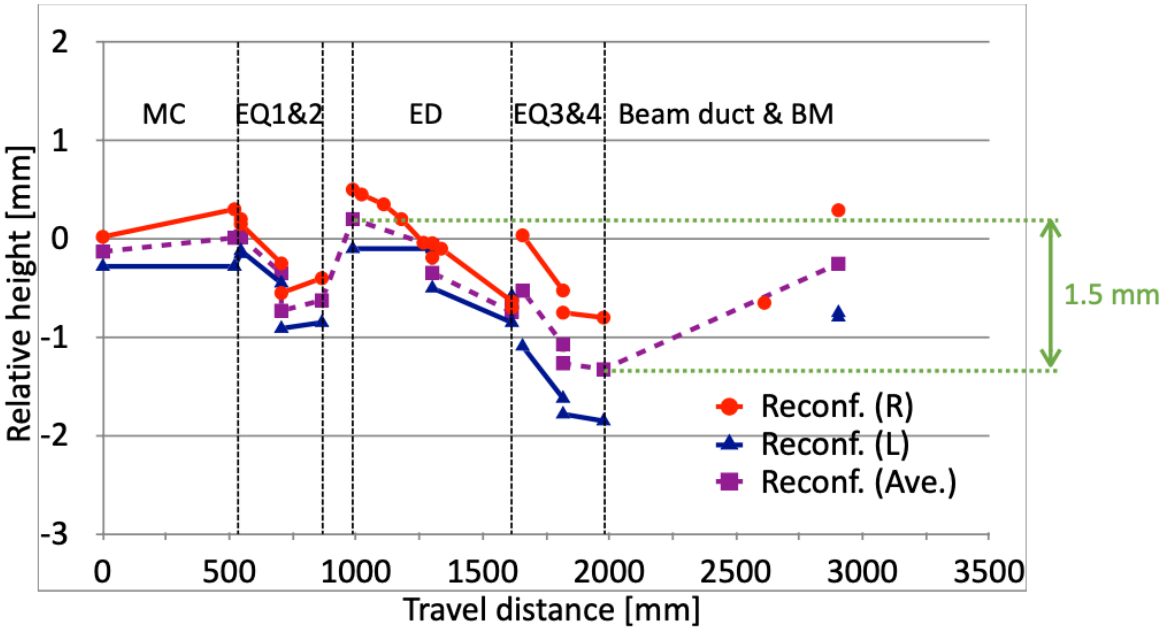

图 4.5　束线的高度校准结果。红色数据点是束线右侧校准结果，蓝色数据点是左侧校准结果。紫色数据点是平均值。我们确认了高度校准误差在 1 毫米以内，符合实验要求。

Figure 4.5　The height alignment measurement along the beam-line after re-configuration. Red color (R) indicates the measurement on the right side to the beam direction aligning the beam-line. Blue color (L) the left. Violent color is the average.

is incorporated into the simulation.

The alignment measurement of each component was directly calculated and set in the relevant Geant-4 files. In the simulation of the SMBL, the geometry was constructed by basic units such as tube, cylinder, and box, then transformed by rotation matrixs. The tilting angle, followed by each component's rotation matrix, was updated with misalignment measurement. Figure 4.6 shows the event display on the interface of SOA and the EQs in the simulation. From this display, it was confirmed that alignment effect was too small to be observed, especially in the vertical direction because the beam size was narrow. Since the beam profile is relatively broad in the horizontal direction, the vertical misalignment does not strongly affect the beam transport.

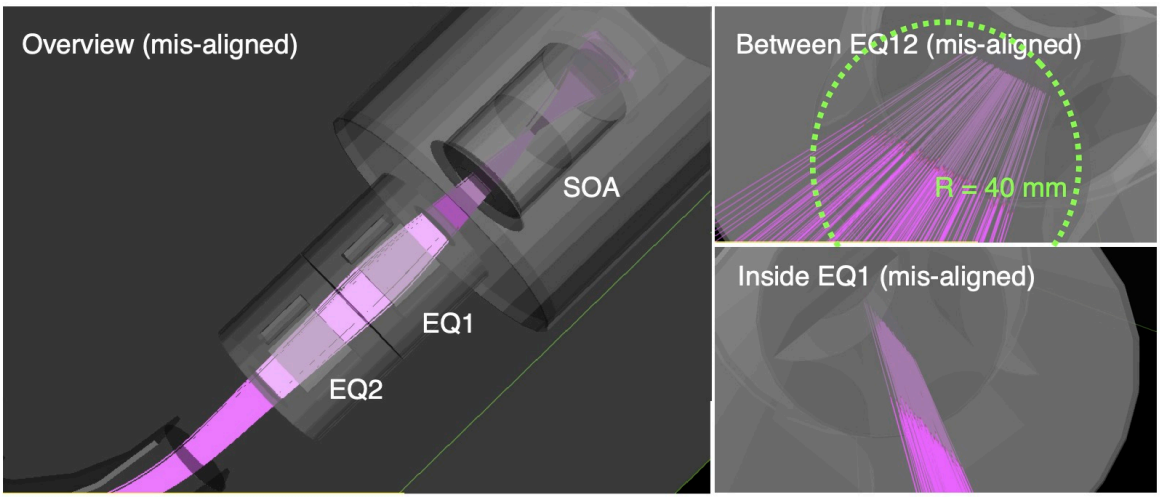

图 4.6　左：SOA 加速器中的事例展示，其中包括了校准的结果。右：电四极铁 EQ12 的放大展示，四极铁的半径为 40 毫米。

Figure 4.6　Left: the event display of the beam-line with the mis-alignment effect included. Right: zoom-in view of the event display at the EQ1 and EQ2, where the radius of the quadrupole is 40 mm.

After incorporating the alignment measurement, Table 4.1 summarizes the alignment measurement of each component on the final beam profile at the MCP detector. For each component such as SOA, EQ, ED, BM duct, and BM field, the misalignment in X, Y, or Z direction is tried with the shift of 0.5 mm, 1 mm, or 1.5 mm. In the simulation, the attempt to recover the transport efficiency has been conducted.

The well-aligned beam-line has a transport efficiency of 65.6% at MCP. It was found that the vertical shift of SOA has the most significant effect on the profile and the transport

表 4.1　在模拟中引入误差后，各个部件的校准精度对束流轮廓的影响总结。平均值（mean）与标准差（σ）代表束流轮廓中心位置及其误差。

Table 4.1　Summary of the effect of mis-alignment on the beam profile at MCP

SOA	EQ12	ED	EQ34	BM	EQ5	Mean$_x$	σ_x	Mean$_y$	σ_y	Trans. efficiency
Y+1						1.99	27.21	6.20	5.34	53.7%
	X+1					2.87	-0.27	7.75	7.54	66.0%
	Y+1					2.21	-26.02	7.21	6.45	60.9%
	Y+0.5					1.99	-13.67	7.44	7.25	62.6%
	Y+0.2					1.79	-5.87	7.54	7.52	63.6%
	Y-1					1.94	25.49	7.21	6.49	59.2%
		Y+1				1.99	0.13	7.44	7.63	66.1%
		Y+0.5				1.77	-0.31	7.42	7.68	66.4%
			Y+1			1.71	5.09	7.39	7.51	64.6%
			Y+0.5			1.85	2.37	7.43	7.43	65.8%
				Y+1		1.77	-0.46	7.42	7.76	65.9%
					X-1	2.13	-0.55	7.46	7.63	65.5%
					Y+1	1.93	-1.34	7.34	7.35	64.4%
					Y+0.5	2.05	-0.94	7.43	7.37	67.0%
					Y-0.5	1.71	0.09	7.34	7.35	67.8%
					Y-1	1.71	0.63	7.28	7.28	65.0%
					Z+1	2.33	-0.39	7.30	7.35	66.9%
					Z+0.5	1.98	-0.49	7.30	7.38	65.3%
					Z-0.5	1.68	-0.50	7.51	7.25	65.1%
Integrated with all the alignment measurement						1.80	-0.57	7.29	7.16	64.2%

efficiency, fullfilling our expectation since the SOA is placed at the most upstream to the beam, and the typical aperture of the SOA lens is 40 mm. In the actual measurement of the SOA chamber, the misalignment is less than 0.5 mm. For other components, the net relative change (NRC) on the efficiency is typically less than 1%.

With all the measurements integrated, the total effect leads to the updated transport efficiency of 64.2% (without EQ5), and the relative change compared with the well-aligned condition is −1.4%.

Figure 4.7 shows the evolution of the transport efficiency under various conditions. Table 4.2 compares the efficiency before and after the alignment simulation. The alignment effect caused about a 1% drop in the efficiency for the beam-line either with EQ5 or without EQ5. Moreover, the enhancement of transport efficiency has been achieved compared with the old beam-line before re-configuration.

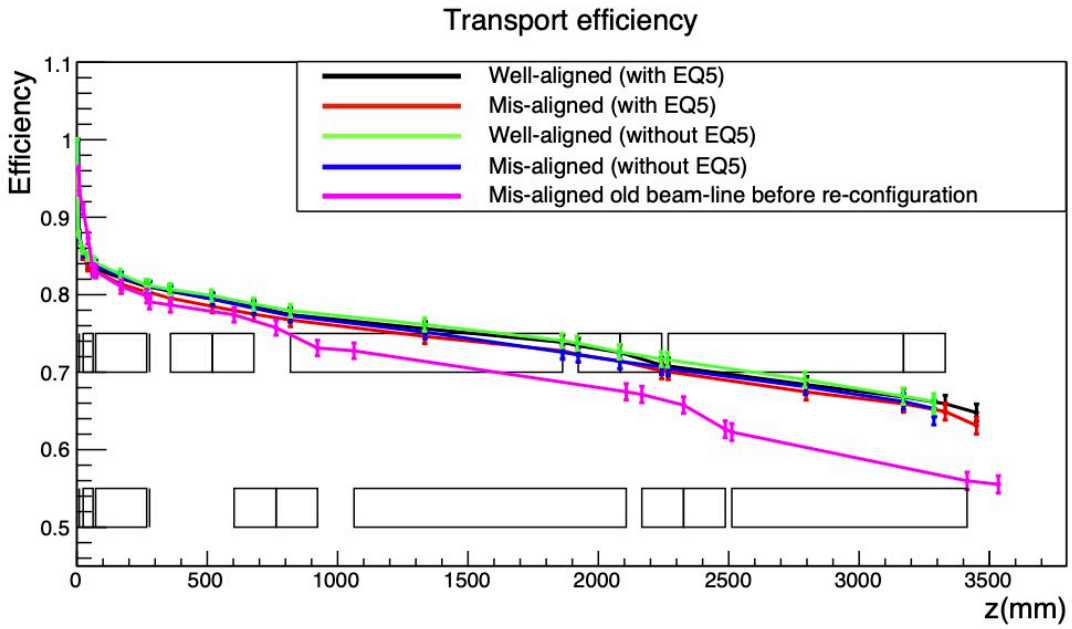

图 4.7　在各情况下加速器束线传输效率的结果：理想校准情况（well-aligned）、现实校准情况（mis-aligned）和在校准前的旧束线（old beam-line）的情况对比。对于新束线，传输效率在 0.63-0.66 范围内。

Figure 4.7　The result of the transport efficiency comparison under various conditions: the well-aligned beam-line, the mis-aligned beam-line with or without EQ5, and the old beam-line before re-configuration.

表 4.2　校准前后慢化缪子束线传输效率的对比

Table 4.2　Comparison on the SMBL transport efficiency before and after alignment simulation

	Ideally-aligned beam-line	Real beam-line
With EQ5	0.647	0.631
Without EQ5	0.656	0.642

4.2 Upgrade of remote control system

The operation of the SMBL, including the High Voltage (HV) application, the vacuum system, and the remote control system (see Chapter 2) was tested. In this work, the upgrade on the control system for the vacuum gate valve labeled as "V1" and "V2" was performed. The vacuum module was controlled via the SYSMAC C60P system in the past, originating from RIKEN-RAL. The alternative is the Programmable Logic Control (PLC) module through the EPICS control system.

The type of PLC module is the F3YC16 relay module from the Yokogawa company[65]. The WideField3 software[66] is used to write the logic design command into the existing Sequence CPU (F3SP71-4S), further distributing the power into each dedicated module. The control of different modules (High voltage modules, the vacuum gate valve module) was realized by functional PLC modules.

Figure 4.8 shows the diagram of the addition of the F3YC16 module to the existing system.

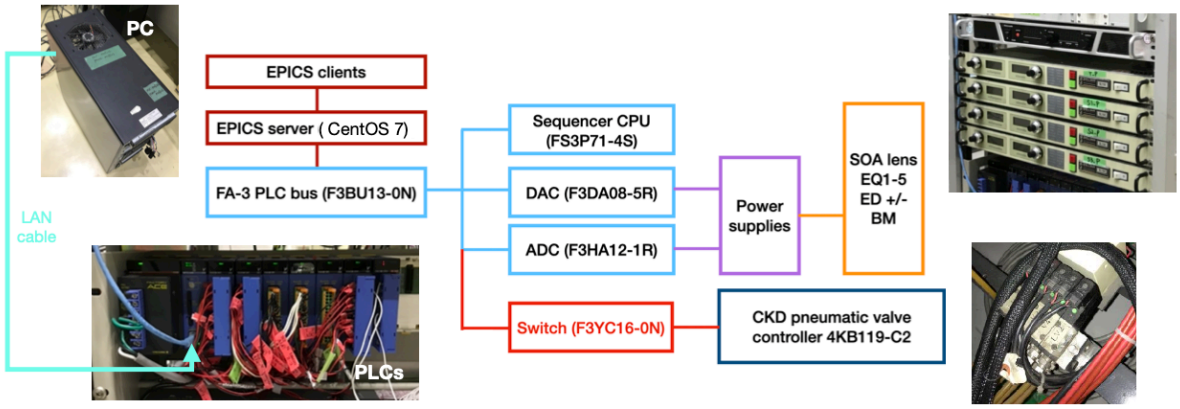

图 4.8　EPICS 控制系统的设计示意图

Figure 4.8　The diagram of the upgraded EPICS control system

There are several choices of the online interface tools available for EPICS. Extensible Display Manager (EDM)[67] is an interactive GUI builder, and the execution engine serves as the Display Manager on EPICS. EDM was used as the online interface for SMBL for a few years, but it only supports primary functions and lacks support community and further development. It is now no longer used in extensive facilities (KEK LINAC, J-PARC accelerator).

To achieve more advanced functions like the complex programming, and auto-logging system, Control System Studio (CSS)[68] interface is used. CSS is an Eclipse-based software toolkit to create the interface of large-scale control systems. It started at DESY and is now actively extended in international collaborations (like SNS and BNL). Both KEK and J-PARC accelerators are employing CSS. KEK has its CSS version: the Operator Interface (OPI) is BOY (Best OPI, Yet)[69]. It has a modern graphical editor, supporting Java and Python script programming, and has plenty of extensible widgets and plug-ins.

Figure 4.9 and 4.10 show the interface of the CSS, through which the control GUI is created. The voltage and the current of the various accelerator modules are monitored online.

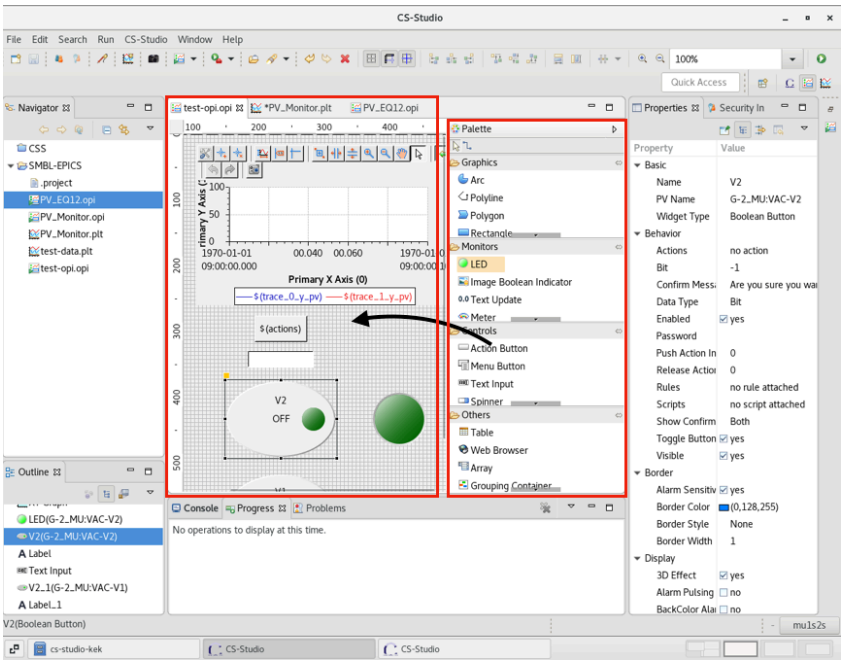

图 4.9 EPICS 系统的可视化界面图（采用 CSS 与 BOY 软件）

Figure 4.9 The interface of the CSS with BOY.

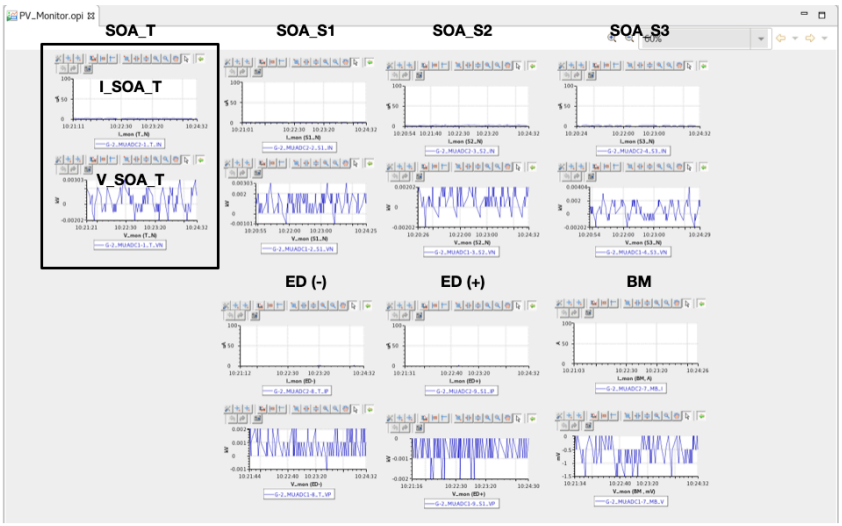

图 4.10　EPICS 系统的可视化监控界面（采用 CSS 与 BOY 软件），加速器的高压和电流值能被实时监控。

Figure 4.10　The control interface designed via CSS with BOY for monitoring the SMBL high voltage and currents.

4.3　Operation test with Hydrogen source

Before the muon source and the 244 nm laser became available at J-PARC, the H^+ source was used in the SMBL operation test (see Section 2.5.6 for setups). By this source, several functions of the SMBL were tested, such as the detector's performance and the voltage/current scan to confirm the beam-line is working normally after re-configuration.

4.3.1　Operation on MCP detector

In SMBL, there are two ends where the MCP detectors are installed, as shown in Figure 4.11. The single-anode MCP (SA-MCP) was installed at the bending exit after the bending magnet (BM), while the beam profile monitor (BPM) MCP was installed on the straight side after the BM. On the bending side, the intensity of the H^+ was counted, while on the straight side, the beam profile was monitored.

After applying the HVs on the beam-line with 2 kV, H^+ signal was successfully observed in the expected arrival time region. Figure 4.12 shows the images on the oscilloscope. From the oscilloscope, the Time of Flight (TOF) of H^+ was measured to be about 5.1 μs, consistent with the simulation prediction. The TOF was measured between the signal and the prompt electron and positron showers. We note that the raw signal from MCP was directly used without the amplifier.

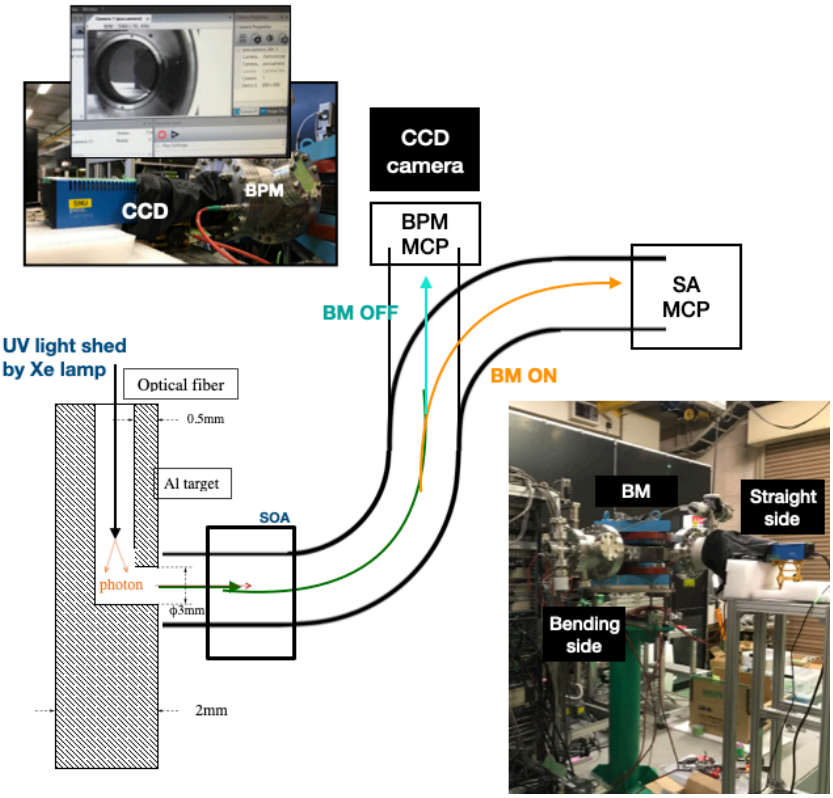

图 4.11　H^+ 加速的示意图。通过开关偏转磁铁，H^+ 信号能分别在偏转方向（SA-MCP）和费偏转方向（BPM-MCP）被探测到。

Figure 4.11　Overview of the H^+ acceleration test. By turning on/off the BM, the H^+ goes to the straight side (with SA-MCP) or bending side (with BMP-MCP).

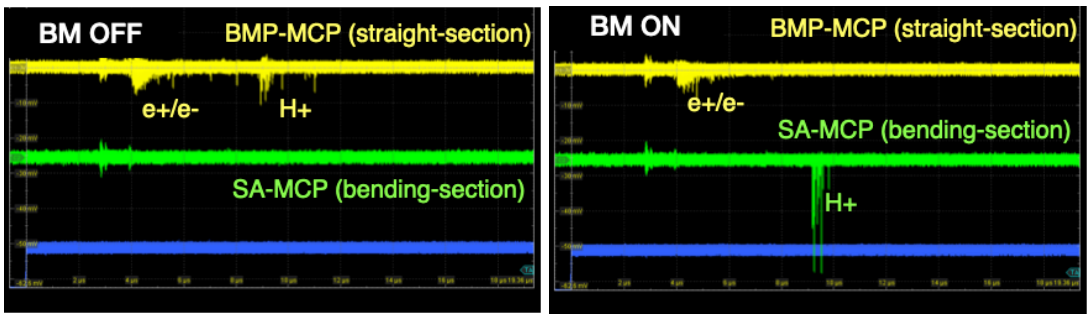

图 4.12　在示波器上观察到的 H^+ 信号。当偏转磁铁关闭时，信号在非偏转方向；当偏转磁铁打开时，信号在偏转方向。

Figure 4.12　H^+ signal at the oscilloscope. When BM was OFF, signal appears at the straight section. When BM was ON, signal appears at the bending section.

CAEN V1720 VME digitizer (12 bit, 250MS/s)[70] connecting to the SA-MCP was used to take data under the same SMBL optics. By accumulating 1.0000×10^4 triggered events (at 50 Hz), the signal waveform was recorded after subtracting the digitizer pedestals. Figure 4.13 shows the analysis result of the digitizer data. From the pedestal-subtracted waveform, the threshold of 5 ADC cut was applied. The rest was selected as H^+ signals in the TOF window.

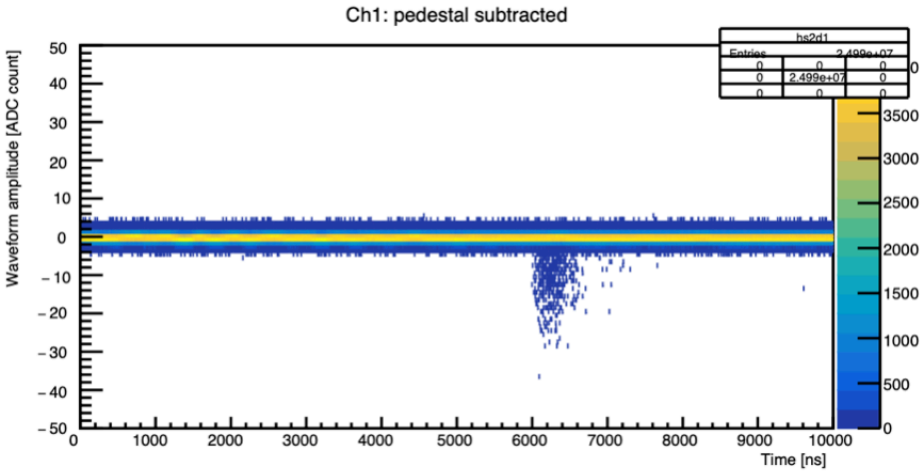

图 4.13　H^+ 信号经过数字化仪后的原始波形累计图。在合适的时间窗口内通过分析可以得到脉冲高度与宽度的分布。

Figure 4.13　H^+ signal after digitizer analysis. The pulse shape and height can be obtained within the time window from 6000 to 7000 ns.

The data analysis confirmed the performance of the beam-line and MCP detectors.

4.3.2　Bending magnet current scan

After the raw waveform at MCP, the Ortec amplifier 579[71] was used, adding gains to the digitizer DAQ system (the coarse gain was set to be 200 while good gain was 1). The signal intensity was improved by about two times. Under this setup, the scan of the bending magnet current was applied. By changing the BM current, the power of the magnet to bend the H^+ signals is different, and the signal rate at the bending side by SA-MCP varies. Figure 4.14 shows the result of the BM scan. The optimized current is 14.5 A, consistent with the theoretical calculation (14.53 A), and has better performance than the value of 15.03 A, which was used in the past.

Figure 4.14 also presents the comparison between the SMBL before and after the reconfiguration work (see Section 4.1). Due to the improvement in the alignment, the signal rate after the re-configuration is significantly higher than that before reconfiguration.

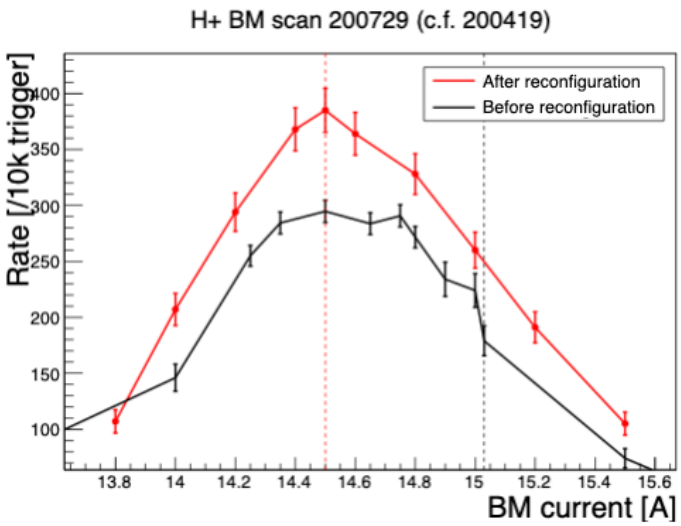

图 4.14　H^+ 信号随偏转磁铁电流的变化情况。14.5 A 是最佳偏转磁铁电流值，且与理论计算值相符合。红色数据点是加速器校准后的结果。黑色数据点是校准前的结果。

Figure 4.14　H^+ rate as the function of the BM current. 14.5 A was optimizedt. it is also consistent with theoretical calculation of 14.53 A. The red line indicates the signal rate after the re-configuration while the black before the re-configuration.

4.3.3 Beam profile

After the rate counting, the MBPM was used on the straight side to confirm its performance. Due to the relatively low energy of the accelerated H^+, only a few events were accumulated and selected. Figure 4.15 shows the signal observed at the oscilloscope. The proper time window of 1 μs was chosen to cover the arrival time spread of the H^+ signal. CCD shoots the picture and records it on the PC during the exposure time window.

Figure 4.16 shows the example result of the beam profile. From the raw data, the electron and position background were eliminated by looking at the 2D distribution of integral height and the pulse height. The pulse height was determined by the highest ADC counts at the arriving pulse, while the integral height sums up the ADC counts within nine surrounding bins for the entire arriving pulse. The signal H^+ is expected to create a dense electron and positron shower in the MCP. The higher the pulse, the lower the integral height of the background. When the pulse height is tall at the tail, the signal is differentiated from the background. The signal profile after the cut in the 2D region is obtained. The background was removed and the signal profiles were observed. More events are needed for further studies to analyze the profiles.

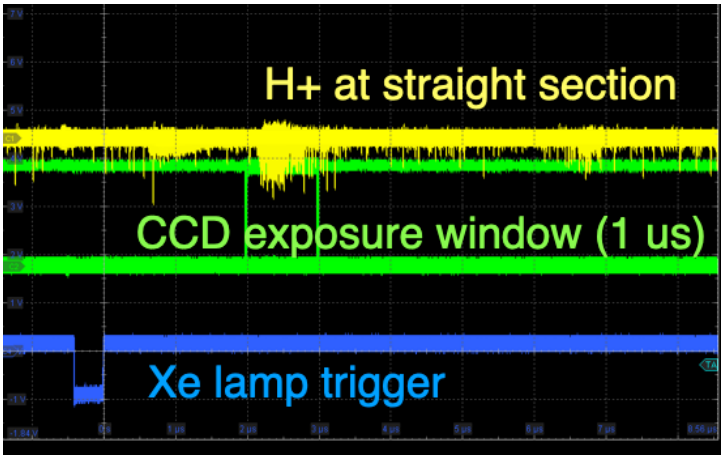

图 4.15　在非偏转一侧，H^+ 信号在示波器上的示意图（黄色）。同时显示了 CCD 照相机的曝光窗口（绿色）和氙灯的触发信号（蓝色）。

Figure 4.15　H^+ signal at the oscilloscope (yellow color), the CCD exposure window (green) and the Xe lamp trigger (blue).

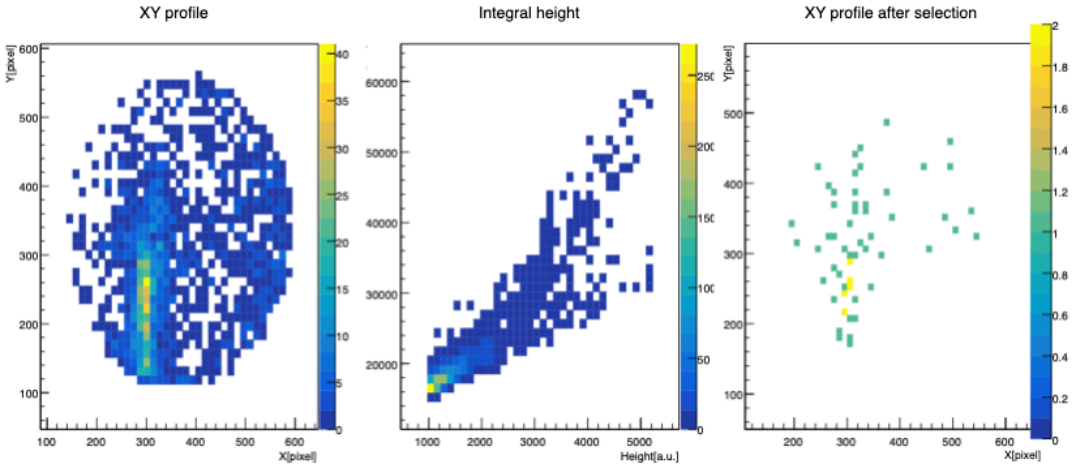

图 4.16　H^+ 束流轮廓的测量结果。最左侧是原始结果。中间部分是像素点的脉冲高度和积累脉冲高度的二维分布。

Figure 4.16　H^+ beam profile from MBPM. The leftmost is the raw example data. The middle is the 2D distribution of the integral height and the pulse height.

4.3.4 Laser ionization of hydrogen atom

The Hydrogen ionization test was also conducted in SMBL before its transport. The 243 nm laser was used, which excites the hydrogen by two-photon excitation (and the thrid photon for ionization), similar to the 244 nm laser for the ionization of Mu.

Figure 4.17 shows the setup of this test. The microwave cavity generated the H atom from the injecting H_2 gas. The 243 nm laser with a power of several mJ was generated from 976 nm External Cavity Diode Lasers (ECDL) and Optical Parametric Oscillator (OPO) technique.

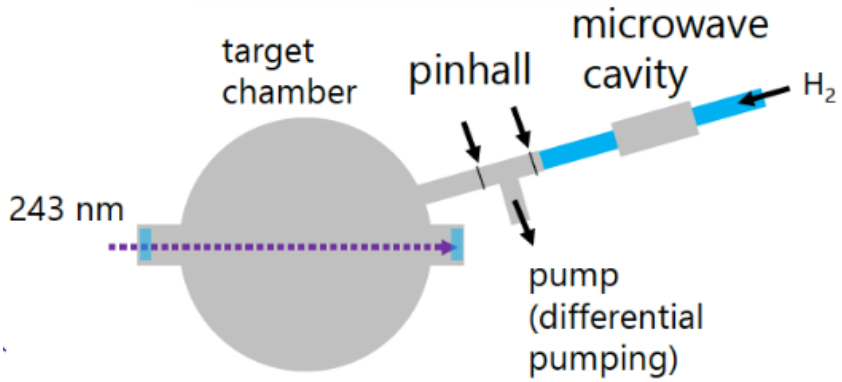

图 4.17 氢原子源从氢气分子中产生的示意图

Figure 4.17 Schematic of the H source generation from H_2 gas

The 243 nm laser at that time was unstable with significant pulse energy fluctuation. The specifications of the laser, such as the linewidth, were not determined. We proceeded with only two days of data taking. The laser frequency was scanned under different conditions in the source. The result is shown in Figure 4.18, the resonance frequency of 242.195 nm was determined, which corresponded to 616 THz of seed light in Figure. We concluded that the H atom two-photon ionization in the target chamber was successful and ready for the Mu ionization experiment.

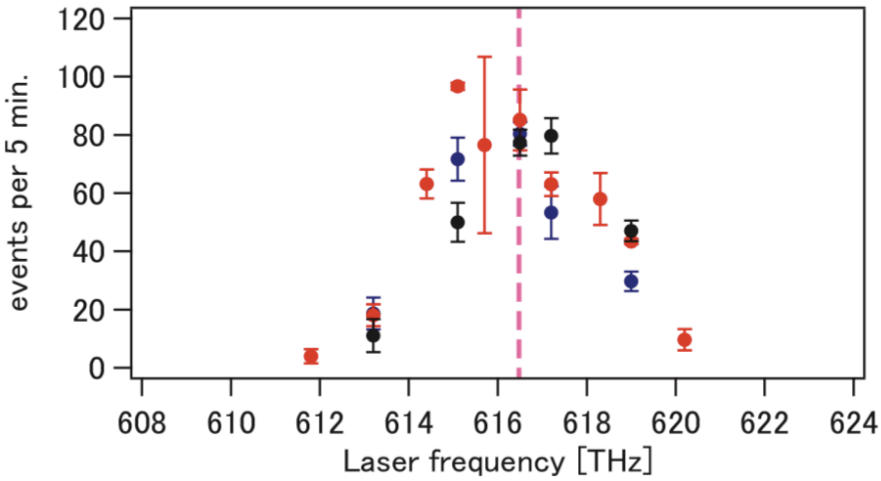

图 4.18　氢原子经由 234 纳米波长的激光电离的失谐曲线（计数率随激光频率的变化）。616 THz 附近的红色虚线表示校准的双光子共振频率。与圆点峰重合，认为靶室中的 H 原子双光子电离成功。不同颜色的数据点来自在示波器上观察来自 MCP 的信号，在不同条件下进行了多次测量，并对超过噪声水平的信号进行计数（各 5 分钟）。

Figure 4.18　Result of the hydrogen ionization experiment via 234 nm laser. During the two day's data taking, the wavelength of the laser was scanned. The round points are the signals obtained in this experiment and were measured multiple times under different conditions. The red dashed line near 616 THz indicates the two-photon resonance frequency calibrated in another experiment, which is consistent with the peak of the round point.

5 Experimental Data Taking from Mu Ionization Experiment

This chapter presents the experimental data taken from the Mu ionization experiment, which started from S2 area surface muon commissioning in July 2021, followed by the laser ionization campaign from January 2022 to March 2022. Data taking was under the J-PARC MLF proton beam power of 750 kW on average.

5.1 Surface muon commissioning at S2

After finishing the construction of the S2 experimental area, the surface muon beam commissioning was performed from July 16th to July 17th, 2021, and from January 15th to January 22nd, 2022. The SMBL was not installed during the commissioning. The delivery of the surface muon with a two-bunch structure separated by 600 ns was firstly confirmed at the oscilloscope. Several measurements were performed, including measuring the surface muon intensity, the surface muon beam profile, and the beam-line optics tuning.

5.1.1 Surface muon intensity

The rate of the surface muon was measured at the S2 area. The schematic drawing is shown in Figure 5.1. Two scintillators were set at the position 1.8 meters from an iron target. The surface muon beam firstly passed the Kapton window and hit the iron target, which has a thickness of 1 millimeter, to fully stop the incident surface muons. The scintillators detected the positrons from muon decay through a coincidence circuit triggered by the MLF synchronized time signal at 25 Hz.

The optics of the S-line started from the result of the simulation tuning in Section 3.1. Figure 5.2 shows the time distribution of the positron rate as the function of time. The fitting result shows the slope of -0.44E-3, consistent with the inverse of the muon lifetime ($1/\tau_\mu$ where $\tau_\mu = 2.2\mu$s).

The measurement in this run had a total pulse of 40015 and a total positron hits of 333656. The measured hit rate was 8.34/pulse or 208.5 Hz. The solid angle of the scintillator was calculated to be $A/(4\pi L^2)$, where A is the area of the scintillator and measured to be 25E-4 m^2 and L is the distance from target to scintillator (1.8 meters). The estimated muon intensity was therefore calculated to be

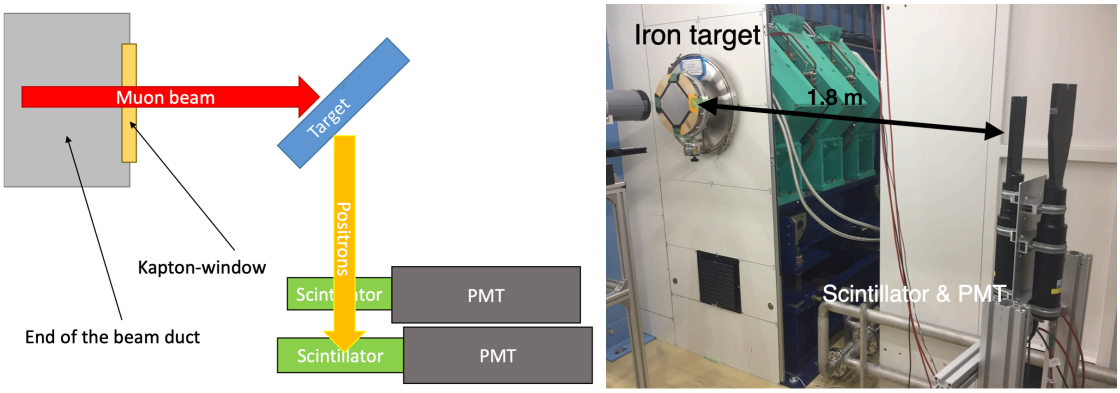

图 5.1　表面缪子束流计数率测量实验设置示意图（左）及其实物示意（右）

Figure 5.1　Schematic drawing (left) and the photo (right) of the rate measurement on surface muon at S2.

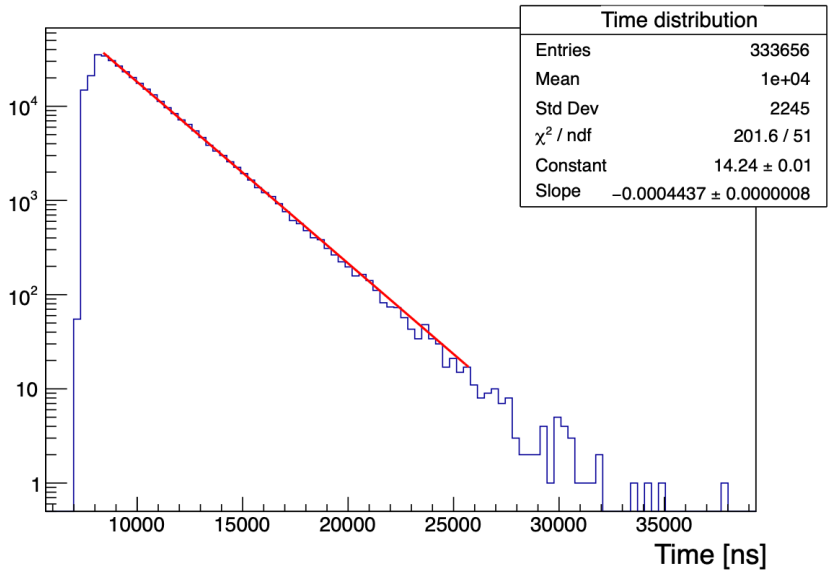

图 5.2　表面缪子束流计数率随时间变化的测量结果。纵向为对数坐标。红色直线为指数拟合结果。

Figure 5.2　Distribution of the surface muon intensity as the function of time.

$$208.5 \times 4\pi L^2/A = 3.78 \times 10^6 \text{ Hz} \tag{5.1}$$

On the other hand, the estimated muon rate at S2 by simulation in Chapter 3 is 3.6×10^6 Hz under 750 kW proton power. The measurement is consistent with the simulation prediction within statistical uncertainties.

5.1.2 Beam profile

The muon profile was measured by the profile monitor[72], consisting of a scintillator, an image intensifier, and a CCD. Figure 5.3 shows an experimental setup. A plastic scintillator disk was placed inside the gas chamber. Luminescence from the scintillator was amplified by an image intensifier and detected by a CCD camera. The scintillator and imaging detector were remotely controlled in synchronization. The entire setup was covered with a black sheet to shield an external light. The temperature of the CCD was controlled by an air-cooling fun and a Peltier element cooler.

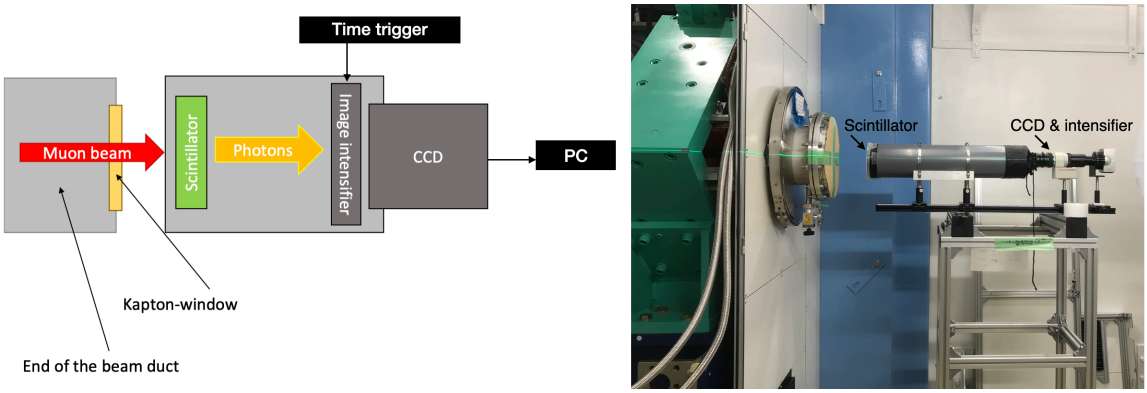

图 5.3 表面缪子束流轮廓测量实验设置示意图（左）及其实物示意（右）。缪子轮廓探测器包含一个闪烁体，一个图像增强器并由 CCD 相机检测。

Figure 5.3 Schematic drawing (left) and the photo (right) of the muon beam profile measurement at S2.

Figure 5.4 shows the results of the muon beam profile. The data taking time was scanned from 1 to 6 μs delayed from RCS kicker time (the arrival of the surface muon at the muon target). At each time, the image was taken under the shutter speed of 10 seconds and the exposure time of 100 nanoseconds. Each image has 7772 and 580 pixels in the horizontal and vertical directions, respectively. The calibration factor is 4.1 pixels per millimeter.

The CCD intensity was shown as the function of the delay time. Two bunch-structure was seen with the interval of 600 nanoseconds, within our expectation. When the time was set

at 1.9 μs, the beam profile showed the RMS width of 42.9 mm and 30.3 mm in the horizontal and vertical directions, respectively (without background subtraction).

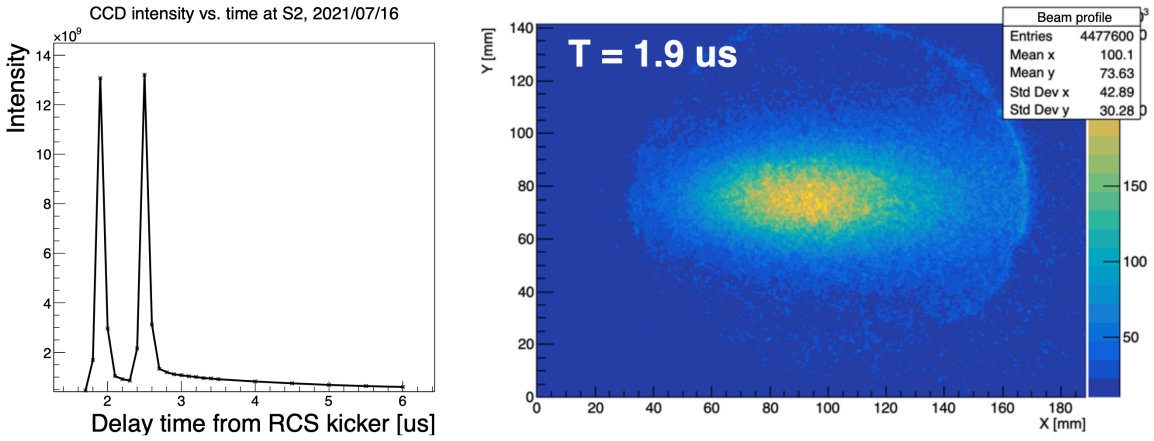

图 5.4　左图：表面缪子轮廓亮度随着取数触发时间的变化。双脉冲结构清晰可见。右图：在 1.9 微秒的取数时刻，表面缪子束流轮廓的测量结果。

Figure 5.4　Left: distribution of the surface muon intensity as the function of time, with two-bunch structure clearly observed. Right: beam profile at 1.9 μs.

5.1.3　Beam-line optics optimization

An auto-tuning program was developed to optimize the beam-line optics with a maximum muon beam rate[32]. The scintillators in Section 5.1.1 were used, and the rate of the positron was used as the input and goal of the optimization. Figure 5.5 shows the tuning process, where the hit rate was maximized by scanning the voltages on accelerator components from upstream to downstream step by step.

After optimization, the hit rate was increased by about 1.35 times than the original one. Table 5.1 summarized the change of the optics at the downstream quadruples after the auto-tuning program.

5.2　Data taking

5.2.1　Data set

After beam commissioning, the SMBL was connected to the S2 area together with a 244 nm laser. The Mu ionization experiment took data from January 23rd, 2022, to March 11th, 2022. Table 5.2 summarized the data sets during this period. The data set includes a scan of the laser frequency and other parameters (laser delay time, bending magnet current, and laser

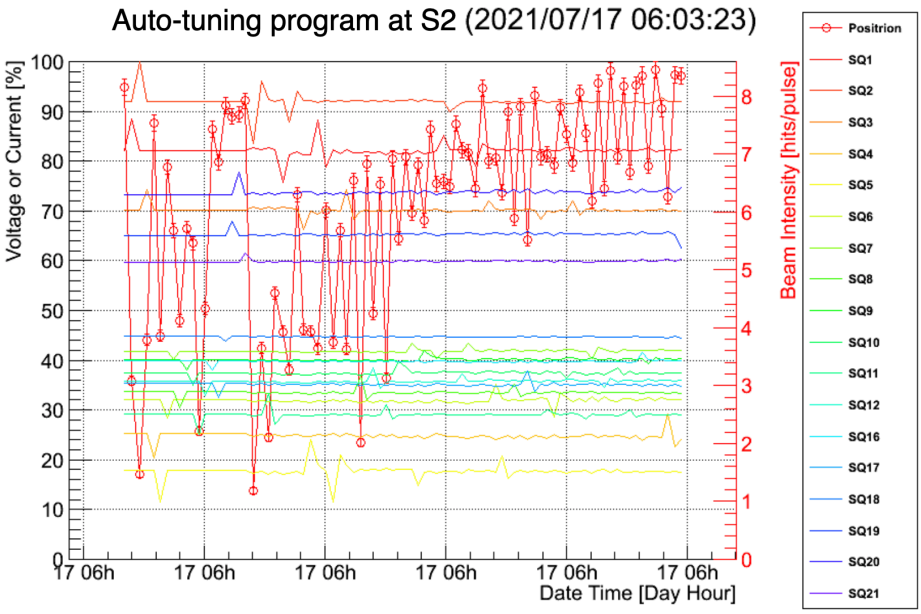

图 5.5　表面缪子束流计数率自动优化程序。红色空心数据点代表计数率随着每一次优化配置的变化。不同颜色的平行曲线代表不同加速器组件的高压值在优化程序中的变化。

Figure 5.5　Auto-tuning program to optimize the surface muon beam rate by scanning the voltages on various accelerator components. The red open circles are the positron hit rate measured at each setup. The different parallel colored lines presents the voltage value for each components.

表 5.1　经过自动优化程序调试后下游四极铁的电流配置总结

Table 5.1　Summary of the currents setups on the downstream triplet after auto-tuning.

Component	Current before tuning [A]	Current after tuning [A]
SQ16	50	49.88
SQ17	74.9	72.8
SQ18	24.8	25.88
SQ19	54.1	57.44
SQ20	81.09	82.59
SQ21	36	37.05

vertical position scan) to improve the signal rate. High statistics at resonance frequency were also taken after optimization. Finally, the beam profile was measured by MBPM.

表 5.2　缪子激光电离实验的实验数据列表

Table 5.2　Data set of the Mu ionization experiment

Data set	Laser energy [mJ]	Number of runs	Total acquisition time [hours]
Laser frequency de-tuning scan	1.2 - 1.8	18	3
Laser delay time scan	1.5	22	4
Bending magnet current scan	1.5	7	1.5
Laser vertical position scan	1.5	3	0.5
High statistics at resonance frequency	1.7	10	5
Beam profile measurement	1.7	10	2.5

5.2.2　Event selection

Waveforms from the MCP detector were digitized using CAEN V1720 VME digitizers (same as used in Section 4.3). The hit timing and pulse heights were extracted from the waveform data, as shown in Figure 5.6.

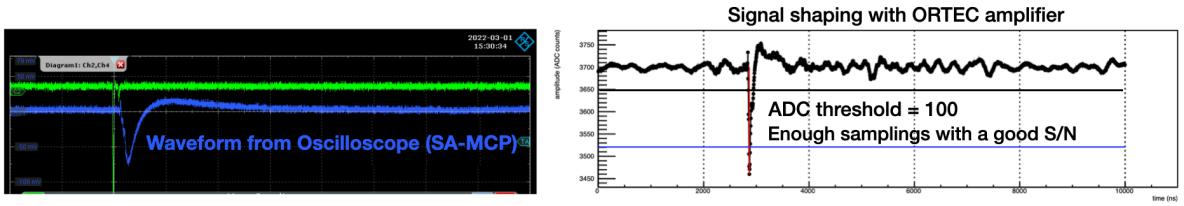

图 5.6　示波器上（左）MCP 探测器上（右）采集到的波形例子（右）。在脉冲高度分布图中，选择条件为大于 150 ADC 计数（对应 30 毫伏），能去除平滑的本底成分。

Figure 5.6　The pulse height and time distribution of the waveform collected at oscilloscope (left) and the MCP detector (right). The event selection is set to be larger than 150 ADC counts, which removes the flat background.

The pulse height threshold was chosen to be 150 ADC count, which corresponds to 30 mV, to remove the flat backgrounds caused by scattered electrons and positrons. Figure 5.7 shows the pulse height and time distributions from the MCP detector. In the 2-dimensional distribution of pulse height and time, the first peak at the time window from 2700 to 3000 nanoseconds was caused by the laser photon and referred to as the laser shooting origin. The

second peak in the time window between 3500 to 3800 ns was recognized as the ionized thermal muon.

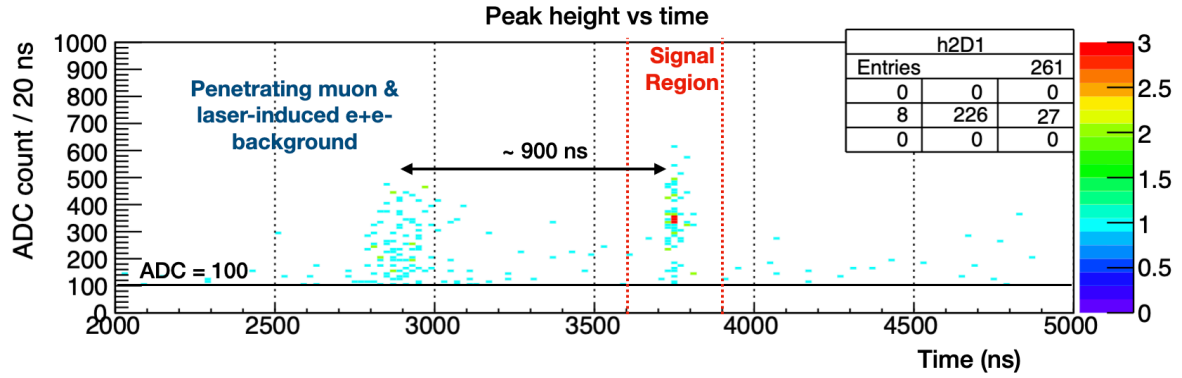

图 5.7 脉冲峰值对应的时间分布图。在时间窗口 3500 纳秒到 3800 纳秒范围内的峰形是激光电离后的热缪子信号。在脉冲高度分布图中，选择条件为大于 150 ADC 计数（对应 30 毫伏），能去除平滑的本底成分。

Figure 5.7 The distribution of pulse peak time. The peak shape in the time window 3500 ns to 3800 ns is the thermal muon signal after Mu laser ionization.

The Time of Flight (TOF) of the thermal muon signal was calculated from the meantime of the photon. The evaluation of the TOF is discussed in Section 5.3. The signal rate was calculated in the TOF selection window from 3600 ns to 3800 ns.

Figure[fig:data-bkg-comparison] compares the data taken from the laser-resonance frequency and the off-resonance frequency. When the laser is at the resonance frequency, the ionized Mu is clearly observed at the signal TOF window (3600 ns to 3800 ns), while no peak is observed when the laser is at off-resonance frequency. We successfully demonstrate the laser ionization of Mu.

5.2.3 Laser frequency de-tuning curves

The signal rate was measured under different laser frequencies, known as the laser de-tuning curve. A resonance ionization frequency gives the highest thermal muon rate of 0.135 Hz at the 244 nm laser energy of 1.8 mJ, as shown in Figure 5.9. The laser de-tuning curve measured in this study was compared with the measurement at RAL in 1999[51]. The resonance frequency in our measurement is aligned with the previous result. We obtained a higher event rate by a factor of 43. The spectral width was 51 MHz and narrower than the RAL result (97 MHz).

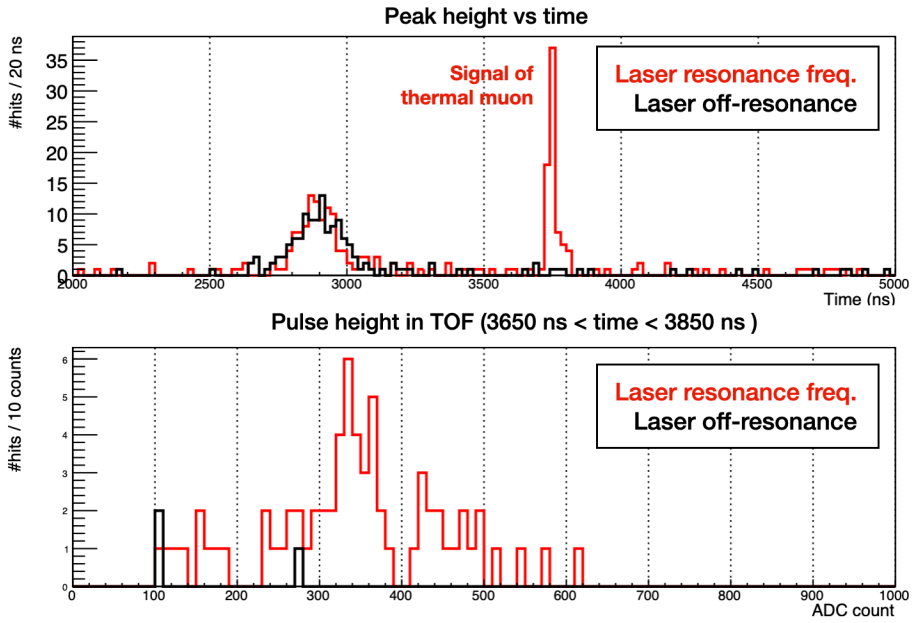

图 5.8　激光在共振频率（红色）与非共振频率（黑色）下取数的比较。在信号的时间窗口（上图）中，可以清楚看到，只有在共振频率下，发生了缪子素的激光电离，观察到了信号。在非共振频率下没有出现激光电离信号。在信号的脉冲高度分布上（指定了信号的时间窗口），可以看到经过初级选择后的信号分布，且几乎没有本底。

Figure 5.8　Comparison of data from laser at resonance frequency (red) and off-resonance frequency (black). In the time window of the signal, only at the resonant frequency, the laser ionization of the Mu signal is observed. No laser ionization peak appears at off-resonance frequencies. On the pulse height distribution (bottom), the distribution of the signal after the ADC selection can be seen with no background peak.

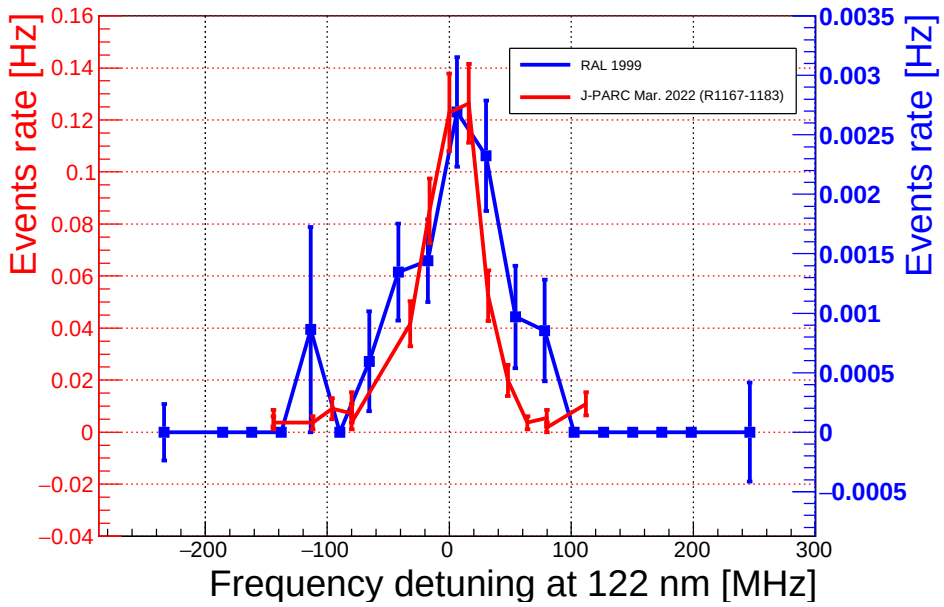

图 5.9　热缪子计数率与激光共振频率的失谐曲线。红色数据点是本实验的测量结果。蓝色数据点来自 1999 年 RAL 实验的测量结果（以往最好结果）。本实验的计数率已经超过该实验约 43 倍左右。通过归一化相同的峰值，可以得到本实验测得信号的展宽为 51 MHz，较先前结果（97 MHz）有大幅改进。

Figure 5.9　The de-tuning curve of the rate of thermal muon signal as the function of laser frequency. The blue points were from RAL 1999 result while red points was measured in this study. The signal rate is 43 times higher in this study and the signal width is improved from 97 MHz to 51 MHz.

Figure 5.10 shows the result of the high statistic data taken under two laser energies of 1.77 mJ and 1.67 mJ, respectively. The signal rate at the resonance was measured to be 0.07 and 0.028, respectively. Such rate results did not fulfill our naive expectation that the rate should be proportional to the laser power. It may be due to the laser power instability and non-ideal laser profiles. See detailed discussion in Section 5.3.3.

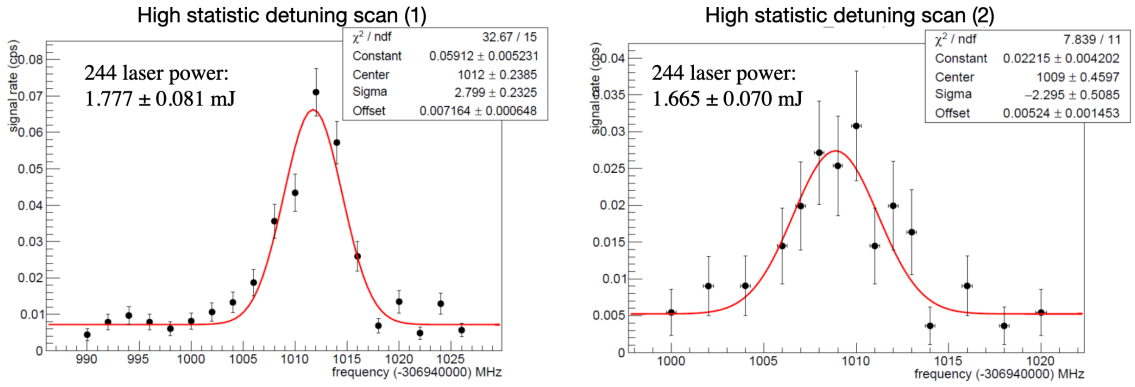

图 5.10　高通计量的热缪子信号测量结果。激光能量为 1.77 mJ（左图）与 1.67 mJ（右图）。

Figure 5.10　High statistics measurement with different laser powers of 1.77 mJ (left) and 1.67 mJ (right), respectively.

5.2.4　Parameters scan

After confirming the clear thermal muon signal, several parameters were scanned to optimize the muon signal rate. Figure 5.11 shows the scan of the laser delay time to the time origin of the RCS kicker. Delay module DG645 was used with the setting precision of 10 ns. The delay time was scanned from 500 ns to 4500 ns from the arrival of the surface muon to the S2 area. We confirmed that the best laser timing is 900 ns, which is consistent with the simulation prediction in Figure 3.11.

Figure 5.12 shows the scan of the bending magnet (MB) current from 14.5 A to 17 A. The signal rate was also highest at the nominal current of 16.25 A.

5.2.5　Measurement on laser profile

The properties of the laser profiles were measured, including the laser energy and spatial profiles. Figure 5.13 shows the result of the profile measurement at various positions along the laser path. The mean value of the laser spatial width was determined to be 2.1 mm at the center of the target chamber.

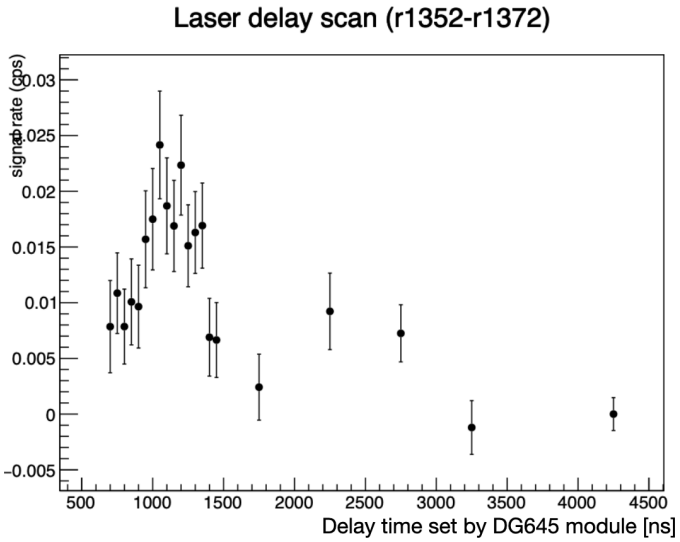

图 5.11　信号计数率随激光入射时间的变化曲线。入射时间原点被设定为表面缪子束流到达实验区域的时刻。最佳的激光入射时间确定为 900 纳秒。

Figure 5.11　Scan of the laser delay time to the arrival of the surface muon at S2 area. The best laser shooting time is determined to be 900 ns.

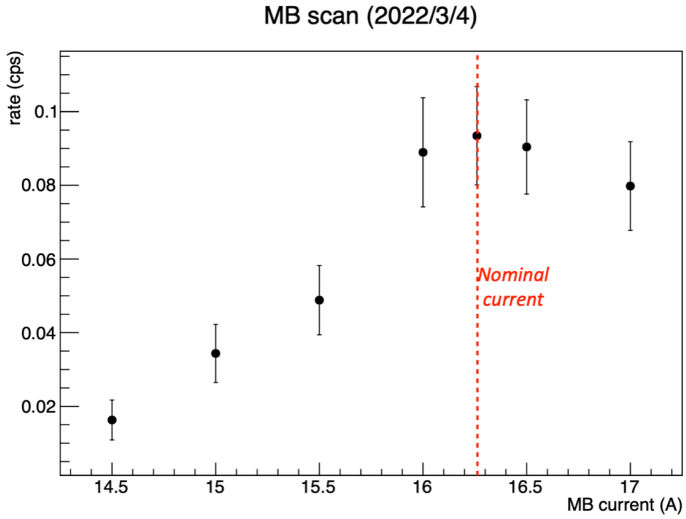

图 5.12　信号计数率随偏转磁铁的电流值的变化曲线。最佳电流值即为设定值 16.25 A。

Figure 5.12　Scan of the magnet current with nominal value of 16.25 A

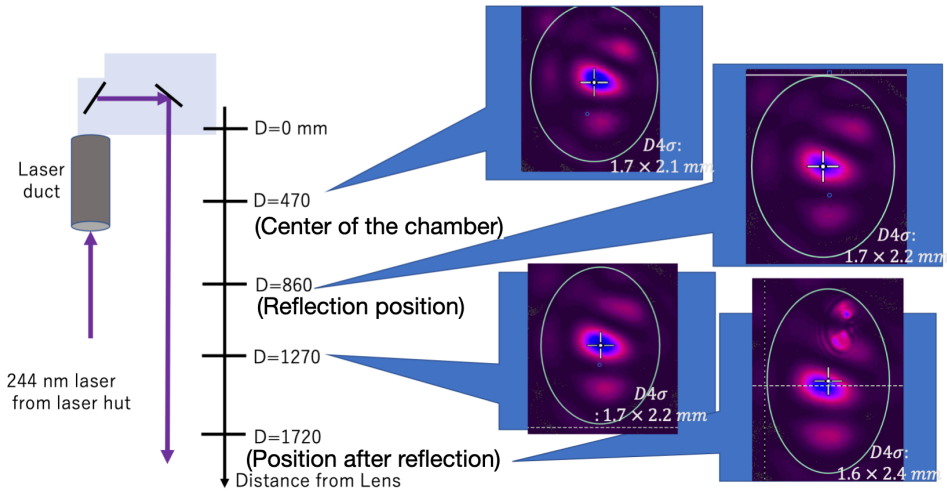

图 5.13　在不同位置上激光光束的轮廓测量结果

Figure 5.13　Laser beam profile measurement along the laser path

Due to the system's instability, the size of the beam profile is found to change from approximately 1 mm to 3 mm during data taking. The improvement in laser stability is needed for future phases.

5.3 Data analysis

5.3.1 Evaluation of TOF and event rate

To better evaluate the TOF and the event rate, high statistic data set was used in the data analysis. The laser energy ranged from 1.4 to 1.7 mJ during the data taking.

The TOF obtained in the SMBL simulation assumes the thermal muon is generated simultaneously. Therefore the real TOF in the simulation needs to consider the laser time linewidth. In Figure 5.14, the TOF from SMBL generation was convoluted with the laser linewidth; the TOF in the simulation was calculated to be 3745 ± 35 ns.

The signal from resonance laser frequency is presented in Figure 5.15. It shows the analysis of the TOF of the thermal muon signal extracted from the peak time distribution. Gaussian fitting was performed on the signal and the laser light peak to determine the mean signal time and the time origin. Measurement was also compared with the simulation prediction, which was from the Geant-4 simulation (see Chapter 3) together with the laser pulse width of 20 ns.

Simulation and measurement were normalized with the same peak height. The experimental measurement was 3742 ± 34 ns, which agrees with the simulation (3745 ± 35 ns).

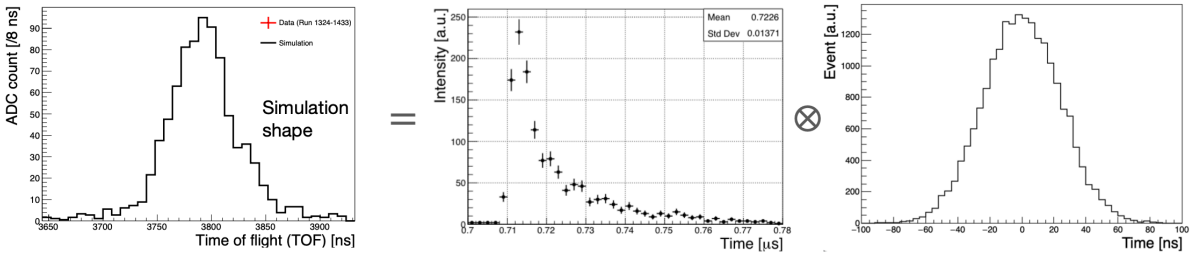

图 5.14　从 SMBL 的飞行时间（中）和激光的时间展宽（右）卷积得到模拟的飞行时间（左）。

Figure 5.14　Convolution of SMBL TOF with laser time linewidth.

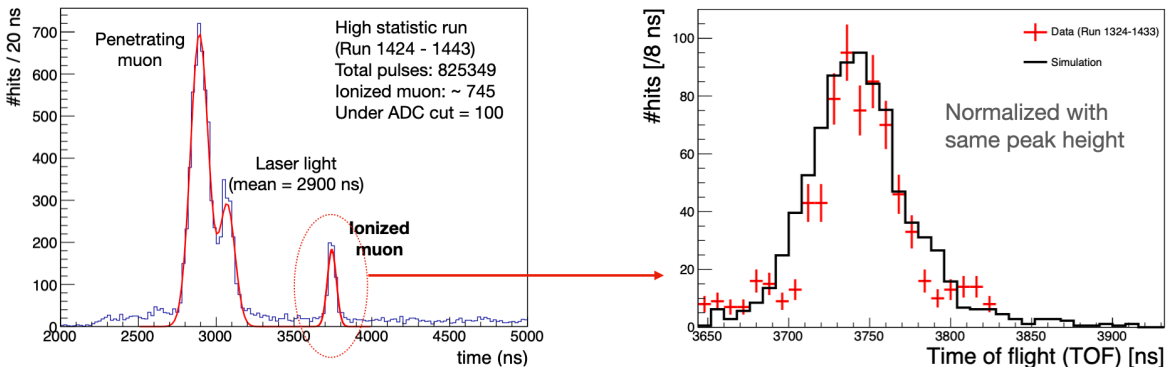

图 5.15　由脉冲峰值得到的各飞行时间谱图（左），包含入射的表面缪子、激光和慢化缪子三个峰值。热缪子信号的 TOF 分析图（右）。红色数据点为测量结果。黑色点为模拟结果。

Figure 5.15　Left: The time spectrum of TOF for penetrating muon, the laser light and the ionized muon signal. Right: the zoom-in view of the data (red), normalized with the same peak height as the simulation (black).

The same simulation events are normalized with the laser power, as shown in Figure 5.16. The measured signal rate (0.023 Hz) in this data set is lower than the simulation prediction of 0.10 Hz by a factor of 5. Several possible causes are discussed in Section 5.3.3.

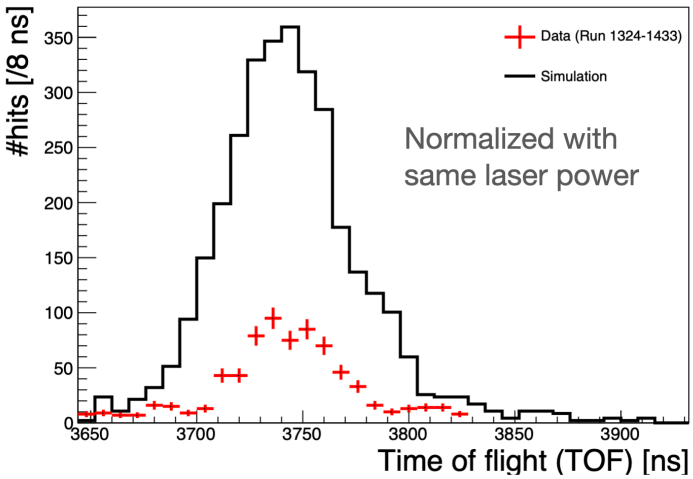

图 5.16　测量信号与模拟结果的比较图。两者根据激光能量归一化，反应了计数率之间存在差异。

Figure 5.16　Comparison of the signal with simulation result. Both are normalized with the same laser power.

5.3.2　Beam profile

At the last stage of the data taking, the beam profiles were taken by muon beam profile monitor (MBPM) at the straight end of the SMBL, as introduced in Section 2.5.5. The waveform taken from the MCP is shown in Figure 5.17. Several peak positions are observed along the time spectrum, including the penetrating muon, scattered photon, ionized thermal muon, recoil hydrogen, and ionized hydrogen. The exposure time of the MBPM is set to be a minimum of 500 ns. The result is shown in Figure 5.18 under 25000 triggers. The concentration of the beam was observed when the laser was shooting, while only flat background when the laser was off. More data are needed to analyze the beam profile in the upcoming data taking.

5.3.3　Discussion

Table 5.3 summarize the results between measurement and simulation (see Table 3.12 for simulation details). The average signal rate measured in this study is 0.023 Hz, which is lower than the simulation prediction by approximately a factor of 5. The discussion on the discrepancy is as the following.

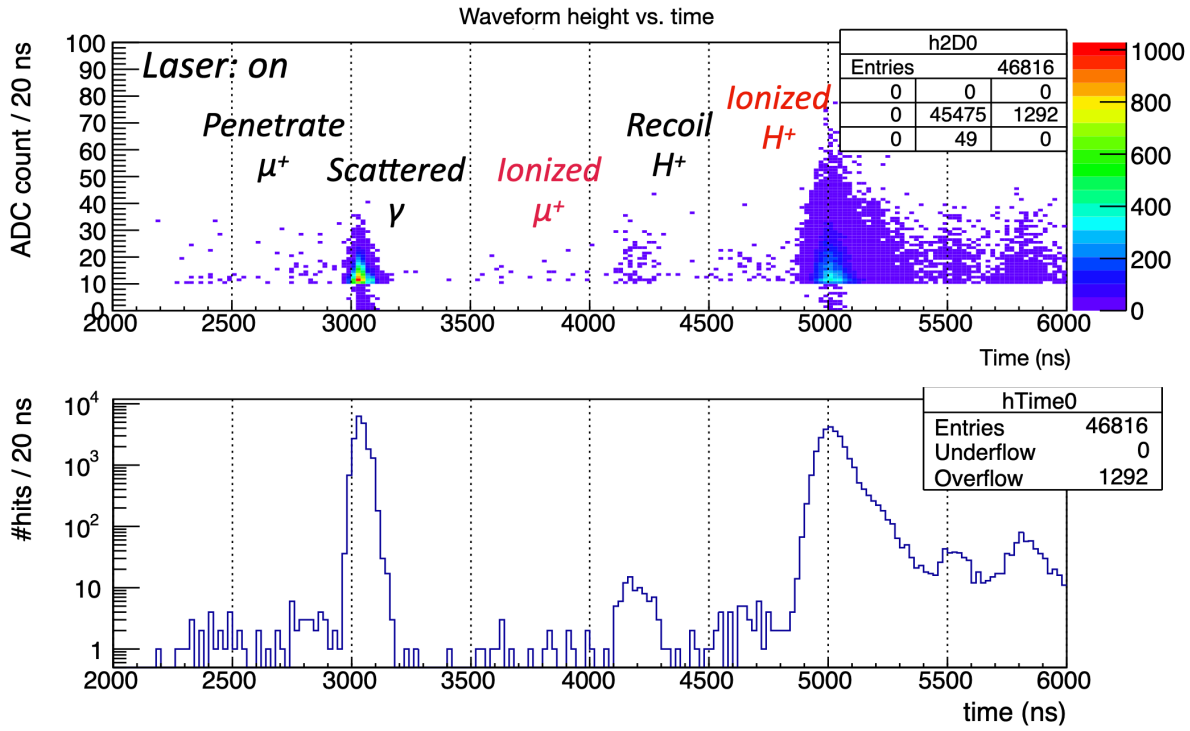

图 5.17　热缪子信号轮廓的分析示意图。在时间谱上可以观察到多个峰值。信号时间窗口选取为 3500 到 4000 纳秒。

Figure 5.17　Waveform time spectrum at the MCP. The signal time window is chosen to be 3500 to 4000 ns to match the CCD exposure time.

表 5.3　缪子激光电离实验高统计量测量结果与模拟预期对比

Table 5.3　Comparison of the muon intensity between measurement and simulation for Mu ionization experiment

	Measurement	Simulation
TOF	3742 ± 34 ns	3745 ± 35 ns
Signal rate (high statistics)	0.023 Hz	0.101 Hz

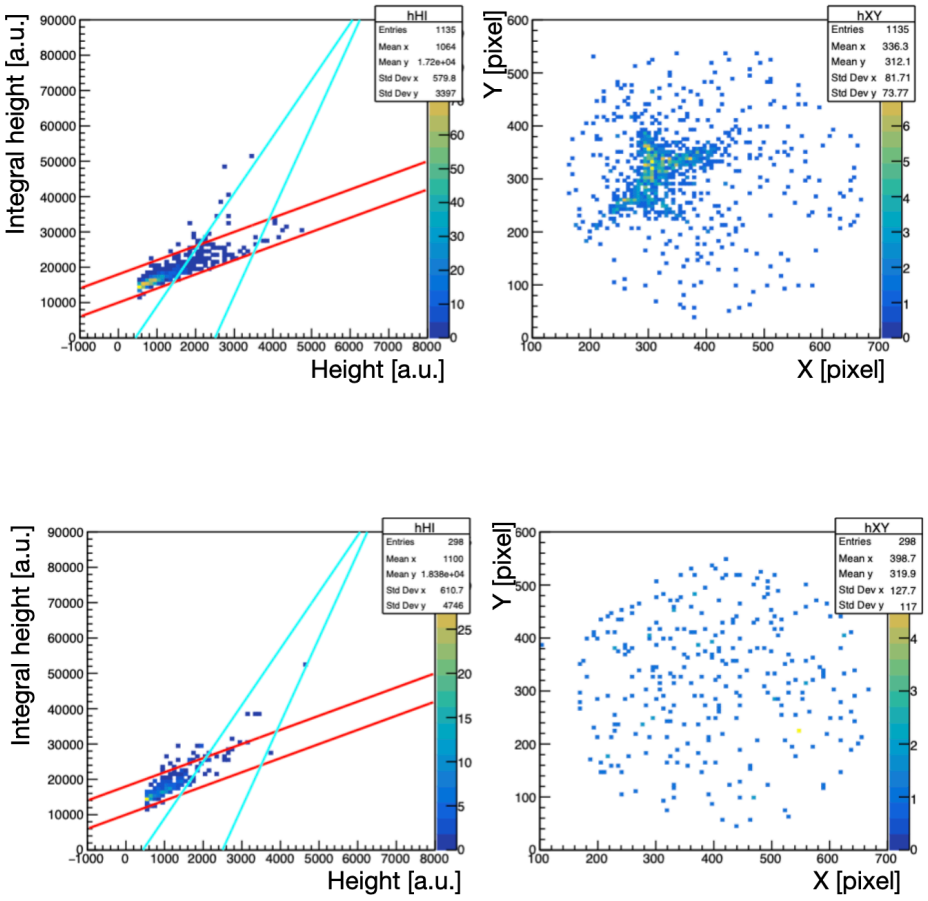

图 5.18　信号轮廓测量结果（上）与本底测量结果（下）。左图为累计脉冲高度与单像素脉冲高度的二维分布图。右图为束流轮廓在 XY 平面上的测量结果。

Figure 5.18　Measurement result of the beam profile on thermal muon signal (top) and background (laser-off). Left plots are the 2-dimensional distribution of the integral pulse height and pulse height. Right plots are the beam profile in XY plane.

- It was found that the **stability of the laser energy** during each data-taking run had large systematic uncertainties. The signal rate evolves from 0.14 Hz in Figure 5.9 to 0.7 Hz in Figure 5.10 with unstable laser energy. It can be improved with a high-quality Barium borate (BBO) crystal used in the amplifier at the first stage. Since ionization is a three-photon process, the laser ionization efficiency is proportional to more than the square of the laser power. Figure 5.19 shows the ionization efficiency under two laser powers. One of the possible solutions in the future is to synchronize the laser power with the data taking. The signal rate is calibrated with the laser power to reduce the effect of laser instability.
- **The alignment of the laser to the surface of the target** is another relatively sizeable systematic uncertainty. The position of the laser was not precisely determined during the data taking. The fluctuation was estimated to be several millimeters. As illustrated in Figure 5.20, different laser center position causes a decrease in the ionization efficiency. It can contribute to the current discrepancy between the measured signal rate and simulation prediction.
- **The laser wavelength** was not measured precisely in this data taking. Frequency accuracy was determined by wavelength meter, which was not calibrated by an Rb-locked laser. The frequency before calibration fluctuates ±0.4 MHz peak-to-peak (0.2 MHz std. deviation). A shot-by-shot measurement fluctuation of WS7-60 would cause this fluctuation. The absolute accuracy of less than 1 MHz is expected in future data taking.

Further improvements are needed towards the high-quality laser beam, and high statistic data-taking is expected to solve current issues on the signal rate.

5.4 Summary on Mu ionization experiment

For the first time, we successfully observed the thermal muon signal from ionization of Mu generated from silica aerogel. The signal rate has been evaluated, and a good agreement on TOF has been achieved between simulation and the measurement. Table 5.4 summarize measurement results obtained in our experiment with the expectations. Improvements by a factor of 43 in thermal muon generation have been achieved with 244 nm laser energy of several mJ.

The measured rate on the first run was consistent with the simulation prediction. The rate of high statistical run afterward was only approximately one-fifth of the simulation pre-

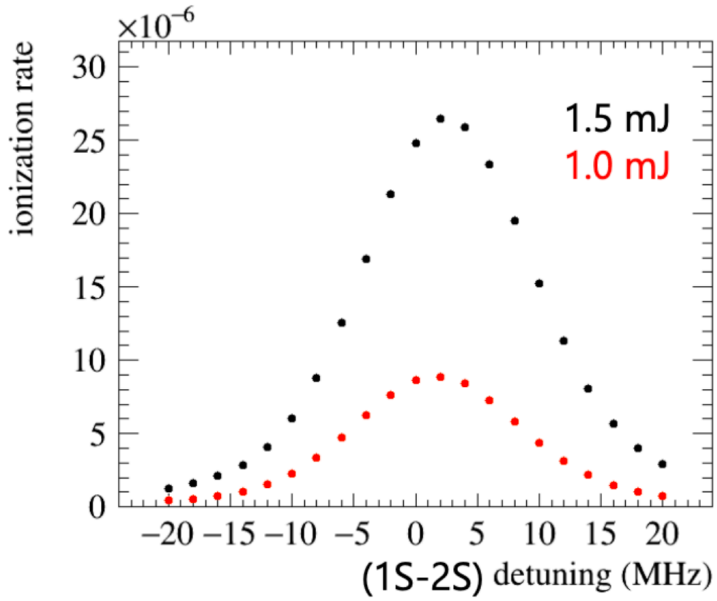

图 5.19　激光能量与电离效率之间的关系。红色点代表激光能量为 1.0 mJ 的情况，黑色代表激光能量位 1.5 mJ 的情况。

Figure 5.19　Laser ionization rate as the function of the frequency. Points in red color is under the laser power of 1.0 mJ while back points is under the laser power of 1.5 mJ.

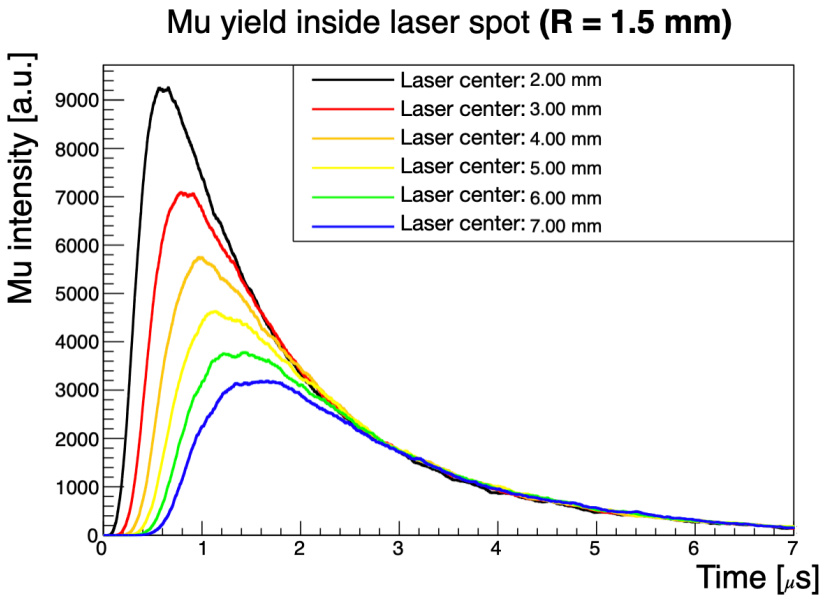

图 5.20　缪子素在激光照射区域内的数目随着时间的演变。不同的颜色曲线代表不同的激光中心位置（到靶材料下游表面的距离）。

Figure 5.20　Mu evolution inside the laser irradiating area. Different colors represents the different laser center position from the downstream surface of the target.

表 5.4 缪子激光电离实验总结表

Table 5.4 Summary of the first phase in Mu ionization experiment

Measurements	Measurement result	Prediction
Signal Rate	0.13 ± 0.01 Hz	0.101 ± 0.002 Hz
	0.023 ± 0.001 Hz	
TOF	842 ± 34 ns	845 ± 35 ns
Laser resonance frequency	306 941 007 ± 49.8 MHz	306 940 993.9 ± 96.9 MHz
Optimal laser shooting time	900 ± 100 ns	910 ± 10 ns

diction. The discrepancy between the measurement and the simulation has been discussed in Section 5.3.3, including the laser instabilities and the improvement in the frequency calibration.

Upcoming data taking with a high-quality and higher energy laser beam is under preparation for precise measurement and the final confirmation on the consistency with the simulation.

6 A Novel Design of Multi-layer Target for Thermal Muon Generation

This chapter discusses an independent work towards the higher intensity of the thermal muon for the E34 experiment. The generation of thermal muons by laser ionization of Mu confined in multi-layer silica aerogel structures was proposed with modeling and simulation. In this design, thermal Mu generated inside the multi-layer silica aerogel can be emitted into the sandwiched vacuum regions separated by a few millimeters between targets. The efficiency of thermal muon generation in this configuration is studied with laser ionization simulation.

Mu emission at E34 configurations (H-line) is firstly introduced in Section 6.1. The scheme of the multi-layer design is introduced in Section 6.2, together with the extension of the diffusion model to the Mu confinement and the laser ionization simulation. The enhancement result of the Mu emission and thermal muon after ionization is presented in Section 6.3. A scheme of validation experiment is proposed in Section 6.4.

6.1 Mu emission at E34 configurations

This section summarizes the Mu emission for the E34 experiment with J-PARC H-line configurations. The basic scheme and the details of the diffusion model were discussed in Chapter 3. In this section, the simulation tools are continuously used. Instead of the S-line beam structure, the difference in previous results is highlighted in the following.

Figure 6.1 shows the stopping distribution of the aerogel target with a thickness of 7.12 mm in the beam (Z) direction. Unlike the S-line stopping simulation in Figure 3.7, the stopping distribution at H-line shows a vast and nearly uniform spread along the beam direction, which is due to the difference in the muon extraction schemes between S-line (bending magnet) and H-line (solenoid) at the upstream proton target. For S-line, it selects muon's momentum strictly, while H-line covers a wide range of muon momentums and gives higher muon intensity.

The spatial distributions are shown in Figure 6.2. It is due to the initial surface muon distribution at the muon target. After the diffusion model, only the Mu that stopped within approximately 2 mm from the downstream surface of the aerogel emits out while most of the stopped surface muon is wasted.

The laser region designed for the E34 experiment along beam direction is set from 1 mm

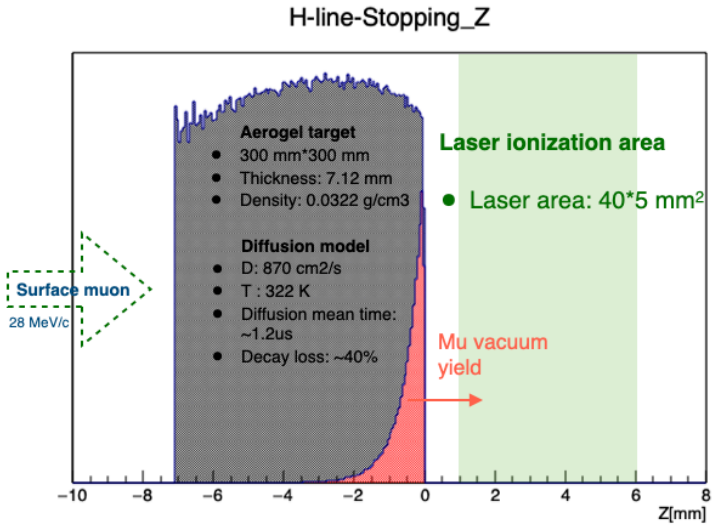

图 6.1　利用 H-line 表面束流性质模拟得到的缪子在硅凝胶内的停止分布（灰色）以及能溢出到真空中的缪子分布（红色）。由于 H-line 的束流动量展宽大，停止分布与第三章图 3.7不同。激光照射区域也不再是半径为 3 毫米的小光斑，而是分布在 40×5 mm^2 的矩形区域。

Figure 6.1　The stopping distribution of the surface muon inside the aerogel. The gray color shows the total stopping distribution of the surface muon and the light red color shows the initial position of the Mu who could emit out into the downstream vacuum. H-line has large beam mometum spread, which yield different stopping feature than S-line in Figure 3.7. Laser ionization area was also defined as 40×5mm^2 in Y and Z direction, respectively.

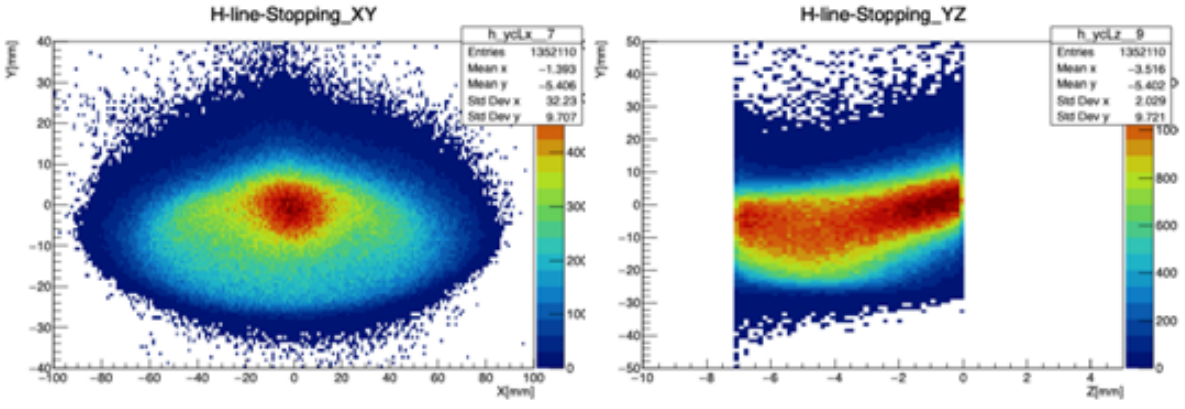

图 6.2　缪子在硅凝胶内停止位置的空间分布。左图为 XY 方向，右图为 ZY 方向。

Figure 6.2　Spatial distributions of the stopping muon inside the aerogel.

to 6 mm away from the downstream surface of the aerogel. After emitting from the surface, Mu goes straight into the vacuum, possessing its initial velocity. The number of Mu inside the laser region is counted at different times. The best laser-shooting time is 0.9 μs with a maximum Mu yield in the H-line case.

Figure 6.3 shows the number of the Mu inside the laser region and the distribution of the Mu inside the laser region at the laser shooting time, which is regarded as the ionized thermal muon. The density of the Mu at the laser shooting time exhibits uniform over the laser irradiative region. Therefore the 122 nm laser power is not recommended to be uniformly distributed.

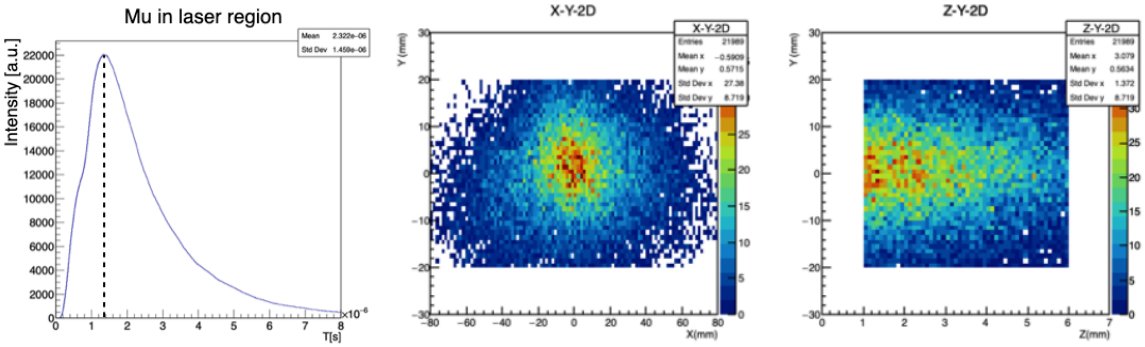

图 6.3 左：缪子素在真空中的激光电离区域内的数量随着时间变化，最佳的激光照射时间可得为 0.9 μs。中图和右图为电离后的热缪子的空间分布（XY 平面和 ZY 平面）。

Figure 6.3 The number of the Mu inside the laser region (left). The best laser-shooting of 0.9 μs could be determined. The distribution of the Mu inside the laser region at the laser shooting time could be regarded as the ionized thermal muon (middle and right).

6.2 Design of the multi-layer target

We present a novel design of multi-layer laser-ablated silica aerogel target, as shown in Figure 6.4. In this design, a series of aerogel targets are aligned horizontally in parallel. Mu is emitted from the upper and lower laser-ablated surfaces of silica aerogel targets. Thermal Mu motions in the narrow vacuum regions between the targets. The pulsed laser is timed to overlap the maximum density of Mu in a vacuum to generate a thermal muon, same as in the strategy for Mu 1S-2S experiment. The meshes at both ends of the aerogel targets provide an electric field in the same direction as the incident surface muon to extract the thermal muon.

In this scheme, the Mu events are confined in those different layers of the vacuum regions, and the density of the Mu increases in the laser-irradiative vacuum. It is necessary to consider Mu's interaction with the surface of the aerogel in addition to Mu's diffusion process.

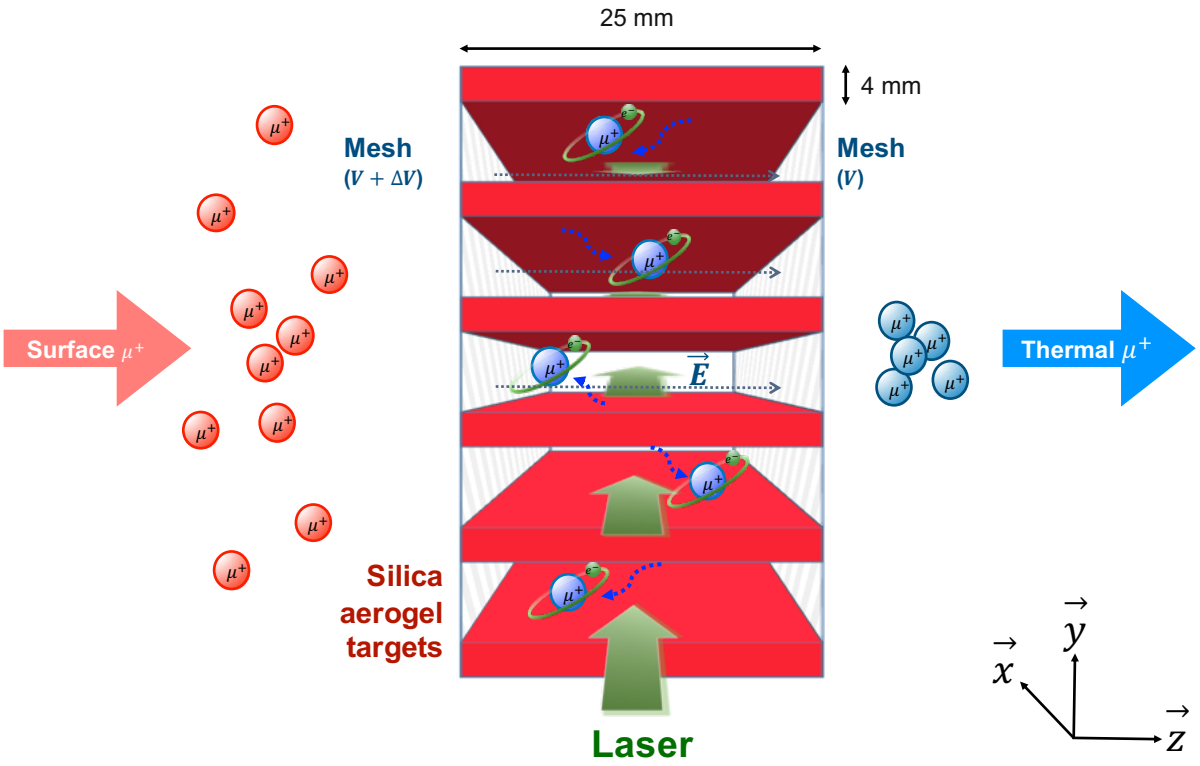

图 6.4　多层靶的概念设计示意图

Figure 6.4　The schematic drawing of the multi-layer aerogel targets proposed in this study.

6.2.1 Muonium confinement in the multi-layer target

Mu under thermal energy (0.02 eV) has a typical velocity of approximately 7 mm/μs at room temperature. If the aerogel slots in the multi-layer target are separated by a few millimeters, Mu can re-encounter the surface of the aerogel within their lifetime.

Such a feature was considered into the diffusion model, as shown in Figure 6.5. Mu is traced in the vacuum. Once the track crosses the surface of the aerogel, the diffusion process starts again until its position scratches the surface into the void within its lifetime or decays inside the aerogel. In this process, Mu is neither 100% elastically reflected from the surface nor completely absorbed by decay in the aerogel. Some Mu is ultimately accumulated in the vacuum region between the aerogel slots. The number of the confined Mu depends on the interval between the aerogel targets.

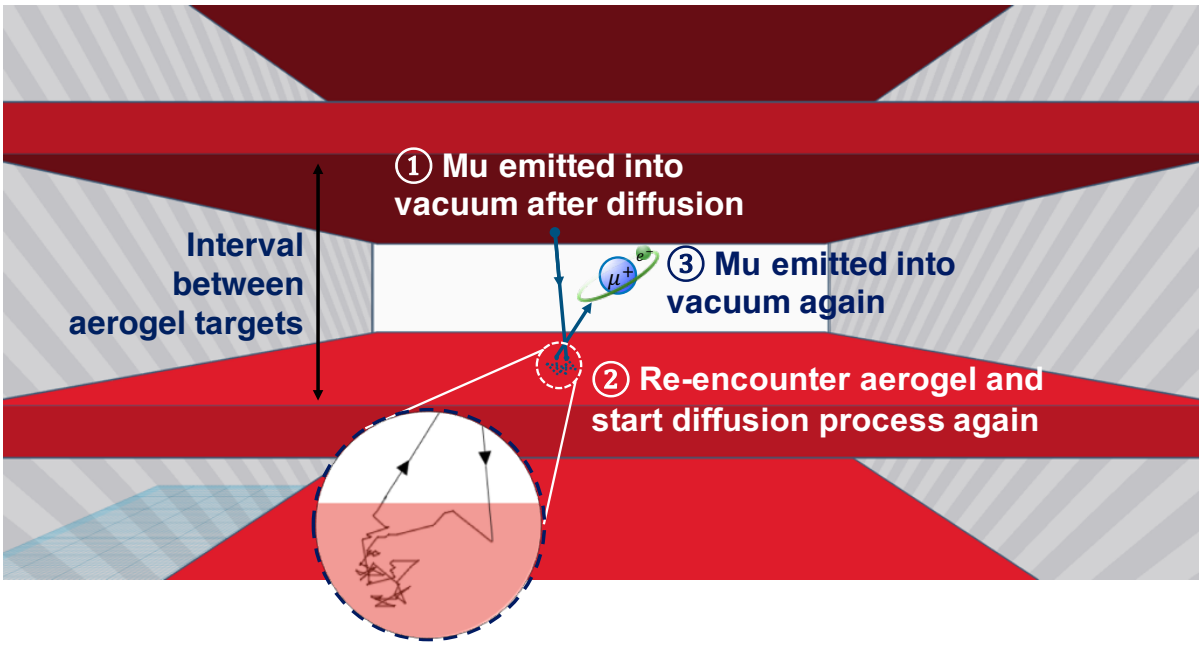

图 6.5 缪子素在硅凝胶表面上的反射过程示意图。从真空中重新接触到硅凝胶表面的缪子素会再次经历扩散过程，并有一定几率重新溢出到真空中。

Figure 6.5 The schematic drawing of the modeling of muonium reflection in the boundary of aerogel and the vacuum.

Figure 6.6 shows the spectra of Mu yield result on several models: the red line was Mu yield from the diffusion model in this study, the green color was from the elastic (direct) reflection and the blue was from absorption (Mu was completed absorbed once re-encounter aerogel). The direct reflections enhance the yield further, fulfilling our naive expectations.

Using our model instead, we have made a conservative estimate of the yields. Since silica aerogel is the material with nanoporous structures. We believe our model is more suitable than direct reflection.

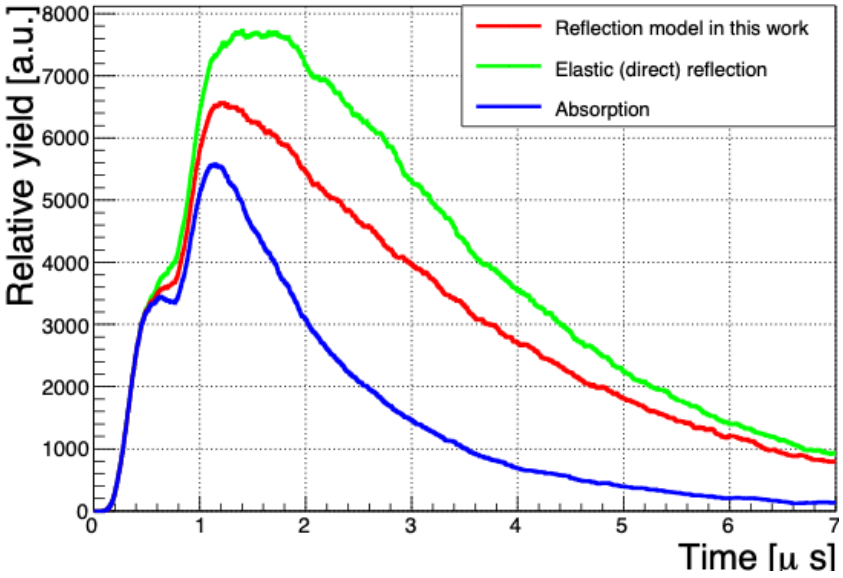

图 6.6　不同的缪子素在硅凝胶表面反射方式的假设：红色曲线表示在本工作中采用的扩散模型的扩展；绿色曲线假设缪子素在表面弹性反射；蓝色曲线假设缪子素在表面被完全吸收。本工作中采用的模型给出的结果介于两个极端假设之间。

Figure 6.6　The results of various models assumed for the Mu yield: green curve is from the diffusion model assumed in our study; green color assumes direct reflection of Mu on the aerogel surface and blue color assumes complete absorption.

6.2.2　Laser ionization of muonium

The laser ionization process was developed as the final stage of the model to derive the ionization probability of the Mu irradiated by a laser in the vacuum. The model utilizes the rate equations[61, 73] to describe the excitation and ionization of each Mu in a vacuum. A layer of 122 nm wavelength is utilized to excite Mu from 1S to 2P state, and another layer of 355 nm wavelength is used to ionize the excited Mu. Combining the model of Mu motion and the laser ionization, thermal muon is generated. The efficiency of the thermal muon per surface muon can be evaluated by developing an end-to-end simulation of the model.

6.3 Simulation result of multi-target design

6.3.1 Simulation setups

A Monte-Carlo program was developed to simulate the multi-layer design. The upstream configurations of the J-PARC H-line surface muon beam are the same as that used for the single-layer design[31]. 2×10^7 surface muons were simulated upstream, and six aerogel targets were set in the multi-layer design. In the single-layer design, the aerogel has a thickness of 7.12 mm, and lengths of 100 mm in the y direction and 100 mm in the x direction, respectively. The laser-irradiation region is 1 mm and 6 mm in z direction from the aerogel surface. In contrast, in the case of multi-layer design, aerogel thickness is 4 mm, and the length is 25 mm in the z direction and 100 mm in the x direction. Each laser-irradiation excludes 1 mm from both the upper and lower aerogel surfaces. The width of the laser in the horizontal direction was set to cover from 0 mm to 25 mm from the upstream edge of the aerogel target.

The pulse laser of 122 nm wavelength was linearly polarized. Gaussian profiles were assumed for the intensity's frequency, timing, and space domains, while the laser outside the defined laser irradiating regions is blocked. The bandwidth of the 122 nm and 355 nm laser was 50 GHz (FWHM), and the time duration was 2 ns. An algorithm was developed in the simulation to optimize the laser configurations, including the laser-shooting time, the position of the laser center, and the distribution of the 122 nm and 355 nm laser pulse energy in each region. For example, the laser irradiation area has been chosen to maximize the number of Mu in the range of 0 to 5×125 mm^2 for the case of an interval of 7 mm in the multi-layer design.

6.3.2 Results of the Mu emission

Figure 6.7 shows the distribution of the stopping position of the surface muon along the beam and the vertical directions. The aerogel thickness in the single-layer case was 7 mm to stop 41.8% of the total surface muons. Because the muon beam had a wide momentum spread, the stopping distribution was nearly flat along the beam direction. In a multi-layer design, although approximately half of the surface muons penetrated the vacuum through the interval of aerogel, the thickness of the aerogel target along the beam direction was set to 25 mm to maximize the number of stopping surface muons. The overall efficiency of the surface muon stopping was 0.454, which was slightly higher than that of single-layer muons.

Figure 6.8 shows the comparison of the distribution of the Mu vacuum yield at 0.60 μs (left) and 0.95 μs (right) after the average time of arrival of the two surface muon pulses. In the single-layer design, Mu is emitted into the vacuum from only one surface (Z = 0 mm). In

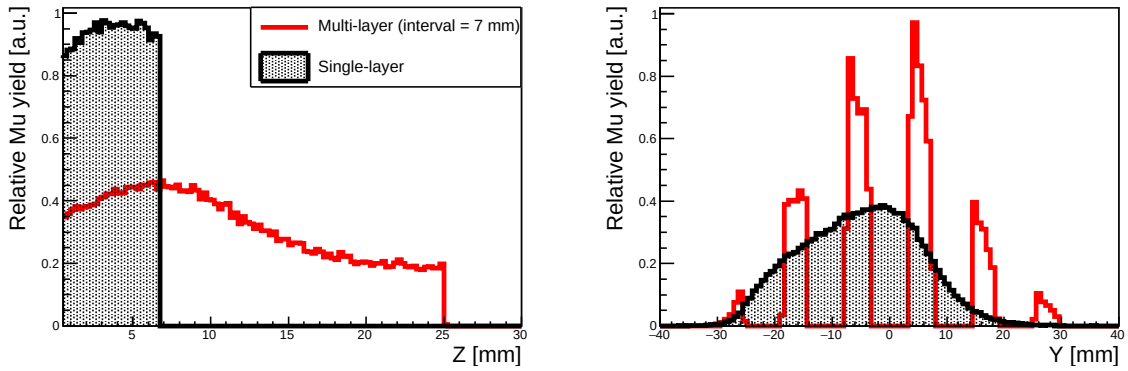

图 6.7　硅凝胶内表面缪子沿光束方向（z）和垂直方向（y）的停止分布图。黑色阴影直方图为单层靶设计，红色为多层靶。坐标系遵循图 6.4。

Figure 6.7　The stopping distribution of the surface muon inside the aerogel along the beam direction (z) and the vertical direction (y), for the single-layer design (black-shaded histogram) and the multi-layer design (red). The coordinate system follows the same design as in the Figure 6.4.

contrast, Mu is emitted from two surfaces in each sandwiched vacuum region in the multi-layer structure. The distribution in the central region is shown in the figure when the surfaces are at $Y = -3.5$ mm and $Y = 3.5$ mm. The area of an aerogel facing the emission surface is 100 cm^2 for the single-layer and 25 cm^2 for the multi-layer (2×25 cm^2 for two surfaces). At 0.60 μs, the two surfaces in the multi-layer design exhibit approximately double the Mu emission compared to the single-layer design. At 0.95 μs, the multi-layer distribution becomes more uniform, which is a convolution of the Mu from the original emission from two surfaces and the re-emitted Mu after encountering the aerogel surface on the opposite side. The latter contributes to 8.4% of the total emission, as predicted by the simulation. In total, 5 vacuum regions were available, but the non-center regions received fewer events from fewer stopping surface muons (see Figure 6.7). The efficiency of the Mu vacuum yield in the multi-layer design (0.179) is determined to be approximately 3 times higher than that of the single-layer design (0.058), including the Mu decay loss during the diffusion process.

Figure 6.9 shows the time evolution of the number of Mu inside the laser irradiation region under the single-layer and the multi-layer designs. The double pulses of the surface muon beam create a step-like time structure at the leading edge. The optimal laser-shooting times are 0.95 μs and 1.05 μs after the average arrival time of the surface muon for single-layer and multi-layers, respectively. The maximum number of Mu is about 3.45 times higher in the

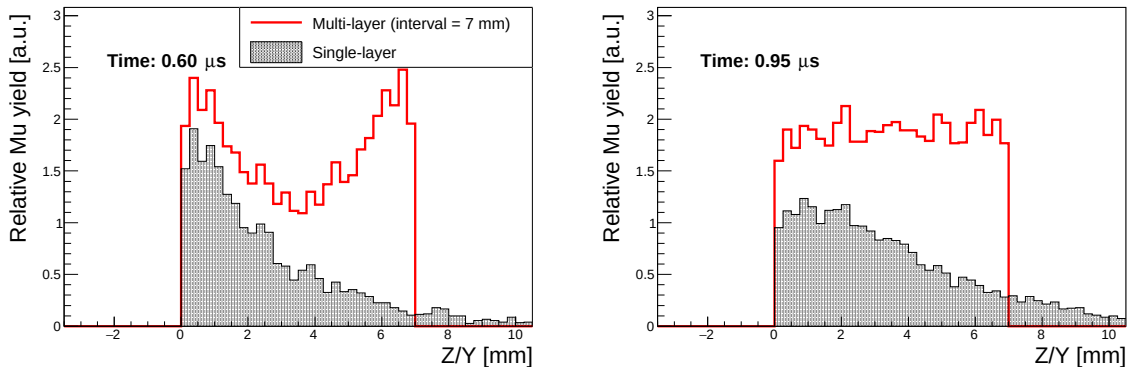

图 6.8 真空中的缪子素在 0.6 μs（左）和 0.95 μs（右）的分布。对于单层靶设计（黑色），水平轴为 z 方向，而对于多层靶，水平轴为 y 方向。两者可沿垂直于发射表面的方向进行比较。（在多层靶中，y 方向的范围应为 −3.5 mm < y < 3.5 mm，在此图中移动了 +3.5 mm）。图中单层靶和多层靶的缪子数量使用相同的表面缪子入射数目进行归一化。

Figure 6.8 Distributions of the Mu position in vacuum at 0.6 μs (left) and at 0.95 μs (right) after the arrival of surface muon pulses. The horizontal axis is in z direction for the single-layer design, while in y direction for the center region of multi-layer so that they are compared along the direction perpendicular to the emission surface. (originally, −3.5 mm < y < 3.5 mm, shifted by +3.5 mm in this figure). Mu emissions in the single-layer and multi-layer designs are normalized with the same incident surface muons.

multi-layers design than in the single-layer design.

As a result, Figure 6.10 shows the results of the Mu emission as the function of intervals. An interval of 7 mm provides the most significant number of Mu inside the laser irradiation region due to a combination of factors. When the gap is smaller, the number of Mu yields in a vacuum increases as the targets are closer to the beam center. However, the spatial constraints of the laser region limit the total irradiated Mu. When the interval is more significant than 7 mm, the fewer stopping muons largely contribute to the loss.

Table 6.1 summarize the thermal Mu generation efficiency between the single-layer design and an example of the multi-layer structure, which has an aerogel thickness of 4 mm and is separated by a 7 mm interval. The total efficiency is enhanced by 3.4 times under the multi-layer case.

6.3.3 Results of the thermal muon generation

The thermal muons from laser ionizations are calculated for various laser pulse energies. The number of Mu was combined with its laser ionization probability from the simulation at different multi-layer intervals.

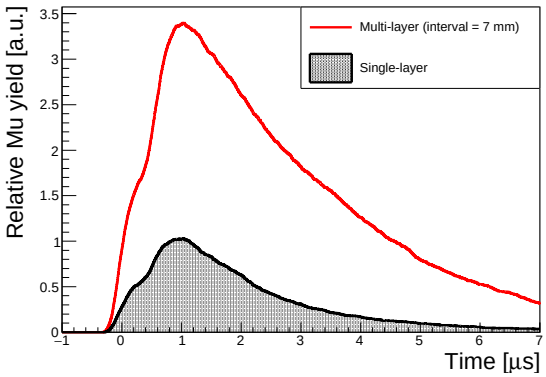

图 6.9　真空中缪子素数目随时间的演变。黑色为单层靶，红色为多层靶。缪子素的数量被归一化为单层设计中的最大的缪子素数量。时间原点设置在表面缪子双脉冲的中间。

Figure 6.9　The evolution of Mu into the laser ionization region after emission into vacuum for the single-layer and multi-layer design. The number of Mu is normalized to the maximum Mu emission from the single-layer design. The time origin was set at the middle of the double pulses of the surface muons.

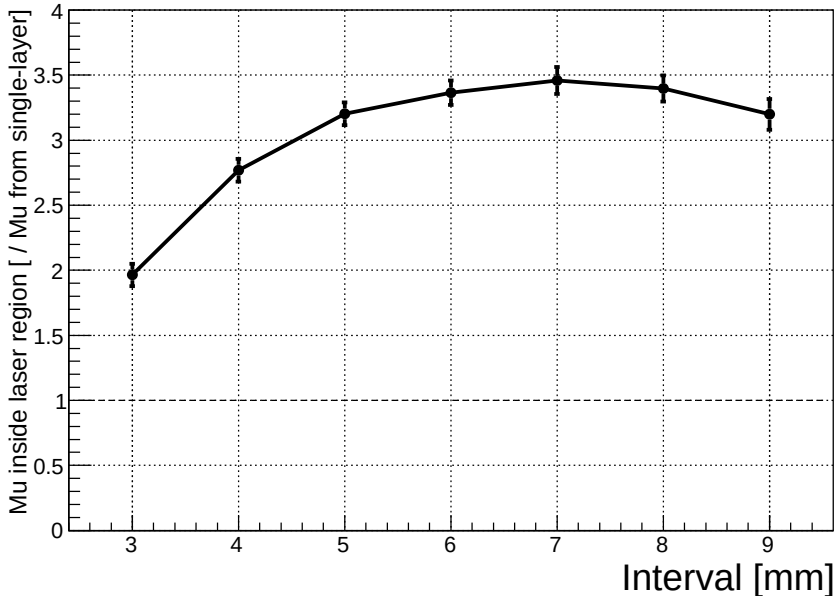

图 6.10　不同的靶间隔下，在最佳的激光发射时间时得到的缪子偶数数量。缪子素的数量被归一化为单层靶的缪子素数量。在多层靶中，最大值出现在间距为 7 毫米处，并且是单层靶的 3.4 倍左右

Figure 6.10　The maximum Mu yield in the laser region under different intervals at their optimal laser shooting time. The number of Mu is normalized to the Mu emission from the single-layer design.

表 6.1 单层靶和多层靶产生的的缪子素细分效率比较表

Table 6.1 Comparison of the efficiency of thermal Mu production between the single-layer design and the multi-layer design in simulations

Stages	Efficiency (single-layer)	Efficiency (6 layers, thickness of 4 mm, interval of 7 mm)
Surface muon stopping in the aerogel	0.418	0.454
Mu formation	0.52	0.52
Mu vacuum yield	0.058	0.179
Mu irradiated by laser	0.264	0.283
Total efficiency	0.0034	0.012

Figure 6.11 shows the calculation strategy. The efficiency of the laser scales the number of Mu. The total laser power to obtain the ionized thermal muon is under two laser powers: 355 nm laser power of 0.15 J/cm^2 or 1.2 J/cm^2. The maximum Mu yield corresponds to an interval of 4 mm.

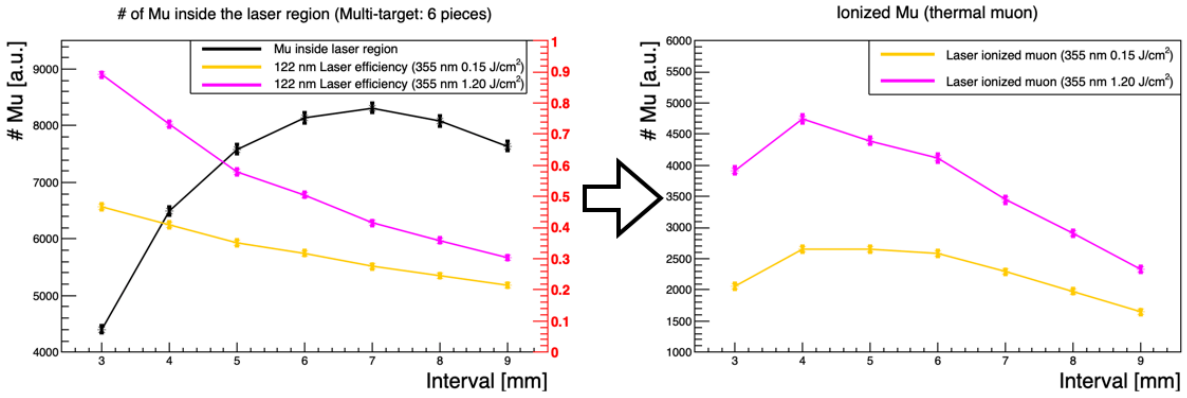

图 6.11 通过结合缪子素数量（左图黑色曲线）和激光电离效率（左图紫色和黄色曲线）计算出电离后的热缪子数（右图曲线）。

Figure 6.11 Calculation of the thermal muon by combining Mu emission and laser ionization efficiency.

Figure 6.12 considers the case of a 122 nm laser with an energy of 100 μJ and a 355 nm laser of energy 300 mJ[31]. The number of thermal muons is maximum at an interval of 3 mm under the energy mentioned above and 2.45 times higher than that of the single-layer design. If the interval is increased, the laser energy per irradiating area has to be reduced, and this causes the ionization efficiency to drop significantly. When the laser energy increases, the

larger interval (and the irradiating area) performs better because the absolute Mu in the laser region rises. For a 122 nm laser with an energy of 100 μJ and a 355 nm laser with a power of 1.5 J total, the number of thermal muons is maximized at a 4 mm interval, where the yield is enhanced by a factor of 3.4 than the single-layer design. For a 122 nm laser with an energy of 500 μJ, the maximum output is improved by a factor of 5.2 at 5 mm. In the extreme case, when the laser energy is high enough to ionize Mu for all intervals fully, the tendency of thermal muon yield is close to that of Mu.

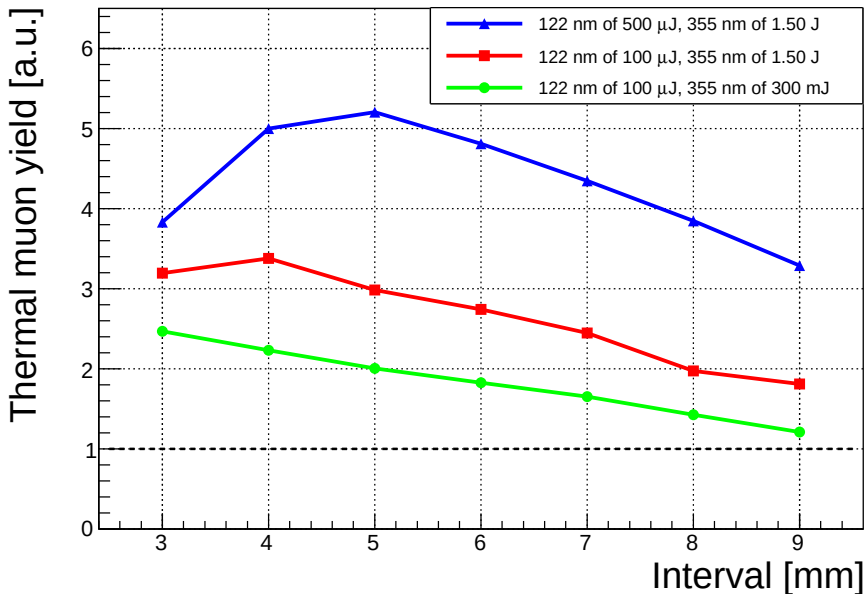

图 6.12　不同多层靶间隔下缪子素激光电离产生热缪子的结果。图6.10中 Mu 数目用不同激光能量配置下的激光电离效率计算出热缪子数。热缪子产率也归一化为单层设计的产率。

Figure 6.12　The results of thermal muon generation from laser ionization of Mu under different intervals. The numbers of Mu in Figure 6.10 was calculated with the laser ionization efficiency under different laser energy configurations. The thermal muon yield is also normalized to that of the single-layer design.

6.3.4　Possible improvement

Further improvements are possible toward even higher thermal muon generation by making the thickness of the aerogel smaller in the multi-layer design. We recall that the initial stopping position of the Mu, which is emitted in a vacuum, follows the exponential distribution with the characteristic depth for the diffusion of 0.43 mm. With smaller thicknesses, more aerogel layers are possible to set.

Moreover, the hybrid geometry design consisting of the single-layer upstream facing the surface muon and several multi-layer aerogel targets downstream gives the additional enhancement of the thermal muon intensity.

We consider an application where the thermal muon from Mu laser ionization is accelerated by the electrical lens to 5.62 keV, followed by conventional RF cavities[31]. We studied the initial acceleration of the thermal muon generated at the multi-layer target and found that the small emittance of the beam and the transport efficiency (0.74) were preserved. On the other hand, the large initial beam spatial spread along the beam acceleration direction (5 mm in the single-layer while about 25 mm in the multi-layer) causes additional concern: the spread of the kinetic energy would increase by using the same the E-field as in the single-layer, as illustrated in Figure 6.13, while the spread of time would increase if using the reduced E-field. The balance between the energy and the time width should be studied for the practical application of the multi-layer design.

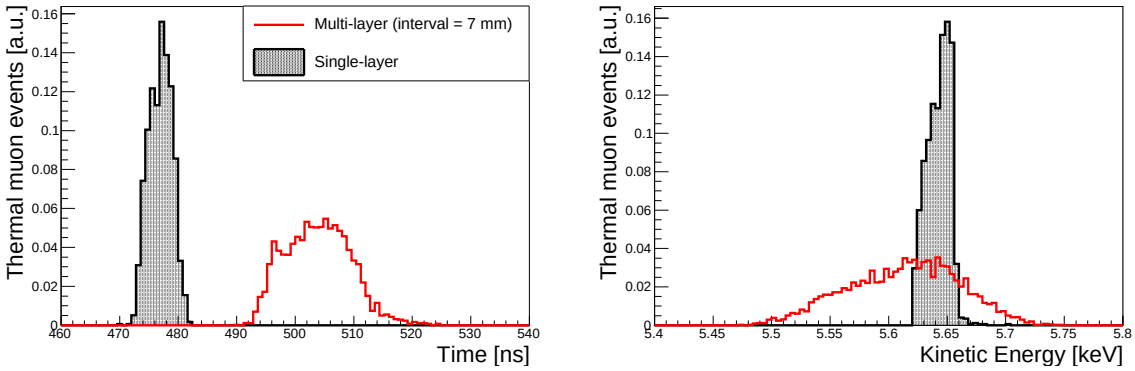

图 6.13 单层设计和多层设计中静电场（SOA）加速的热缪子的时间（左）和能量（右）分布。在多层靶设计中，电场设置为与单层靶设计相同。每个分布都归一化为单位面积。

Figure 6.13 Time (left) and energy (right) distributions of thermal muon extracted by static-electrical field from single-layer design and multi-layer design. In the multi-layer design, the time E-field was set to be the same as that of single-layer design. Each distribution is normalized to unit area.

6.4 Validation on the reflection effect in the multi-layer design

A validation experiment was designed on the reflection process in the multi-layer design before constructing the full version of the multi-targets.

Figure 6.14 shows the schematic drawing of the validation experiment. In this simplified scheme, only two aerogel targets are created. Considering the realistic development of the

laser system, the 244 nm laser with a beam waist of about 1.5 mm is expected. Such a small laser spot will be inside the vacuum with an interval of about 4 mm (and adjustable in later optimization).

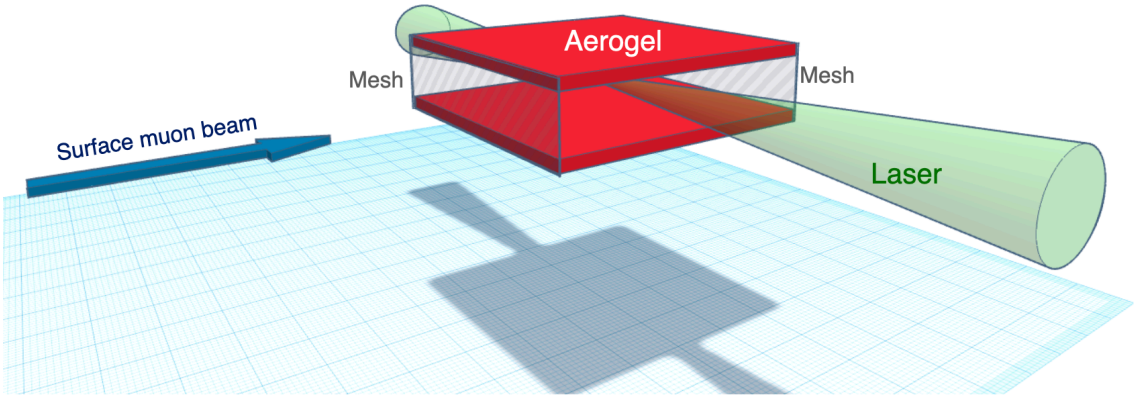

图 6.14　多层靶概念的验证性实验示意图。在此设计中，只用两层硅凝胶靶来验证缪子素在硅凝胶表面的反射过程。

Figure 6.14　The scheme of the validation experiment. Only two pieces of the aerogel are needed.

Under such a scheme, we discuss two methods to perform the measurement in Section 6.4.1 and Section 6.4.2.

6.4.1　Scan of the laser position

In this method, the laser spot is scanned along the $\vec{z}$ direction (the beam direction) from one end of the aerogel to the other. The range of the aerogel is designed to be 25 mm in length. For each position, the number of the ionized Mu from the two pieces is counted by the SMBL.

Figure 6.16 shows the comparison of the Mu emission evolution curve with the reflection model and without the reflection model. The reflection model helps to keep more Mu inside the laser region for a longer time. Such curves are simulated from $Z = 3$ mm to $Z = 23$ mm.

In summing up all the curves, it was found that the collection of curves without the reflection model shows similar shapes and tendencies. In contrast, the collection of curves with the reflection shows the deviation from each other. Such a feature is further quantitatively shown in Figure 6.16. The optimal laser time shooting time obtained from each curve is plotted as the function of the position. Without reflection, the optimal times are stable around the 600

μs to 700 μs. It means that the number of the Mu events is not sensitive to different $\vec{z}$ positions, wherever it is positioned at the middle of the target or the edge.

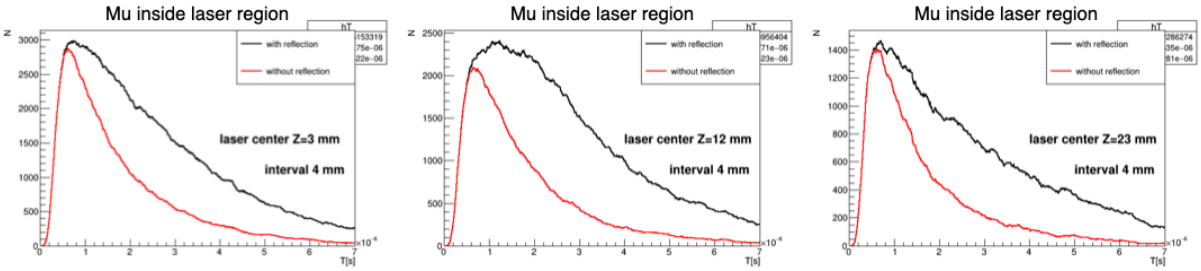

图 6.15 在不同的激光空间位置下，缪子素随时间变化的关系（上图分别为激光位于 Z=3，12 和 23 毫米处）。红色曲线是假设没有缪子素反射效应的模型，黑色曲线是假设存在反射模型的结果。在黑色曲线中，对应最大值的时间不同。

Figure 6.15 Mu emission as the results of the laser position scan. Red curves

With the reflection effect, the curve has a different performance. The optical time increases from the edge position to the center of the target, then drops back as the position goes to the other edge. The reflection effect of the Mu explains it: Mu events are expected to be reflected by the surface of the target. Therefore when the position is at the center, the region receives the contribution of the Mu events from both sides. In contrast, only the contribution from one side is possible at the edge.

This feature is expected to be directly measured in the validation experiment to confirm the reflection model.

6.4.2 Scan of the interval between targets

Another direction is to scan the interval between the two-piece. When the interval increases, the reflection effect is mitigated since the distance for Mu to travel is longer. Figure 6.17 shows the example of the interval scan on the Mu evolution with and without the reflection model. When the interval increases, the difference between the two curves is also reduced.

Such a feature is quantitatively exhibited in Figure 6.18, which shows the Mu yield result at different intervals while the position of the laser is fixed. The number of Mu shows again very stable without the reflection model while significantly changing with the reflection model. Such tendency could also be directly measured in the validation experiment.

Figure 6.19 shows the comparison of the Mu yield in the laser region under the condition

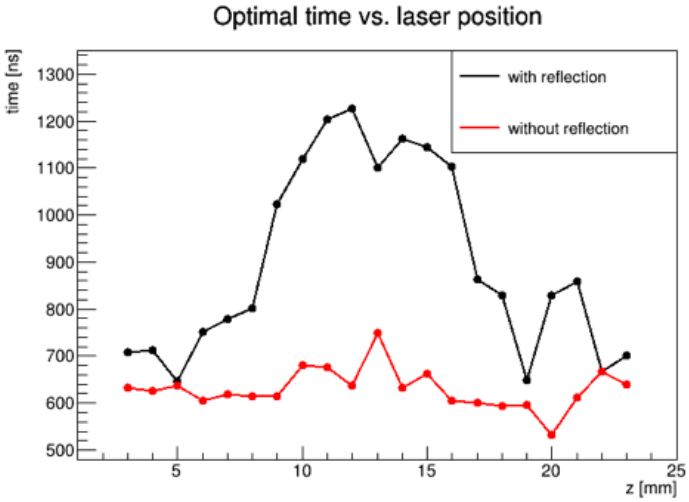

图 6.16　最佳的激光入射时间随着激光空间位置的变化关系。红色曲线是假设没有缪子素反射效应的模型，黑色曲线是假设存在反射模型的结果。通过此测量能很好区分是否存在真实反射过程。

Figure 6.16　The highest Mu emission as the function of the laser position scan

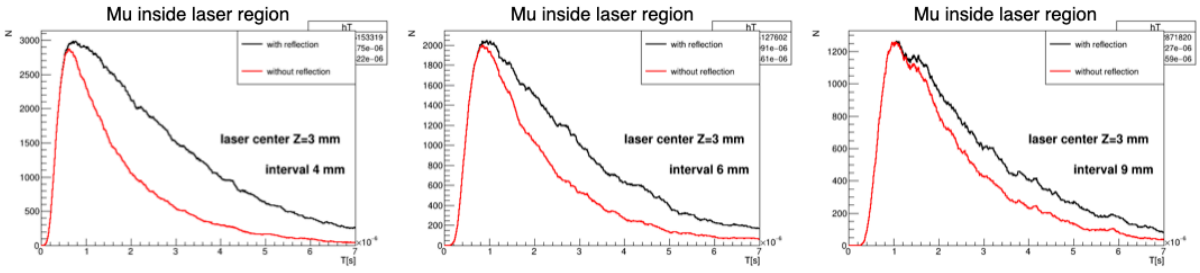

图 6.17　在不同的双层靶间距下，缪子素随时间变化的关系（上图的间距分别为 4，6 和 9 毫米处）。红色曲线是假设没有缪子素反射效应的模型，黑色曲线是假设存在反射模型的结果。如果取相同的激光照射时间，发现在黑色曲线中，对应最大值随着靶间距的加大而迅速下降。

Figure 6.17　The Mu emission results of the interval scan.

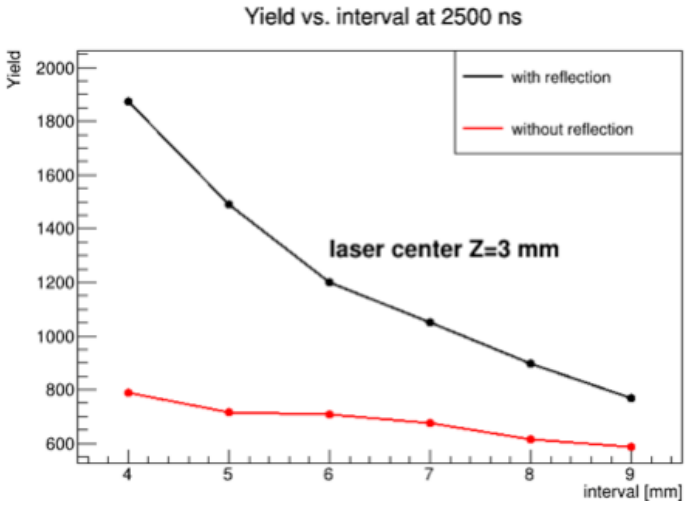

图 6.18 缪子素的电离数量随着靶间距的变化关系。红色曲线是假设没有缪子素反射效应的模型，黑色曲线是假设存在反射模型的结果。通过此测量能很好区分是否真实存在反射过程。激光入射时间均设置为 2500 纳秒。

Figure 6.18 The result of the interval scan. Laser were shot at 2500 ns at each case.

of the validation experiment. Compared with the single-layer design, the yield number of the Mu is estimated to be 1.6 times higher in the validation experiment, with only two layers.

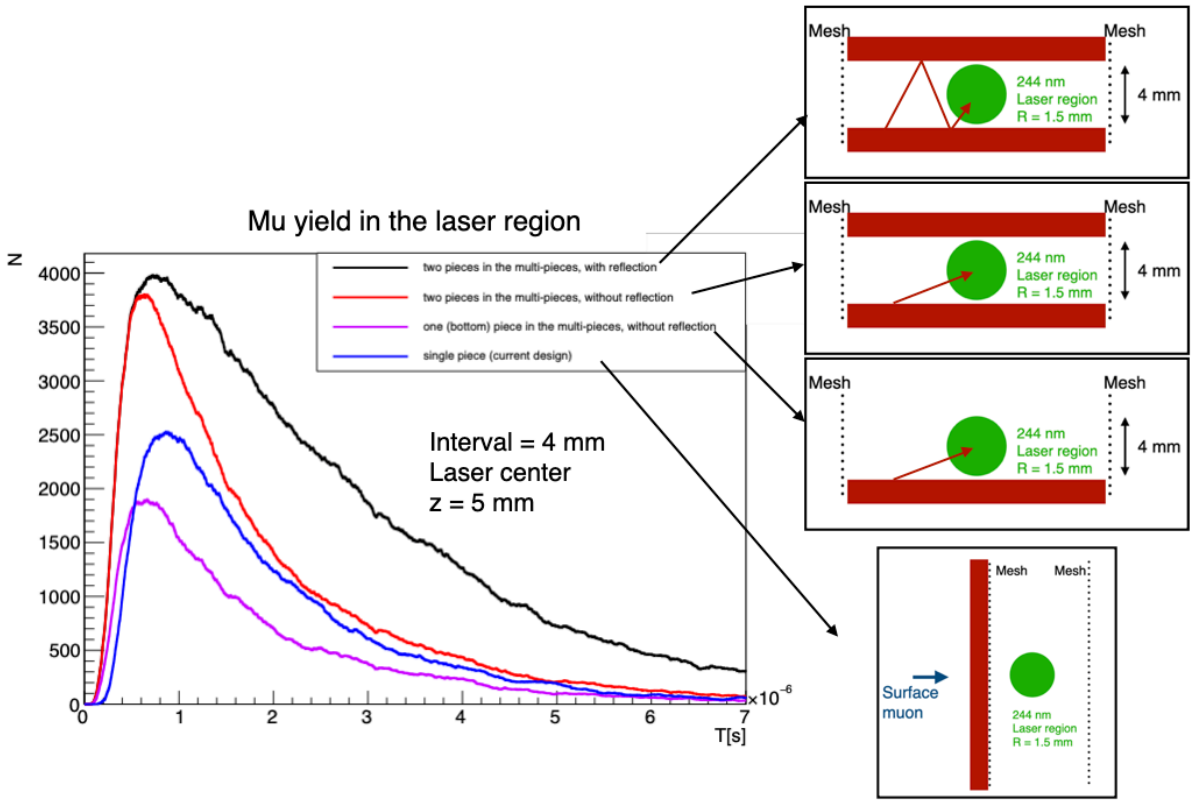

图 6.19　在多层靶的验证性实验设计中，缪子素电离数量在不同条件下的比较。即使只有双层靶的情况下，缪子素的数量比单层靶增加 1.6 倍左右。

Figure 6.19　Comparison of the Mu emission for validation experiment. The enhancement of the multi-layre is about 1.6 times higher than the single-layer even with only two layers.

7 Conclusion and Outlook

This thesis studied the development of a thermal muon source via Mu laser ionization for the proposed Muon $g-2$/EDM experiment at J-PARC.

The Mu ionization experiment was proposed and constructed to demonstrate laser ionization of Mu generated from silica aerogel. In addition, we proposed a novel design of a multi-layer aerogel target toward the high thermal muon intensity, exceeding the current statistical limit. All the works comprehensively studied the properties of thermal muon generation, including its generation efficiency and beam dynamics.

Section 7.1 presents the future perspectives on the thermal muon source developments, and Section 7.2 discusses the expected statistical limit for the upcoming J-PARC $g-2$/EDM experiment.

7.1 Future perspectives for thermal muon source development

In future developments, there are several directions toward the success of the thermal muon for the E34 experiment.

- **Continues studies on the Mu ionization experiment**. More data is expected in the upcoming phase of the Mu ionization experiment. A high-quality and higher energy laser beam is under preparation for checking the consistency of the muon rate with the simulation. In addition, the muon beam profile and its preliminary analysis were performed, but more data is necessary to complete the study of beam dynamics of the thermal muon. The determination of the thermal muon beam profile is critical for the next stage of the E34: the RFQ acceleration test.
- **Final technology choice on ionization laser system** is under investigation. The practical developments on the 122 nm laser and the 244 nm laser are ongoing. Their total available energy and the comparison of their performance should be tested based on the Mu ionization platform.
- **Spin manipulation of Mu at rest** is a straightforward application of muon or Mu spin precession in a transverse magnetic field. By collecting the decay positron from muon with both spin directions, detector acceptance and efficiency differences are canceled and systematic errors are removed. The magnetic field system on the laser ionization region manipulates spin and recovers the polarization loss in Mu formation.

In addtion, we investigate our method under the scope of muon cooling techniques. Now there are progress globally on the high-quality muon beam with high intensity and low emittance. At Paul Scherrer Institut (PSI), High-Intensity Muon Beam (HiMB) project[74] was proposed to increase the intensity of DC thermal muon beam to be the order of 10^{10} per second. muCool project[75] is ongoing to use the E-B field to reduce the phase space of the incident surface muon beam for better measurements of Mu.

Table 7.1 compares the generation of low-energy muon (LEM)[76] and Mu at PSI and J-PARC using the configuration of PSI Mu-MASS experiment[77] and E34 experiment, respectively. The statistics of Mu reach the same order for experiments at both facilities.

表 7.1　缪子素相关实验设施束流强度比较

Table 7.1　Comparison between J-PARC and PSI on muon beam and Mu intensity

Step	J-PARC (Mu ionization experiment)	PSI (with 15 keV LEM)	PSI (with future HiMB and muCool)
Surface muon intensity	3.6×10^6 Hz	4.2×10^8 Hz	$\sim 1\times10^{10}$ Hz
Mu yield efficiency	$\sim 10^{-3}$	$\sim 10^{-5}$	$\sim 2\times10^{-6}$ to $\sim 10^{-5}$
Mu yield intensity	$\sim 3\times10^3$ Hz	$\sim 2\times10^3$ Hz	$\sim 3\times10^4$ Hz

7.2 Statistical sensitivity for E34 experiment

Based on our results from the Mu ionization experiment, we discuss the expected statistical sensitivity for the upcoming Muon $g-2$/EDM experiment.

The precision of measurement with the extracted muon $g-2$ frequency $\sigma_{\omega_a}^{\rm exp}$ is inversely proportional to $\sqrt{N}A$[78]:

$$\frac{\sigma_{\omega_a}^{\rm exp}}{\omega_a} = \frac{\sqrt{2}}{\gamma\tau A\sqrt{N}}\frac{1}{\omega_a} \tag{7.1}$$

where N is the number of muons and the asymmetry A is proportional to the polarization.

We consider the fixed polarization of 0.5 in the E34 experiment and the upstream surface muon intensity of 3.2×10^8 Hz after H-line transport. The current result from the Mu ionization experiment estimates the Mu emission rate of 0.021, which is the combined result of the muon stopping (0.41), Mu formation (0.52), and the Mu vacuum yield (0.09). Given the high power laser ionization efficiency of 0.73 and other downstream efficiency estimations, the final muon intensity in the storage detector in the J-PARC Muon $g-2$/EDM experiment is estimated to

be 2×10^5 Hz. Such intensity satisfies the a_μ precision of 0.45 ppm in the first stage, similar to the BNL result or the FNAL Run-1 result, as illustrated in Figure 7.1. The realization of the novel multi-layer target design elevates the Mu intensity by a factor of 3 to 4, offering the opportunity for the experiment to reach the final goal of 0.1 ppm in a_μ.

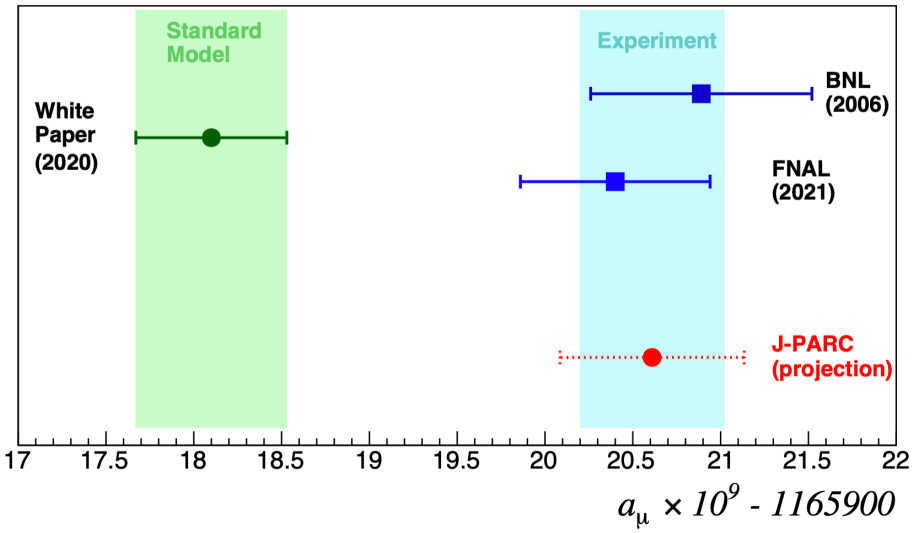

图 7.1 缪子反常磁矩 a_μ 测量总结。红色圆点及其统计误差代表 J-PARC 实验第一阶段的预期结果（以当前实验测量值为中心）。

Figure 7.1 The summary of current status of muon $g-2$ measurement. The red point is the expected result from Phase-1 of J-PARC experiment.

Bibliography

[1] PATRIGNANI C, et al. Review of Particle Physics[J]. Chin. Phys. C, 2016, 40(10): 100001. DOI: 10.1088/1674-1137/40/10/100001.

[2] JEGERLEHNER F, NYFFELER A. The Muon g-2[J]. Phys. Rept., 2009, 477: 1–110arXiv: 0902.3360 [hep-ph]. DOI: 10.1016/j.physrep.2009.04.003.

[3] PESKIN M E. An introduction to quantum field theory[M]. [S.l.]: CRC press, 2018.

[4] FARLEY F. The 47 years of muon g2[J]. Progress in Particle and Nuclear Physics, 2004, 52(1): 1–83 [2020–8–31]. DOI: 10.1016/j.ppnp.2003.09.004. ISSN: 01466410.

[5] SCHWINGER J S. On Quantum electrodynamics and the magnetic moment of the electron[J]. Phys. Rev., 1948, 73: 416–417. DOI: 10.1103/PhysRev.73.416.

[6] PARKER R H, YU C, ZHONG W, et al. Measurement of the fine-structure constant as a test of the Standard Model[J]. Science, 2018, 360: 191arXiv: 1812.04130 [physics.atom-ph]. DOI: 10.1126/science.aap7706.

[7] MOREL L, YAO Z, CLADÉ P, et al. Determination of the fine-structure constant with an accuracy of 81 parts per trillion[J]. Nature, 2020, 588(7836): 61–65. DOI: 10.1038/s41586-020-2964-7.

[8] HANNEKE D, FOGWELL S, GABRIELSE G. New Measurement of the Electron Magnetic Moment and the Fine Structure Constant[J]. Phys. Rev. Lett., 2008, 100: 120801arXiv: 0801.1134 [physics.atom-ph]. DOI: 10.1103/PhysRevLett.100.120801.

[9] MILLER J P, de RAFAEL E, ROBERTS B L. Muon (g-2): Experiment and theory[J]. Rept. Prog. Phys., 2007, 70: 795arXiv: hep-ph/0703049. DOI: 10.1088/0034-4885/70/5/R03.

[10] DAVIDSON S, NARDI E, NIR Y. Leptogenesis[J]. Phys. Rept., 2008, 466: 105–177arXiv: 0802.2962 [hep-ph]. DOI: 10.1016/j.physrep.2008.06.002.

[11] HEWETT J L, et al. Fundamental Physics at the Intensity Frontier[C]. [S.l.]: [s.n.], 2012arXiv: 1205.2671 [hep-ex]. DOI: 10.2172/1042577.

[12] KOBAYASHI M, MASKAWA T. CP Violation in the Renormalizable Theory of Weak Interaction[J]. Prog. Theor. Phys., 1973, 49: 652–657. DOI: 10.1143/PTP.49.652.

[13] POSPELOV M E, KHRIPLOVICH I B. Electric dipole moment of the W boson and the electron in the Kobayashi-Maskawa model[J]. Sov. J. Nucl. Phys., 1991, 53: 638–640.

[14] BOOTH M J. The Electric dipole moment of the W and electron in the Standard Model[J]. 1993arXiv: hep-ph/9301293.

[15] BENNETT G W, et al. An Improved Limit on the Muon Electric Dipole Moment[J]. Phys. Rev. D, 2009, 80: 052008arXiv: 0811.1207 [hep-ex]. DOI: 10.1103/PhysRevD.80.052008.

[16] AOYAMA T, ASMUSSEN N, BENAYOUN M, et al. The anomalous magnetic moment of the muon in the Standard Model[J]. Physics Reports, 2020 [2020–11–4]. DOI: 10.1016/j.physrep.2020.07.006. ISSN: 0370-1573.

[17] COLANGELO G, et al. Prospects for precise predictions of a_μ in the Standard Model[J]. 2022arXiv: 2203.15810 [hep-ph].

[18] BORSANYI S, et al. Leading hadronic contribution to the muon magnetic moment from lattice QCD[J]. Nature, 2021, 593(7857): 51–55arXiv: 2002.12347 [hep-lat]. DOI: 10.1038/s41586-021-03418-1.

[19] CZARNECKI A, MARCIANO W J. The Muon anomalous magnetic moment: A Harbinger for 'new physics'[J]. Phys. Rev. D, 2001, 64: 013014arXiv: hep-ph/0102122. DOI: 10.1103/PhysRevD.64.013014.

[20] ATHRON P, BALÁZS C, JACOB D, et al. Simple BSM explanations of a_μ in light of the FNAL muon $g-2$ measurement[J]. PoS, 2022, EPS-HEP2021: 695arXiv: 2110.07156 [hep-ph]. DOI: 10.22323/1.398.0695.

[21] ENDO M, HAMAGUCHI K, IWAMOTO S, et al. Probing minimal SUSY scenarios in the light of muon $g-2$ and dark matter[J]. JHEP, 2017, 06: 031arXiv: 1704.05287 [hep-ph]. DOI: 10.1007/JHEP06(2017)031.

[22] BUEN-ABAD M A, FAN J, REECE M, et al. Challenges for an axion explanation of the muon $g-2$ measurement[J]. JHEP, 2021, 09: 101arXiv: 2104.03267 [hep-ph]. DOI: 10.1007/JHEP09(2021)101.

[23] KRNJAIC G, MARQUES-TAVARES G, REDIGOLO D, et al. Probing Muonphilic Force Carriers and Dark Matter at Kaon Factories[J]. Phys. Rev. Lett., 2020, 124(4): 041802arXiv: 1902.07715 [hep-ph]. DOI: 10.1103/PhysRevLett.124.041802.

[24] BAILEY J, BARTL W, von BOCHMANN G, et al. Precise Measurement of the Anomalous Magnetic Moment of the Muon[J]. Nuovo Cim. A, 1972, 9: 369–432. DOI: 10.1007/BF02785248.

[25] Muon, Collaboration, BENNETT G W. Final Report of the Muon E821 Anomalous Magnetic Moment Measurement at BNL[J]. Physical Review D, 2006, 73(7): 072003arXiv: hep-ex/0602035 [2020–8–31]. DOI: 10.1103/PhysRevD.73.072003. ISSN: 1550-7998, 1550-2368.

[26] GRANGE J, et al. Muon (g-2) Technical Design Report[J]. 2015arXiv: 1501.06858 [physics.ins-det].

[27] Jackson, J.D. Classical Electrodynamics[M]. 3rd Edition. [S.l.]: New York :Wiley, 1999 [2021–11–16].

[28] BAYES R, et al. Experimental Constraints on Left-Right Symmetric Models from Muon Decay[J]. Phys. Rev. Lett., 2011, 106: 041804. DOI: 10.1103/PhysRevLett.106.041804.

[29] KHAW K S. Towards next generation fundamental precision measurements with muons[D]. ETH Zurich, 2015.

[30] Muon g2 Collaboration, ABI B, ALBAHRI T, et al. Measurement of the Positive Muon Anomalous Magnetic Moment to 0.46 ppm[J]. Physical Review Letters, 2021, 126(14): 141801 [2021–11–16]. DOI: 10.1103/PhysRevLett.126.141801.

[31] ABE M, BAE S, BEER G, et al. A new approach for measuring the muon anomalous magnetic moment and electric dipole moment[J]. Progress of Theoretical and Experimental Physics, 2019, 2019(5): 053C02 [2020–11–10]. DOI: 10.1093/ptep/ptz030. ISSN: 2050-3911.

[32] KAWAMURA N. Current Status of Muon Science Facility[J]. JPS Conf. Proc., 2021, 33: 011052. DOI: 10.7566/JPSCP.33.011052.

[33] BERKO S, MILLS A, CRANE W, et al. Positron Studies of Solids, Surfaces, and Atoms: A Symposium to Celebrate Stephan Berko's 60th Birthday, Brandeis University, December 12, 1984[M]. [S.l.]: World Scientific, 1986. ISBN: 9789971978440.

[34] HUGHES V W, MCCOLM D W, ZIOCK K, et al. Muonium. I. Muonium Formation and Larmor Precession[J]. Phys. Rev. A, 3 1970, 1: 595–617.

[35] HUGHES V W, MCCOLM D W, ZIOCK K, et al. Formation of Muonium and Observation of its Larmor Precession[J]. Phys. Rev. Lett., 1960, 5: 63–65. DOI: 10.1103/PhysRevLett.5.63.

[36] JUNGMANN K P. Muonium-physics of a most fundamental atom[J]. Nucl. Phys. B Proc. Suppl., 2006, 155: 355–357. DOI: 10.1016/j.nuclphysbps.2006.02.100.

[37] NAGAMINE K, MIYAKE Y, SHIMOMURA K, et al. Ultraslow Positive-Muon Generation by Laser Ionization of Thermal Muonium from Hot Tungsten at Primary Proton Beam[J]. Phys. Rev. Lett., 24 1995, 74: 4811–4814.

[38] BAKULE P, MATSUDA Y, MIYAKE Y, et al. Pulsed source of ultra low energy positive muons for near-surface μSR studies[J]. Nuclear Instruments and Methods in Physics Research Section B: Beam Interactions with Materials and Atoms, 2008, 266(2): 335–346. ISSN: 0168-583X.

[39] PROKSCHA T, MORENZONI E, DEITERS K, et al. The new μE4 beam at PSI: A hybrid-type large acceptance channel for the generation of a high intensity surface-muon beam[J]. Nuclear Instruments and Methods in Physics Research Section A: Accelerators, Spectrometers, Detectors and Associated Equipment, 2008, 595(2): 317–331. ISSN: 0168-9002.

[40] BELOSEVIC I, et al. MuCool: A next step towards efficient muon beam compression[J]. Eur. Phys. J. C, 2019, 79(5): 430.

[41] BAKULE P, BEER G A, CONTRERAS D, et al. Measurement of muonium emission from silica aerogel[J]. Progress of Theoretical and Experimental Physics, 2013, 2013(10): 103C01–103C01 [2020–8–31]. DOI: 10.1093/ptep/ptt080. ISSN: 2050-3911.

[42] BEER G A, FUJIWARA Y, HIROTA S, et al. Enhancement of muonium emission rate from silica aerogel with a laser-ablated surface[J]. Progress of Theoretical and Experimental Physics, 2014, 2014(9). ISSN: 2050-3911.

[43] BEARE J, BEER G, BREWER J H, et al. Study of muonium emission from laser-ablated silica aerogel[J]. Progress of Theoretical and Experimental Physics, 2020, 2020(12). ISSN: 2050-3911.

[44] MILLS A P, IMAZATO J, SAITOH S, et al. Generation of Thermal Muonium in Vacuum[J]. Phys. Rev. Lett., 14 1986, 56: 1463–1466.

[45] BEER G A, MARSHALL G M, MASON G R, et al. Emission of Muonium into Vacuum from a Silica-Powder Layer[J]. Phys. Rev. Lett., 6 1986, 57: 671–674.

[46] KHAW K S, ANTOGNINI A, PROKSCHA T, et al. Spatial confinement of muonium atoms[J]. Phys. Rev. A, 2016, 94(2): 022716.

[47] CHU S, MILLS A P, YODH A G, et al. Laser Excitation of the Muonium 1 S 2 S Transition[J]. Physical Review Letters, 1988, 60(2): 101–104 [2020–8–31]. DOI: 10.1103/PhysRevLett.60.101. ISSN: 0031-9007.

[48] SAITO N, YU O, MIYAZAKI K, et al. High-efficiency generation of pulsed Lyman- radiation by resonant laser wave mixing in low pressure Kr-Ar mixture[J]. Optics Express, 2016, 24(7): 7566.

[49] ZHANG C, HARA H, HIRAKI T, et al. Simulation Study of Laser Ionization of Muonium by 1S-2S Excitation for the Muon g ? 2/EDM Experiment at J-PARC[G]// Proceedings of the 3rd J-PARC Symposium (J-PARC2019). Vol. 33. 0 vols. JPS Conference Proceedings 33. [S.l.]: Journal of the Physical Society of Japan, 2021. [2021–3–26]. DOI: 10.7566/JPSCP.33.011125.

[50] STRASSER P, et al. Status of the New Surface Muon Beamline at J-PARC MUSE[J]. JPS Conf. Proc., 2018, 21: 011061. DOI: 10.7566/JPSCP.21.011061.

[51] MEYER V, BAGAYEV S N, BAIRD P E G, et al. Measurement of the 1 s 2 s Energy Interval in Muonium[J]. Physical Review Letters, 2000, 84(6): 1136–1139 [2020–8–31]. DOI: 10.1103/PhysRevLett.84.1136. ISSN: 0031-9007, 1079-7114.

[52] KITAMURA R, BAE S, CHOI S, et al. Development of negative muonium ion source for muon acceleration[J]. Physical Review Accelerators and Beams, 2021, 24(3): 033403 [2021–4–6]. DOI: 10.1103/PhysRevAccelBeams.24.033403.

[53] OTANI M, KAWAMURA N, MIBE T, et al. Simulation of Surface Muon Beamline, UltraSlow Muon Production and Extraction for the J-PARC g-2/EDM Experiment[J]. Journal of Physics: Conference Series, 2018, 1067: 052018 [2020–8–31]. DOI: 10.1088/1742-6596/1067/5/052018. ISSN: 1742-6588, 1742-6596.

[54] KITAMURA R. Demonstration of the muon acceleration with Radio-Frequency Quadrupole linac[D]. University of Tokyo, 2018.

[55] DALESIO L R, KOZUBAL A, KRAIMER M. EPICS architecture[R]. Los Alamos National Lab., NM (United States), 1991.

[56] NAKAZAWA Y, BAE S, CHOI H, et al. Beam commissioning of muon beamline using negative hydrogen ions generated by ultraviolet light[J]. Nuclear Instruments and Methods in Physics Research Section A: Accelerators, Spectrometers, Detectors and Associated Equipment, 2019, 937: 164–167 [2020–9–25]. DOI: 10.1016/j.nima.2019.05.043. ISSN: 0168-9002.

[57] ROBERTS T. G4beamline Users Guide[J]. 201.

[58] AGOSTINELLI S, et al. GEANT4–a simulation toolkit[J]. Nucl. Instrum. Meth. A, 2003, 506: 250–303. DOI: 10.1016/S0168-9002(03)01368-8.

[59] MCQUARRIE D A, SIMON J D. Physical chemistry: a molecular approach[M]. Vol. 1. [S.l.]: University science books Sausalito, CA, 1997.

[60] CHANDRASEKHAR S. Stochastic Problems in Physics and Astronomy[J]. Rev. Mod. Phys., 1 1943, 15: 1–89.

[61] HAAS M, JENTSCHURA U D, KEITEL C H, et al. Two-photon excitation dynamics in bound two-body Coulomb systems including ac Stark shift and ionization[J]. Phys. Rev. A, 5 2006, 73: 052501.

[62] SEDLÁK K, SHIROKA T, SALMAN Z. Manual of musrSim[J]. Lmu.Web.Psi.Ch, 2016: 1–26.

[63] SYSTEMES D. Opera Electromagnetic and Electromechanical Simulation, https://operafea.com[EB/OL]. https://operafea.com.

[64] CORPORATION M. MISUMI Frame[EB/OL]. https://jp.misumi-ec.com/special/alumiframe/frames/pr/.

[65] CORPORATION Y E. F3YC16 relay module[EB/OL]. https://www.yokogawa.co.jp/solutions/products-platforms/control-system/programmable-logic-controller/plc-io/plc-output/.

[66] CORPORATION Y E. WideField3[EB/OL]. https://www.yokogawa.co.jp/solutions/products-platforms/control-system/programmable-logic-controller/plc-software/plc-programming-tool/.

[67] SINCLAIR J. EDM: Extensible Display Manager for EPICS. 2003.

[68] KASEMIR K, et al. Control system studio applications[C]// Proc. 11th Int. Conf. on Accelerator and Large Experimental Physics Control Systems (ICALEPCS' 07). [S.l.]: [s.n.], 2007: 692–694.

[69] SATAKE I, SATOH M, SUWADA T, et al. Improvement of Temperature and Humidity Measurement System for KEK Injector Linac[C]// Proceedings of ICALEPCS. [S.l.]: [s.n.], 2017: 1323–1326.

[70] https://caen.it/products/v1720/.

[71] INC. A. Ortec579[EB/OL]. https://www.ortec-online.com/products/electronics/amplifiers/579.

[72] SIKORA J P, CARLSON B T, DUGGINS D O, et al. Electron Cloud Density Measurements in Accelerator Beam-pipe Using Resonant Microwave Excitation[J]. Nucl. Instrum. Meth. A, 2014, 754: 28–35arXiv: 1311.5633 [physics.acc-ph]. DOI: 10.1016/j.nima.2014.03.063.

[73] ACKERHALT J R, SHORE B W. Rate equations versus Bloch equations in multiphoton ionization[J]. Phys. Rev. A, 1 1977, 16: 277–282.

[74] AIBA M, et al. Science Case for the new High-Intensity Muon Beams HIMB at PSI[J]. 2021arXiv: 2111.05788 [hep-ex].

[75] ANTOGNINI A, TAQQU D. MuCool: muon cooling for high-brightness μ^+ beams[J]. SciPost Phys. Proc., 2021, 5: 030. DOI: 10.21468/SciPostPhysProc.5.030.

[76] KHAW K S, ANTOGNINI A, CRIVELLI P, et al. Geant4 simulation of the PSI LEM beam line: energy loss and muonium formation in thin foils and the impact of unmoderated muons on the μSR spectrometer[J]. JINST, 2015, 10(10): P10025arXiv: 1506.01779 [physics.ins-det]. DOI: 10.1088/1748-0221/10/10/P10025.

[77] CRIVELLI P. The Mu-MASS (MuoniuM lAser SpectroScopy) experiment[J]. Hyperfine Interact., 2018, 239(1): 49arXiv: 1811.00310 [physics.atom-ph]. DOI: 10.1007/s10751-018-1525-z.

[78] BENNETT G W, et al. Statistical equations and methods applied to the precision muon (g-2) experiment at BNL[J]. Nucl. Instrum. Meth. A, 2007, 579: 1096–1116. DOI: 10.1016/j.nima.2007.06.023.

Publications

[1] C. Zhang, H. Hara, T. Hiraki, Y. Ikedo, Y. Imai, K. Ishida, S. Kamal, N. Kawamura, A. Koda and Y. Mao, *et al.* "Simulation Study of Laser Ionization of Muonium by 1S-2S Excitation for the Muon $g-2$/EDM Experiment at J-PARC," JPS Conf. Proc. **33** (2021), 011125 doi:10.7566/JPSCP.33.011125

Acknowledgement

I would like to thank my supervisors, **Prof. Yajun Mao** who encouraged me to join this exciting experiment, and **Prof. Naohito Saito** who took care of me from research to daily life during my more than three years stay in Japan.

I am extremely grateful to another mentor in Japan, **Prof. Tsutomu Mibe**. I have learned a lot in the weekly discussions, where those enlightening moments were impressive.

I had a great time working with **Kazuhito Suzuki** on the muon beam-line. Hiking with him was also of great pleasure. I enjoyed a lot collaborating with **Shusei Kamioka** on laser simulation and the discussions with **Katsuhiko Ishida**, who can always understand my points quickly and make excellent suggestions.

Takahiro Hiraki from the Okayama group helped me with my limited knowledge of laser development. **Taihei Adachi** and **Masashi Otani** are friendly experts to whom I can ask questions on muon beam-line without hesitation.

Many thanks to **Glen Marshall**, from whom I have received more valuable advice than I expected. My special thanks go to **Arthur Olin, Yannis Semertzidis** and **Kim Siang Khaw** for their kindness and critical encouragement.

COVID-19 changed everything. I would like to thank all the friends I met at Tsukuba and Tokai for their physical and mental support in this foreign land. Students at Saito-Mibe-lab were also very collaborative towards a good lab environment. I am grateful to **Abdul Rehman** for supporting me in my darkest time. My special gratitude goes to **Bruce** and **Jing Wang**, who made me feel at home.

This study was supported by China Scholarship Council (CSC).